



**HAL**  
open science

# Magnetic structures of Mn-rich and of Fe-rich $\text{TmMn } 6 - x \text{ Fe } x \text{ Sn } 6$ stannides with (Mn, Fe) kagome networks and related $^{119}\text{Sn}$ hyperfine magnetic fields

G. Venturini, B. Malaman, Gérard Le Caër, T. Mazet

► **To cite this version:**

G. Venturini, B. Malaman, Gérard Le Caër, T. Mazet. Magnetic structures of Mn-rich and of Fe-rich  $\text{TmMn } 6 - x \text{ Fe } x \text{ Sn } 6$  stannides with (Mn, Fe) kagome networks and related  $^{119}\text{Sn}$  hyperfine magnetic fields. *Physical Review B*, 2021, 104 (18), pp.184433. 10.1103/PhysRevB.104.184433 . hal-03464435

**HAL Id: hal-03464435**

**<https://hal.science/hal-03464435>**

Submitted on 3 Dec 2021

**HAL** is a multi-disciplinary open access archive for the deposit and dissemination of scientific research documents, whether they are published or not. The documents may come from teaching and research institutions in France or abroad, or from public or private research centers.

L'archive ouverte pluridisciplinaire **HAL**, est destinée au dépôt et à la diffusion de documents scientifiques de niveau recherche, publiés ou non, émanant des établissements d'enseignement et de recherche français ou étrangers, des laboratoires publics ou privés.

**Magnetic structures of Mn-rich and of Fe-rich  $\text{TmMn}_{6-x}\text{Fe}_x\text{Sn}_6$  stannides with (Mn, Fe) kagome networks and related  $^{119}\text{Sn}$  hyperfine magnetic fields**

G. Venturini<sup>1†</sup>, B. Malaman<sup>1\*</sup>, G. Le Caër<sup>2</sup>, T. Mazet<sup>1</sup>

<sup>1</sup> Université de Lorraine, CNRS, IJL, F-54000 Nancy, France

<sup>2</sup> Université de Rennes I, CNRS, IPR (Institut de Physique de Rennes) - UMR 6251, F-35000 Rennes, France

**Abstract**

Stannides  $\text{TmMn}_{6-x}\text{Fe}_x\text{Sn}_6$ , with hexagonal  $\text{HfFe}_6\text{Ge}_6$ -type structures, were studied by X-ray and neutron diffraction, magnetic measurements and by  $^{119}\text{Sn}$  Mössbauer spectroscopy. Transition metal atoms form kagome networks in (001) planes with an intraplanar ferromagnetic coupling of their moments. At temperatures higher than  $\sim 20$  to  $50$  K, Mn-rich stannides, ( $x = 0.4, 0.6, 1.2$ ), have an AFII easy-plane antiferromagnetic structure, with interplanar couplings  $++-$  along the  $c$ -axis. The thulium sublattice orders magnetically at low temperature. The complexity of the resultant neutron diffraction patterns arises from a mixture of several magnetic phases, some being incommensurate. The Tm sublattice does not order above  $1.6$  K in Fe-rich stannides ( $x = 4.25, 4.5, 5.0$ ). Fe-rich stannides have an AFI antiferromagnetic structure, this time with interplanar couplings  $+--$ . The  $M = \text{Mn/Fe}$  magnetic moments are directed along the  $c$ -axis for  $x=5$  at any temperature. Further, neutron diffraction shows that moments rotate from the  $c$ -axis towards the basal plane above  $4.2$  K with maximum rotation angles of  $\sim 70^\circ$  and of  $\sim 55^\circ$  reached at  $\sim 50$  K and  $\sim 80$  K for  $x = 4.25$  and  $4.50$  respectively. Transferred hyperfine fields at tin sites of  $\text{TmMn}_{6-x}\text{Fe}_x\text{Sn}_6$  stannides are the moduli of  $^{119}\text{Sn}$  vectorial hyperfine magnetic fields that are modelled for the AFI and AFII magnetic structures assuming a random substitution of Mn with Fe. Models involve sums of dipolar-type and of isotropic vector components, with simple assumptions about the model parameters. The transferred hyperfine magnetic fields at  $^{119}\text{Sn}$  nuclei are measured by Mössbauer spectroscopy. The hyperfine magnetic fields of Sn atoms, whose six transition-metal nearest neighbors are ferromagnetically coupled, are predicted and observed to vary linearly with their number of Fe first nearest neighbors. The hyperfine magnetic fields on Sn atoms sandwiched between two antiferromagnetically-coupled kagome planes are expected proportional to  $|p_2 - p_1|$ , where one of the two kagome planes contains  $p_1$  Fe first nearest

neighbor and the other  $p_2$ . Tin atoms, with a ferromagnetic first nearest neighbor shell, experience negative hyperfine fields in Mn-rich stannides whereas they experience positive hyperfine fields in the Fe-rich stannides. This change is explained by a change of sign of the isotropic hyperfine magnetic fields which occurs when going from Mn-rich to Fe-rich stannides.

PACS numbers: 33.45+x, 71.20.Lp, 75.25.+z, 76.80.+y

† deceased

\* [bernard.malaman@univ-lorraine.fr](mailto:bernard.malaman@univ-lorraine.fr)

[gerard.le-caer@univ-rennes1.fr](mailto:gerard.le-caer@univ-rennes1.fr)

[thomas.mazet@univ-lorraine.fr](mailto:thomas.mazet@univ-lorraine.fr)

## I. INTRODUCTION

The hexagonal  $\text{HfFe}_6\text{Ge}_6$ -type structure of  $\text{RM}_6\text{Sn}_6$  stannides, space group  $P6/mmm$ , (Fig. 1) is first characterized by three crystallographic sites, namely 2c, 2d and 2e, which are equally occupied by Sn atoms. Second, the crystallographic site 6i is occupied by M transition metal atoms, where M is Mn or Fe herein. Finally, the crystallographic site 1a is occupied by rare-earth atoms R (Fig. 1, Table S1 of [1]). Manganese atoms form kagome networks (Fig. S1 of [1]) in (001) planes (ab planes) also called kagome planes from now on.

Some recent studies ([2-12] and Sec. I of [1]), deal with transition-metal-based kagome magnets, a class of materials which are of fundamental importance. They include, among others,  $\text{RM}_6\text{Sn}_6$  stannides. These studies focus on the physical consequences of the interplay between lattice geometry and electron correlation.

Most previous studies of  $\text{RM}_6\text{Sn}_6$  stannides focused on crystallographic characteristics (Fig. 1) and on magnetic properties and structures. In addition,  $^{119}\text{Sn}$  Mössbauer spectroscopy yielded detailed information on hyperfine magnetic fields in stannides, notably in  $\text{RMn}_6\text{Sn}_6$  and  $\text{RFe}_6\text{Sn}_6$  (R = Li, Mg, Sc, Pr-Sm, Gd-Lu, U) [13-26].  $^{119}\text{Sn}$  hyperfine magnetic fields provide invaluable information on the local evolution of magnetic structure.

The present work is devoted to  $\text{TmMn}_{6-x}\text{Fe}_x\text{Sn}_6$  stannides, either Mn-rich ( $x = 0.4, 0.6, 1.2$ ) or Fe-rich ( $x = 4.25, 4.5, 5.0$ ). A  $\text{TmMn}_{6-x}\text{Fe}_x\text{Sn}_6$  stannide might form for any  $x$  as  $\text{TmMn}_6\text{Sn}_6$  and  $\text{TmFe}_6\text{Sn}_6$  both crystallize with the  $\text{HfFe}_6\text{Ge}_6$ -type structure. Our aim was first to follow the effect of the substitution of Mn with Fe on magnetic structures, as studied by magnetic measurements and neutron diffraction, and second its effect on transferred hyperfine magnetic fields at  $^{119}\text{Sn}$  nuclei. Complex magnetic structures are observed at low temperatures in Mn-rich stannides because of the ordering of the Tm magnetic moments. By contrast, magnetic structures are simpler in Fe-rich stannides because the Tm magnetic moments do not order above 1.6 K. Two simple “high-temperature” antiferromagnetic (AF) structures, named AFII and AFI are observed from neutron diffraction patterns. They are characterized by an ordering of the transition metal moments which are ferromagnetically coupled in their (0 0 1) kagome planes [24]. These moments lie in the kagome planes in the Mn-rich stannides and are perpendicular to them, at least at 4.2 K, in the Fe-rich stannides (Fig. 2). Successive ferromagnetic (0 0 1) kagome planes are coupled along [0 0 1] according to sequences, ++ -- and +-+- for AFII and AFI respectively [20, 25] (Fig. 2).

Above 324 K,  $\text{TmMn}_6\text{Sn}_6$  exhibits an easy-plane AFII antiferromagnetic structure [25]. An easy-axis AFI-type structure is observed instead in  $\text{TmFe}_6\text{Sn}_6$ , at  $T > \sim 1.6$  K, as in

most  $\text{HfFe}_6\text{Ge}_6$ -type  $\text{RFe}_6\text{Sn}_6$  stannides [25]. The Fe moments,  $\mu_{\text{Fe}}=2.40(4) \mu_{\text{B}}$  at 2 K, are directed along the c-axis.

In practice,  $\text{TmFe}_6\text{Sn}_6$  is slightly under-stoichiometric in Tm, with a composition  $\text{Tm}_{1-\delta}\text{Fe}_6\text{Sn}_6$  ( $\delta \approx 0.1$ ) [25]. X-Ray diffraction patterns at room temperature (RT, nominally 295 K) indicate that Mn-rich  $\text{TmMn}_{6-x}\text{Fe}_x\text{Sn}_6$  stannides are essentially stoichiometric in Tm while the Fe-rich ones,  $\text{Tm}_{1-\delta}\text{Mn}_{6-x}\text{Fe}_x\text{Sn}_6$ , are slightly under-stoichiometric in Tm with  $\delta \approx 0.05$  (Table S2 of [1]). The nominal composition  $\text{TmMn}_{6-x}\text{Fe}_x\text{Sn}_6$  will still be used hereafter.

The transferred magnetic hyperfine fields at  $^{119}\text{Sn}$  nuclei are interpreted with a model whose physical basis finds a justification in first-principles electronic structure calculations [13, 17]. It combines both dipolar and isotropic magnetic field components with the additional assumption of a random distribution of Mn and Fe on the sites 6i. The predicted hyperfine magnetic fields are then compared with hyperfine magnetic fields obtained from  $^{119}\text{Sn}$  Mössbauer spectra. However, it is very difficult to confidently differentiate the effects of complex low-temperature magnetic structures on the  $^{119}\text{Sn}$  Mössbauer spectra from those of the disordered substitution of Mn with Fe (Fig. 2 and Fig. S7 of [1]). To circumvent these difficulties, the magnetic structures AFI and AFII were given a major role to compare experimental and predicted hyperfine magnetic fields.

## II. EXPERIMENTAL METHODS

### A. Materials

The samples were prepared in an induction furnace starting from stoichiometric mixtures of elements: Tm from Alphaceasar, 99.9%; Fe from Cerac, 99.95%; Mn from Chempur, 99.99%; Sn from Chempur, 99.99%. As-cast ingots were annealed at 1123 K for one week and quenched in water. Phases were identified by X-ray powder analysis (Xpert Pro diffractometer  $\text{CuK}\alpha$ ). Low-intensity peaks due to “impurities” were attributed respectively to elemental tin,  $\text{Mn}_{1-x}\text{Fe}_x\text{Sn}_2$  ( $\text{CuAl}_2$ -type),  $(\text{Mn,Fe})_{2-x}\text{Sn}$  ( $\text{Ni}_2\text{In}$ -type) and, in Fe-rich stannides, to  $\text{CeNiSi}_2$ -type  $\text{Tm}(\text{Mn,Fe})_x\text{Sn}_2$ . All impurities represent about 5 wt%.

### B. Magnetization measurements and neutron diffraction

The thermal variation of the magnetisation was measured with a MANICS magneto-susceptometer at a temperature increasing from 300 K to 700 K in an applied field of 0.05 T.

The low temperature (5-350 K) magnetization measurements were performed upon FC with a Physical Property Measurement System (PPMS) from Quantum Design in DC field up to 9 T. Neutron diffraction patterns were obtained with the D1B diffractometer at the Institut Laue Langevin (Grenoble) at a wavelength  $\lambda = 2.520\text{\AA}$ . Structural and magnetic parameters were refined using the Fullprof software [27]. They are detailed in [1].

### C. $^{119}\text{Sn}$ Mössbauer spectroscopy

$^{119}\text{Sn}$  Mössbauer spectra were measured in transmission geometry with a spectrometer operating in the conventional constant-acceleration mode. Spectra were recorded at various temperatures from 4.2 to 300 K in a JANIS (Research Company Inc.) liquid helium cryostat. Polycrystalline absorbers, with natural abundance of  $^{119}\text{Sn}$  isotope and area density of  $\sim 10\text{ mg}\cdot\text{cm}^{-2}$ , were used. The source, kept at room temperature, was  $\text{Ba}^{119\text{m}}\text{SnO}_3$  with a nominal activity of 10 mCi. A palladium foil of 0.05 mm thickness was used as a critical absorber for tin X-rays. Velocity calibration was performed against a 12  $\mu\text{m}$ -thick  $\alpha\text{-Fe}$  foil at RT using a source of  $^{57}\text{Co}$  in Rh.  $^{119}\text{Sn}$  isomer shifts (IS or  $\delta$ ) are referred to  $\text{BaSnO}_3$  at RT.

$^{119}\text{Sn}$  Mössbauer spectra of  $\text{TmMn}_{6-x}\text{Fe}_x\text{Sn}_6$  were fitted with a standard least-squares method making assumptions which are briefly described in Sec. IVA of [1]. A hyperfine magnetic field distribution was calculated for  $\text{TmMSn}_6$  at 4.2 K (Sec. XB of [1]) with a constrained Hesse-Rübartsch method [28]. In  $\text{TmMSn}_6$  (M=Mn or Fe), point symmetries at sites 2c, 2d and 2e, are respectively  $\bar{6}m2$ ,  $\bar{6}m2$  and  $6mm$ . They imply that the Z principal axes of the electric field gradient tensors (h=c, d, e) are parallel to the c-axis and that the associated asymmetry parameters are all equal to zero (Sec. IVB of [1]). The effects of electric field gradients on the fitted hyperfine magnetic fields are further discussed in Sec. IVB of [1].

Only absolute values of  $^{119}\text{Sn}$  hyperfine magnetic fields are measured in our experimental conditions. These measured fields are the only hyperfine parameters we discuss in the present work. Theoretical results are available for hyperfine magnetic fields transferred at Sn sites in  $\text{RMn}_6\text{Sn}_6$  with R=Mg, Zr, Hf [17] and for  $\text{LiMn}_6\text{Sn}_6$  [13]. We infer from this information the signs of the measured hyperfine magnetic fields.

### III. CRYSTALLOGRAPHIC FEATURES OF $\text{TmMn}_{6-x}\text{Fe}_x\text{Sn}_6$

The hexagonal  $\text{HfFe}_6\text{Ge}_6$ -type structure (space group no 191:  $P6/mmm$ ) depicted in Fig.1 may be described as being made from two distinct slabs. The latter are characterized by

rather different magnetic interactions in ternary  $\text{RMn}_6\text{Sn}_6$  stannides [20]: a Mn-(R-Sn(2c))-Mn slab and a Mn-Sn(2e)-Sn(2d)-Sn(2e)-Mn one (Fig. 1a). The Sn(2d) and Sn(2c) sites are in mirror planes perpendicular to the  $c$  axis. Hereafter, tin atoms will be denominated indifferently as Sn(2h) “atoms” or “sites” where  $h=c, d, e$  refers to the sites they occupy (2c, 2d, 2e) (Fig. 1).

Tin atoms at (2c) and (2d) sites in  $\text{RMn}_6\text{Sn}_6$  are at the centers of trigonal prisms of Mn atoms (Fig. 1b). Their first Mn neighbors form equilateral triangles in two parallel kagome planes. By contrast, the neighbors of Sn(2e) atoms are located at the vertices of regular hexagons of a single kagome plane, as sketched in Fig. 1b. In  $\text{RMn}_{6-x}\text{Fe}_x\text{Sn}_6$ , all three tin sites have six M transition metal atoms as first nearest neighbors and the 2c, 2d, and 2e Sn sites have three, zero, and one R neighbors, respectively. These structural features have, among others, the following two consequences:

*a)* only Sn(2e) and Tm atoms contribute significantly to the structure factors of  $(h\ k\ 2\ell+1)$  lines. They are for instance proportional to  $(f_{\text{Sn}}-f_{\text{Tm}})$  for  $\ell = 0$  for any  $x$ . Because the coherent scattering lengths  $b_{\text{Sn}}$  and  $b_{\text{Tm}}$  have similar values, 6.225 fm and 7.07 fm respectively, substantial intensities of the  $(h\ k\ 1)$  neutron diffraction lines are essentially due to magnetic contributions.

*b)* The  $^{119}\text{Sn}$  hyperfine magnetic fields at the three tin sites depend on the local configurations of the magnetic moments of their first M nearest neighbors, located in two kagome planes for Sn(2d) and Sn(2c) sites and in a single kagome plane for Sn(2e) sites (Fig. 1). Although the two former planes are undistinguishable, we choose, for convenience, to denote as  $\text{K}^+$  the kagome plane first met when going from a given Sn(2h) atom ( $h=c, d$ ) in the [001] direction and as  $\text{K}^-$  the one first met in the opposite direction (Fig. S5 of [1]).

Rietveld refinements of X-ray diffraction patterns ( $\text{CuK}\alpha$ ) of the studied  $\text{TmMn}_{6-x}\text{Fe}_x\text{Sn}_6$  stannides reveal a slight under-stoichiometry in Tm ( $\approx 5\%$ ) within the Fe-rich alloys (Table S2 of [1]), which is reminiscent of that observed in the ternary  $\text{TmFe}_6\text{Sn}_6$  parent stannide [25].

#### IV. MAGNETIC PROPERTIES OF $\text{TmMn}_{6-x}\text{Fe}_x\text{Sn}_6$

Figure 3 shows the thermal variation of the magnetization of  $\text{TmMn}_{6-x}\text{Fe}_x\text{Sn}_6$  stannides, either Mn-rich ( $x = 0.4, 0.6, 1.2$ ) or Fe-rich ( $x = 4.25, 4.5, 5.0$ ). Table S3 of [1] gives values of some magnetic characteristics of these stannides. Néel temperatures are clearly evidenced in Mn-rich stannides through pronounced local maxima that are much more

marked than in Fe-rich stannides. The magnetization jump observed around 270K in Mn-rich stannides arises from the ferromagnetic  $(\text{Mn,Fe})_{2-x}\text{Sn}$  impurity. The low-temperature thermal variations of the magnetization of  $\text{TmMn}_{6-x}\text{Fe}_x\text{Sn}_6$  alloys are presented in Fig. 3b.  $\text{TmMn}_{5.4}\text{Fe}_{0.6}\text{Sn}_6$  shows a two-step increase of the magnetization upon cooling while  $\text{TmMn}_{4.8}\text{Fe}_{1.2}\text{Sn}_6$  displays a pronounced ferromagnetic-like transition. In contrast, the other stannides show only minor magnetization changes at low temperature. The magnetization curves of  $\text{TmMn}_{5.6}\text{Fe}_{0.4}\text{Sn}_6$  and  $\text{TmMn}_{1.75}\text{Fe}_{4.25}\text{Sn}_6$  comprise a smooth peak near 25 K. In addition, a slope change occurs near 8 K for  $\text{TmMn}_{1.5}\text{Fe}_{4.5}\text{Sn}_6$  and  $\text{TmMn}_{1.75}\text{Fe}_{4.25}\text{Sn}_6$ .

The field dependences of the magnetization at 4.2 K are shown in Fig. 3c for the six studied stannides. They were measured immediately after recording the isofield data. The curves of the alloys with  $x = 0.4$  and  $0.6$  are characterized by a marked irreversible upturn at a critical field close to  $\mu_0 H_{\text{crit}} \sim 0.9$  T and by a non-zero remnant magnetization. This is likely due to the anisotropy of the magnetically ordered Tm sublattice. The  $\text{TmMn}_{4.8}\text{Fe}_{1.2}\text{Sn}_6$  stannide exhibits a spontaneous magnetization, suggesting that  $\mu_0 H_{\text{crit}}$  would be lower than 0.05 T, the field under which the thermomagnetization data were recorded. The three Fe-rich stannides do not exhibit any remnant magnetization whereas the curves of  $\text{TmMn}_{1.75}\text{Fe}_{4.25}\text{Sn}_6$  and  $\text{TmMn}_{1.5}\text{Fe}_{4.5}\text{Sn}_6$  display a more or less pronounced reversible field-dependent transition. This suggests field-induced modifications in the M sublattice.

## V. NEUTRON DIFFRACTION

### A. Mn-rich $\text{TmMn}_{6-x}\text{Fe}_x\text{Sn}_6$ stannides

Fig. 4 shows the thermal evolution of the neutron diffraction patterns of the three Mn-rich  $\text{TmMn}_{6-x}\text{Fe}_x\text{Sn}_6$  solid solutions ( $x = 0.4, 0.6, 1.2$ ).

At high temperature, above about 20-50 K, the three patterns display only the  $(0\ 0\ 1/2)$  and  $(0\ 0\ 3/2)$  peaks characteristic of the antiferromagnetic AFII structure in addition to the nuclear peaks. The AFII structure is built upon ferromagnetic kagome layers with the moments in the kagome plane (Fig. 2). The interlayer coupling is ferromagnetic through the M-Sn(2e)-Sn(2d)-Sn(2e)-M slab and antiferromagnetic through the M-(Tm-Sn(2c))-M yielding the  $++--$  sequence (i.e. a magnetic cell twice as large as the chemical one along the c-axis). This structure, which occurs only above 324 K in  $\text{TmMn}_6\text{Sn}_6$  [24], is thus stabilized by the substitution of Mn with Fe in Mn-rich solid solutions. The refined parameters near  $T \sim 90$  K are given in Table S4 of [1] while the corresponding neutron patterns are shown in Fig. S4 of [1]. Near  $T \sim 90$  K, the M moment magnitude refines to  $\mu_M \sim 2.2 \mu_B$ , as generally

observed in Mn or Fe based 1-6-6 stannides [16, 17, 20-21]. The refined Fe content is close to the nominal one.

The features of the low-temperature patterns strongly depend on the Fe content (Fig. 4). They are related to the magnetic ordering of the Tm sublattice. The diffraction patterns arise from a mixture of several magnetic phases. Because the study of  $^{119}\text{Sn}$  hyperfine magnetic fields (Sec. VI) only deals with magnetic structures where only the M sublattice is ordered, the detailed analysis of the low-temperature neutron diffraction patterns is beyond the scope of the present paper. We limit ourselves to a brief comment on these patterns (Fig. 4).

Upon cooling below  $\sim 20$  K, the patterns of  $\text{TmMn}_{4.8}\text{Fe}_{1.2}\text{Sn}_6$  mainly display an increase of the (1 0 0) and (1 0 1) peak intensities and the emergence of an additional peak without significant change in the intensity of the (0 0 1/2) and (0 0 3/2) peaks. The additional peak can be indexed as a (1 0 1)<sup>+</sup> satellite with a propagation vector (0 0  $q_z \approx 0.34$ ). Upon cooling, the neutron patterns of  $\text{TmMn}_{5.4}\text{Fe}_{0.6}\text{Sn}_6$  also show the appearance of incommensurate peaks without significant change in the intensity of the AFII peaks but with no magnetic intensity on the top of the (101) nuclear peaks. We observe the successive growths of the (101)<sup>+</sup> satellite ( $q_z \approx 0.28$ ) below ca.  $T = 29\text{K}$  and of the (101)<sup>+</sup> satellite ( $q_z \approx 0.24$ ) below ca.  $T = 20\text{K}$ . This feature is likely related to the two-step variation of the magnetization at low temperature (Fig. 3). By contrast, the low-temperature patterns below  $\sim 50$  K of  $\text{TmMn}_{5.6}\text{Fe}_{0.4}\text{Sn}_6$  are characterized by a strong reduction of the intensities of the AFII peaks concomitant with the growth of a set of magnetic satellites that can be indexed with a propagation vector (0 0  $q_z \approx 0.24$ ).

### B. Fe-rich $\text{TmMn}_{6-x}\text{Fe}_x\text{Sn}_6$ stannides

The thermal evolutions of neutron diffraction patterns of the three Fe-rich  $\text{TmMn}_{6-x}\text{Fe}_x\text{Sn}_6$  solid solutions ( $x = 4.25, 4.5, 5.0$ ) are shown in Fig 4.

No superlattice lines are observed. All diffraction peaks can be indexed on the basis of the  $\text{HfFe}_6\text{Ge}_6$ -type cell. All patterns are characterized by a significant intensity of the (1 0 1) line though the corresponding nuclear structure factor is very weak (see Sec. III). This line is characteristic of the AFI antiferromagnetic structure usually adopted by the Fe moments in  $\text{RFe}_6\text{Sn}_6$ . This structure consists of ferromagnetic kagome planes stacked along the c-axis with the + - + - sequence (Fig. 2). The missing (0 0 1) peak in  $\text{TmMn}_{1.0}\text{Fe}_{5.0}\text{Sn}_6$  indicates that the magnetic moment is aligned along the c-axis. In contrast, the patterns of the two other Fe-

rich stannides ( $x = 4.25$  and  $4.50$ ) show that the  $(0\ 0\ 1)$  intensities vary strongly with temperature. These variations show that the moment direction deviates markedly from the  $c$ -axis. The refinements were carried out with a variable angle  $\theta$  between the direction of the moments and the  $c$ -axis. The temperature dependence of the angle  $\theta$  is presented in Fig. 5. The refined parameters and R-factors are given in Table S5 of [1] while the observed and calculated patterns are shown in Fig. S5 of [1].

The patterns of the three Fe-rich stannides do not exhibit any additional significant change at low temperature, suggesting that the Tm sublattice is not ordered, at least above 1.6 K as in  $\text{TmFe}_6\text{Sn}_6$  [25]. Therefore, the weak low-temperature anomalies in their magnetization curves (Fig. 3) are due to magnetic impurities (section IV).

## VI. $^{119}\text{Sn}$ HYPERFINE MAGNETIC FIELDS IN $\text{RMn}_{6-x}\text{Fe}_x\text{Sn}_6$ (R=rare earth)

Random vectors are denoted hereafter in bold underlined italic fonts while their realizations are in bold italic fonts. The hyperfine magnetic field model, which is described below, was first successfully applied to  $^{119}\text{Sn}$  hyperfine magnetic fields measured in distannides  $\text{MSn}_2$  ( $M=\text{Mn}, \text{Fe}$ ) [29-33]. They were seen later to be consistent with theoretical results outlined below.

### A. Some literature results about $^{119}\text{Sn}$ transferred hyperfine magnetic fields in $\text{HfFe}_6\text{Ge}_6$ -type $\text{RMn}_6\text{Sn}_6$ stannides

Explanations of the various contributions to the  $^{119}\text{Sn}$  hyperfine magnetic fields in  $\text{HfFe}_6\text{Ge}_6$ -type  $\text{RMn}_6\text{Sn}_6$  stannides (R=Li and Mg, Zr, Hf) were obtained from first-principles electronic structure calculations [13, 17]. Hybridization between metalloid  $p$  states and transition-metal  $d$  states leads to bonding and antibonding hybrids situated at the bottom and at the top of the transition-metal  $d$  band, respectively [17]. The “ $s$ ” symmetry states of Sn atoms exhibit two regions with different polarization signs, going from negative at low energy to positive at an energy larger than the Fermi energy. Bonding states with a preferential occupation by minority spin states corresponds to the low energy part while the reverse holds for antibonding states at higher energy. The total Fermi contact contribution, which arises from the finite spin density of  $5s$  electrons at  $^{119}\text{Sn}$  nuclei, is the sum of a negative contribution due to the bonding states and of a positive contribution due to the antibonding states. Theoretical calculations show that the transferred hyperfine magnetic fields in the

previous  $\text{RMn}_6\text{Sn}_6$  stannides are negative, i.e. their directions are opposite to the directions of the magnetic moments of the first Mn neighbors (or to the directions of their sums) [17].

Besides the Fermi contact term, transferred hyperfine magnetic fields include a negligible orbital contribution [17] and a small lattice dipolar contribution (less than 1 T), due to the moments of neighboring atoms. The transferred hyperfine magnetic fields include also a local dipolar contribution arising from the non-spherical valence p spin density of tin hybridized with the spin-polarized d states of transition metal atoms. The latter dipolar part of the transferred field, which is simply explained as being due to the spin density of valence p electrons localized in each Mn-Sn bond, can be as large as several Tesla for Sn atoms. The lattice dipolar field due to the first nearest magnetic moments and the previous local dipolar field are formally identical. A hand-waving argument is as follows: the local term defined above is by far larger than the lattice term because of the typical  $r^{-3}$  distance dependence of dipolar fields. The dipolar field we consider is represented by the left term of Eq. 1. A priori, it is not collinear with the contact field.

Both the separation between bonding and antibonding states and the 5s spin polarization increase when the Mn-Sn distance decreases. The M-Sn(2h) distances at 300K, for h=c, d, e, in  $\text{TmMn}_{6-x}\text{Fe}_x\text{Sn}_6$  stannides studied herein, are respectively  $\approx 2.57$ , 2.61 and 2.86 Å in Mn-rich stannides and  $\approx 2.57$ , 2.56 and 2.80 Å in Fe-rich stannides, for any  $x$  in the two investigated Fe ranges. Thus, the measured hyperfine magnetic field at the Sn(2e) site is expected to be smaller than those measured at Sn(2d) or/and at Sn(2c) sites. However, this occurs only if the sums of the first M nearest neighbor moments of the last two sites differ from zero (Eq. (1) below).

## **B. An explicit simple model of $^{119}\text{Sn}$ transferred hyperfine magnetic fields applied to various stannides**

The present study of hyperfine magnetic fields in stannides, with a  $\text{HfFe}_6\text{Ge}_6$ -type structure, is restricted to “high” temperatures for which only M (Mn, Fe) magnetic moments are ordered. The studied stannides with AFI and AFII structures might be looked at as “pseudo-binary alloys” of Mn and Fe atoms in parallel kagome planes, probed locally by  $^{119}\text{Sn}$  atoms. The  $^{119}\text{Sn}$  hyperfine magnetic fields,  $\mathbf{B}_M^{(2h)}$  in  $\text{TmMn}_{6-x}\text{Fe}_x\text{Sn}_6$  pseudo-binary alloys are modelled by Eq. (1). On the left, a vector sum of anisotropic dipolar hyperfine

magnetic fields, and on the right a vector sum of Fermi contact isotropic hyperfine magnetic fields, both due to the six M first nearest neighbors of the considered tin site:

$$\mathbf{B}_M^{(2h)} = \sum_{i=1}^6 A_{aMi}(2h) \left[ \mathbf{u}_{Mi} (\boldsymbol{\mu}_{Mi} \cdot \mathbf{u}_{Mi}) - \frac{1}{3} \boldsymbol{\mu}_{Mi} \right] + \sum_{i=1}^6 A_{isMi}(2h) \boldsymbol{\mu}_{Mi} \quad (1)$$

The hyperfine magnetic fields we measure are the moduli of  $\mathbf{B}_M^{(2h)}$ . The conversion constants  $A_{aMi}(2h)$ ,  $A_{isMi}(2h)$  ( $h=c, d, e$ ), from magnetic moments into respectively anisotropic and isotropic hyperfine magnetic fields, depend on the studied stannide, on the considered tin site and on the nature of its  $i^{\text{th}}$  M nearest neighbor. Fig. S5 of [1] exemplifies some constituents of Eq. (1). As mentioned above, the  $^{119}\text{Sn}$  hyperfine magnetic fields are negative in  $\text{HfFe}_6\text{Ge}_6$ -type  $\text{RMn}_6\text{Sn}_6$  stannides [17] as are then the isotropic coefficients,  $A_{isMn}(2h)$ .

### C. Anisotropic and isotropic constants in $\text{HfFe}_6\text{Ge}_6$ -type $\text{RMn}_6\text{Sn}_6$ stannides

The anisotropic fractions of the total transferred hyperfine magnetic fields are measured to be almost negligible fractions,  $\sim 3$  to  $4\%$ , of the total hyperfine magnetic fields for Sn(2d) and Sn(2c) sites in  $\text{RMn}_6\text{Sn}_{6-x}\text{X}_x$  ( $\text{R}=\text{Y, Tb, Er, X}=\text{In, Ga}$ ) [21]. As the hyperfine magnetic fields are negative (Sec. VIA), the  $A_{aMn}(2h)$ 's and the  $A_{isMn}(2h)$ 's, which have the same sign for all Sn sites [21] are negative.

In a series of fourteen  $\text{RMn}_6\text{Sn}_6$  stannides with ferromagnetically coupled Mn moments in (001) kagome planes, transferred hyperfine magnetic fields at Sn(2d) sites range from 30 T to 33.4 T, at  $T \leq 7$  K. In these stannides, R atoms are not all rare earth elements ( $\text{R}=\text{Li, Mg, Zr, Hf, Sc, Y, Gd, Tb, Dy, Ho, Er, Tm, Yb, Lu}$  [13, 17, 18]). Further, Mn magnetic moments have similar values at low temperature,  $\mu_{\text{Mn}} \sim 2.5(3) \mu_{\text{B}}$ , and similar relative orientations. This rather narrow distribution of hyperfine magnetic fields is consistent with the smallness of anisotropic constants as compared to isotropic constants. Although large, the previous hyperfine magnetic fields are much smaller than the one of 57 T measured at  $^{119}\text{Sn}$  impurities on Gd sites in hexagonal  $\text{GdCo}_5$  at 5 K [34].

#### D. Additional assumptions about $A_{isM}(2h)$ and $A_{aM}(2h)$ constants in $\text{TmMn}_{6-x}\text{Fe}_x\text{Sn}_6$

The lack of experimental or theoretical information about possible local distortions produced by the substitution of Mn with Fe in  $\text{TmMn}_{6-x}\text{Fe}_x\text{Sn}_6$  pseudo-binary alloys, in particular in the Fe-rich range, leads us to make additional assumptions on the parameters associated with the six Sn(2h)-M bonds of any tin site:

a) The anisotropic and isotropic constants  $A_{aMn}(2h)$  and  $A_{isMn}(2h)$  are supposed to be identical for all Sn(2h)-Mn bonds as are  $A_{aFe}(2h)$  and  $A_{isFe}(2h)$  for all Sn(2h)-Fe bonds. The latter are a priori different from the former and all may depend on  $x$ .

b) All the projections of unit vectors carried by Sn(2h)-Mn bonds (Fig. 1 and Fig. S5 of [1]) on the c-axis are assumed to have the same lengths. The same assumption holds for all the projections onto the ab plane. Similar assumptions apply to all Sn(2h)-Fe bonds but the lengths differ a priori from the previous ones. These lengths are denoted respectively as  $u_{zM}(2h)$  (c-axis) and  $u_{abM}(2h)$  (ab plane).

Experimental hyperfine magnetic fields (Sec. VIII) suggest that anisotropic and isotropic constants differ for Mn-rich and for Fe-rich stannides. However, as  $x/6$  varies only by  $\sim 0.13$  and by  $\sim 0.29$  in Mn-rich and in Fe-rich stannides respectively, the previous constants are seen to be essentially independent of  $x$  in each range. Finally, the projections of the above unit vectors may vary, though moderately, with temperature, at most 300 K.

#### E. Probabilities of configurations of M atoms around Sn atoms in $\text{TmMn}_{6-x}\text{Fe}_x\text{Sn}_6$

Sn(2h) (h=c, d, e) have all six M first nearest neighbors. For a random distribution of M atoms on kagome lattices, the probability  $P(p)$  that a Sn(2h) atom (named hereafter  $\text{Sn}_{2h}(p)$ ) has  $p$  Fe atoms and  $6-p$  Mn atoms as nearest neighbors, is simply given by a classical binomial distribution which writes:

$$P(p) = \binom{6}{p} \left(\frac{x}{6}\right)^p \left(1 - \frac{x}{6}\right)^{6-p} \quad (p = 0, 1, \dots, 6) \quad (2)$$

where  $\binom{6}{p}$  is a binomial coefficient. Table S6 of [1] gives the most significant values of  $P(p)$  for the different pseudo-binary alloys we studied. The number of configurations of  $p$  Fe

neighbors of Sn(2c) or of Sn(2d) atoms, contained in a single kagome plane,  $A^{(1)}(p)$ , or in two kagome planes,  $A^{(2)}(p)$ , are further given in Table S7 of [1].

## VII. PREDICTED $^{119}\text{Sn}$ HYPERFINE MAGNETIC FIELDS IN $\text{RMn}_{6-x}\text{Fe}_x\text{Sn}_6$ STANNIDES

The considered magnetic structures are described from a stacking of parallel kagome planes, each with ferromagnetically coupled transition metal atoms M (Secs VA and VB) whose moment magnitudes  $\mu_M$  are either equal to  $\mu_{\text{Mn}}$  or to  $\mu_{\text{Fe}}$ .

### A. General expressions of hyperfine magnetic fields in $\text{RM}_6\text{Sn}_6$

#### 1. Anisotropic hyperfine magnetic fields in $\text{RM}_6\text{Sn}_6$

The contribution of  $K^+$  to anisotropic hyperfine magnetic fields at Sn(2h) sites,  $\mathbf{B}_{aM}^{(2h)}(K^+)$ , is calculated in Sec VA of [1] from the left sum in Eq. (1) to be:

$$\mathbf{B}_{aM}^{(2h)}(K^+) = A_{\text{eff},M}(2h) [\alpha(2h)/2] \times \{ \boldsymbol{\mu}_M - 3\boldsymbol{\mu}_{zM} \} \quad (3)$$

where  $\alpha(2h) = 1, 1, 2$ , for  $h=c, d, e$  respectively, and  $\boldsymbol{\mu}_{zM}$  is the projection of the magnetic moment  $\boldsymbol{\mu}_M$  on the [001] axis. Further,  $A_{\text{eff},M}(2h) = A_{aM}(2h) (1 - 3u_{zM}^2(2h))$  where  $u_{zM}^2(2h)$  is the square of the length of the projection on the c-axis of a unit vector carried by any Sn(2h)-M bond.

#### 2. Total hyperfine magnetic fields in $\text{RM}_6\text{Sn}_6$ ( $M$ is either Mn or Fe)

The moments  $\boldsymbol{\mu}_M$  of M atoms, in a single kagome plane or in two successive kagome planes, are assumed to make an angle  $\theta$  with the c-axis at a temperature  $T$  made explicit in Eqs (4) and (5). The latter equations hold for those Sn(2h) sites which are sandwiched between two ferromagnetically coupled kagome planes and, in all cases, for Sn(2e) sites which are bound to a single plane. Besides  $h=e$ ,  $h$  is:

- a)  $h=c, d$  in ferromagnetic  $\text{RM}_6\text{Sn}_6$  stannides (examples are given in [21]).
- b)  $h=d$  in  $\text{RM}_6\text{Sn}_6$  stannides with the AFII antiferromagnetic structure (Fig.2).

An orthonormal coordinate system with unit vectors  $(\mathbf{u}_x, \mathbf{u}_y, \mathbf{u}_z)$ , where  $\mathbf{u}_z=[001]$ , (Fig. S5 of [1]) is defined in Sec. V of [1]. The total angle dependent hyperfine magnetic fields at Sn(2h) sites defined above at a temperature  $T$ ,  $\mathbf{B}_{M,T}^{(2h)}(\theta)$ , are obtained in the  $(\mathbf{u}_x, \mathbf{u}_y, \mathbf{u}_z)$  reference system from Eqs. (1) and (3) to be:

$$\mathbf{B}_{M,T}^{(2h)}(\theta) = \mathbf{B}_{M,T}^{(2h)}(90^\circ) \sin \theta \times \mathbf{u}_x + \mathbf{B}_{M,T}^{(2h)}(0^\circ) \cos \theta \times \mathbf{u}_z \quad (4)$$

Eq. (4) and some of its applications are discussed in Sec. VB of [1]. For Sn atoms, with six identical nearest neighbors ( $M=\text{Mn}$  or  $\text{Fe}$ ), Eqs (1) and (3) yields the explicit expressions of  $\mathbf{B}_{M,T}^{(2h)}(90^\circ)$  and of  $\mathbf{B}_{M,T}^{(2h)}(0^\circ)$  as:

$$\begin{cases} \theta = 90^\circ \Rightarrow \mathbf{B}_{M,T}^{(2h)}(90^\circ) = (6A_{isM}(2h) + A_{aeff,M}(2h)) \mu_M(T) \\ \theta = 0^\circ \Rightarrow \mathbf{B}_{M,T}^{(2h)}(0^\circ) = (6A_{isM}(2h) - 2A_{aeff,M}(2h)) \mu_M(T) \end{cases} \quad (5)$$

In general, the direction of the total hyperfine magnetic field, calculated from Eq. (1), deviates from the moment direction in collinear magnetic structures except if they are easy-plane or easy-axis (Fig. 2).

### B. Hyperfine magnetic fields in stannides $\text{TmMn}_{6-x}\text{Fe}_x\text{Sn}_6$

Hyperfine magnetic fields at tin sites in  $\text{TmMn}_{6-x}\text{Fe}_x\text{Sn}_6$  change when 6 Mn neighbors are replaced by  $6-p$  Mn neighbors and  $p$  Fe neighbors ( $p=0, \dots, 6$ ). Therefore, the vector hyperfine magnetic field at a given tin site Sn(2h) is a random vector,  $\underline{\mathbf{B}}_M^{(2h)}$ , which takes a set of vector values associated with the many possible ways of distributing six Mn and Fe first nearest neighbors around the given tin site for the given Fe content.

The anisotropic hyperfine magnetic field  $\underline{\mathbf{B}}_{aM}^{(2h)}$ , is a sum of six random vectors  $\underline{\mathbf{X}}_{Mi}$  ( $i=1, \dots, 6$ ) associated with dipolar HMF's. The two possible values of each of the six  $\underline{\mathbf{X}}_{Mi}$  are  $\underline{\mathbf{X}}_{Mi} = A_{aMi}(2h) \times \{ \mathbf{u}_{Mi} (\boldsymbol{\mu}_{Mi} \cdot \mathbf{u}_{Mi}) - \boldsymbol{\mu}_{Mi}/3 \}$  where  $Mi$  is either Mn or Fe (Eq. (1)). The random hyperfine magnetic field at site Sn(2h) is then  $\underline{\mathbf{B}}_M^{(2h)} = \sum_{i=1}^6 ( \underline{\mathbf{X}}_{Mi} + A_{isMi}(2h) \underline{\boldsymbol{\mu}}_{Mi} )$  where the last term is the isotropic hyperfine magnetic field which depends on a random

magnetic moment  $\underline{\mu_{Mi}}$  either equal to  $\mu_{Mni}$  or to  $\mu_{Fei}$ . Further calculations are described in Sec. VIA of [1].

For those Sn(2h) atoms, which have either six Mn or six Fe first nearest neighbors, the magnetic hyperfine fields we consider have well-defined values. For M being either Mn or Fe everywhere in the next three relations, we write the anisotropic fields from Eq. (1):

$$\mathbf{B}_{aM}^{(2h)} = \sum_{i=1}^6 A_{aM} (2h) \times \{ \mathbf{u}_i (\boldsymbol{\mu}_M \cdot \mathbf{u}_i) - \mu_M / 3 \} = \sum_{i=1}^6 \mathbf{X}_{Mi} \quad (6)$$

the isotropic fields,  $\mathbf{B}_{isM}^{(2h)} = 6A_{isM} (2h) \boldsymbol{\mu}_M$ , and the total hyperfine magnetic fields:

$$\mathbf{B}_M^{(2h)} = \mathbf{B}_{aM}^{(2h)} + \mathbf{B}_{isM}^{(2h)} \quad (7)$$

All sites (6i), occupied at random by M atoms in  $\text{TmMn}_{6-x}\text{Fe}_x\text{Sn}_6$ , are statistically equivalent. However, from the point of view of tin ‘‘probes’’, the statistical equivalency of their six M first nearest neighbors depends further on local magnetic structures. The assumptions done in Sec. VID lead us to distinguish two main cases, relevant for the AFI and AFII magnetic structures, for which the six first nearest neighbor sites of the considered tin atoms are:

1) statistically equivalent. This is the case for Sn(2e) sites whose six M first nearest neighbors are always ferromagnetically coupled and are thus interchangeable. This is also the case of tin sites sandwiched between two ferromagnetically coupled kagome planes (case a of Sect. VIIA2).

2) statistically inequivalent. This holds for tin sites sandwiched between two kagome planes, which are not themselves ferromagnetically coupled. The six neighboring sites are then split into two groups of three equivalent sites, each in a ferromagnetic kagome plane. Then, it is necessary to know not only the total number  $p$  of Fe first nearest neighbors but also their repartition among the two neighboring kagome planes ( $p_1, p_2$ ).

For a given Fe content  $x$  and a random substitution of Mn atoms with Fe atoms, the average hyperfine magnetic fields at Sn(2h) atoms are calculated in Sec. VI of [1] as a function of  $p$  (and if required of ( $p_1, p_2$ )). A comparison of experimental fields with the moduli of their calculated counterparts is thus possible.

### 1. Six statistically equivalent first nearest neighbor sites

Experimental results (Sec. VIII) show only a weak hyperfine magnetic field dependence on  $x$  for a given number  $p$  of their Fe nearest neighbors for stannides which belong to the same class, i.e. either to the Mn-rich class or to the Fe-rich class. The calculated average hyperfine magnetic fields,  $\mathbf{B}_M^{(2h)}(p)$  ( $x$  is omitted), yields predicted hyperfine magnetic fields,  $B_{pred}^{(2h)}(p)$ , the modulus of  $\mathbf{B}_M^{(2h)}(p)$ , which are just those to which experimental hyperfine magnetic fields,  $B_{exp}^{(2h)}(p)$ , have to be compared.

With the set of assumptions described in Sec. VID, the average anisotropic and isotropic hyperfine magnetic fields, and thus the average total hyperfine magnetic fields at sites  $\text{Sn}_{2h}(p)$ , where  $p$  is a fixed number, are calculated in Sec. VIA of [1]. Eqs (24), (25) and (26) of [1] give explicitly the separate anisotropic (subscript,  $aM$ ) and isotropic ( $isM$ ) contributions to the total ( $M$ ) hyperfine magnetic field of  $\text{Sn}(2h)$  atoms which have  $p$  Fe first nearest neighbors,  $\mathbf{B}_{aM}^{(2h)}(p)$ ,  $\mathbf{B}_{isM}^{(2h)}(p)$ ,  $\mathbf{B}_M^{(2h)}(p)$ . The average total field (Eq. (26) of [1]):

$$\mathbf{B}_M^{(2h)}(p) = \mathbf{B}_{Mn}^{(2h)} - p \times \left\{ \mathbf{B}_{Mn}^{(2h)} - \mathbf{B}_{Fe}^{(2h)} \right\} / 6 \quad (8)$$

is then a weighted sum, linear in  $p$ , of the two hyperfine magnetic fields  $\mathbf{B}_{Mn}^{(2h)}$  and  $\mathbf{B}_{Fe}^{(2h)}$  (Eq. (7)), of  $\text{Sn}(2h)$  atoms with respectively six Mn and six Fe first nearest neighbors. Ideally, the latter fields are or would have to be measured both at the same temperature for the given Fe content.

### 2. Two groups of three statistically equivalent first nearest neighbor sites

For  $\text{Sn}(2h)$  atoms, sandwiched between two kagome planes antiferromagnetically coupled, the index  $h$  is  $h=c, d$  for the AFI structure while it is  $h=d$  for the AFII structure (Fig. 2). The numbers of Fe atoms in kagome planes  $K^-$  and in  $K^+$  (Fig. S5 of [1]) are denoted respectively as  $p_1$  and  $p_2=p-p_1$  (Table S7 of [1]). In easy-axis AFI and in easy-plane AFII, the isotropic and anisotropic contributions to total hyperfine magnetic fields are collinear. Further, if the anisotropic hyperfine magnetic fields are negligible as compared to the isotropic ones, then the predicted experimental hyperfine magnetic fields reduce to (Eq. (28) of [1]):

$$B_{pred}^{(2h)}(N_{Fe}) = N_{Fe} \times \left| A_{isMn}(2h)\mu_{Mn} - A_{isFe}(2h)\mu_{Fe} \right| \quad (9)$$

where  $N_{Fe} = |p_2 - p_1|$  plays the role of an “effective” number of Fe nearest neighbors. Relations, which include anisotropic terms, are given in Sec. VIB of [1]. In all cases, the calculated hyperfine magnetic fields vary linearly with  $N_{Fe}$ .

Finally, the dispersion of the distribution of the modulus of the random magnetic hyperfine field  $\underline{B}_M^{(2h)}$  contributes to Mössbauer line broadening, possibly asymmetrical to some extent.

### VIII. EXPERIMENTAL $^{119}\text{Sn}$ HYPERFINE MAGNETIC FIELDS OF $\text{TmMn}_{6-x}\text{Fe}_x\text{Sn}_6$ AND THEIR INTERPRETATION

As we measure only absolute values of hyperfine magnetic fields, we define for convenience  $A_{isM}^-(2h) = -A_{isM}(2h)$  and  $A_{aM}^-(2h) = -A_{aM}(2h)$  ( $M = \text{Mn, Fe, h=c, d, e}$ ).

Sec. IVB of [1] discusses the validity of hyperfine magnetic fields as obtained from Mössbauer spectra with the assumption that first-order perturbation theory holds. It leads to conclude that anisotropic and isotropic constants are confidently calculated for tin sites whose hyperfine magnetic fields are large enough. The latter are measured at tin sites whose first nearest neighbors are ferromagnetically coupled, i.e. Sn(2e) in all stannides and Sn(2d) in Mn-rich stannides (easy-plane AFII structure).

#### A. Three Mn-rich stannides ( $x = 0.4, 0.6$ and $1.2$ ) in the easy-plane AF II state ( $T \geq 30$ K)

The easy-plane AFII type-structure (Fig. 2), which exists only above 324 K in  $\text{TmMn}_6\text{Sn}_6$  [24], is stabilized by the substitution of Mn with Fe. Fig. 6 shows observed and calculated  $^{119}\text{Sn}$  Mössbauer spectra of three  $\text{TmMn}_{6-x}\text{Fe}_x\text{Sn}_6$  stannides with  $x = 0.4, 0.6$  and  $1.2$ , recorded respectively at 55, 46 and 30 K in the AFII state while those observed at 4.2 K, with magnetically ordered Tm moments, are shown in Fig. S6 of [1]. All parameters obtained from least-squares fits are collected in Table S8 of [1].

Positive ratios  $A_{aMn}(2h)/A_{isMn}(2h) < \approx 70\%$  in  $\text{RMn}_6\text{Sn}_{6-x}\text{X}_x$  compounds ( $R = \text{Y, Tb, Er}$ ;  $X = \text{In, Ga}$ ) [21] are reported in [21] for Sn(2d) and Sn(2c) sites. They range between  $\sim 20\%$  and  $\sim 70\%$  for site Sn(2e). The isotropic contribution is thus awaited to be still the main part of the total hyperfine magnetic field in Mn-rich stannides. As  $A_{isMn}(2h)$  is negative,

$A_{aMn}(2h)$  is also negative. Both constants are conveniently written as  $A_{uM}^-(2h)$  ( $u = is, a, aeff$ ).

### 1. An estimate of $A_{isMn}^-(2d)$ from the hyperfine magnetic fields of $TmMn_6Sn_6$

The hyperfine magnetic field of Sn(2d) atoms in  $TmMn_6Sn_6$  which have thus six Mn neighbors ( $p=0$ ),  $B_{exp}^{(2d)}(0)$ , lies most likely between 30T and 33.4 T. Indeed, Table S8 of [1] shows that the measured  $B_{exp}^{(2d)}(0)$ 's appear to be independent of  $x$ , with a mean of  $31.3 \pm 0.3$ T at temperatures of 30K, 46K and 55K. The latter mean is  $31.7 \pm 0.3$ T at 4.2K. All these values are close to  $B_{exp}^{(2d)}(0) = 32.1(3)$ T measured in  $ZrMn_6Sn_6$  at 100K, which has an AFII magnetic structure above  $\approx 70$  K with  $\mu_{Mn} = 2.11 \mu_B$  [17]. The predicted hyperfine magnetic field at Sn(2d) nuclei,  $B_{pred}^{(2d)}(0)$ , is  $(6A_{isMn}^-(2d) + A_{aeff,Mn}^-(2d))\mu_{Mn}$  ( $\theta = 90^\circ$ ) as deduced from Eq. (5). Neglecting the anisotropic contribution gives  $A_{isMn}^-(2d) = B_{exp}^{(2d)}(0) / (6\mu_{Mn}) = 2.3(3) \text{ T} / \mu_B$  with  $\mu_{Mn} \sim 2.3(3) \mu_B$  at 2 K (neutron diffraction) and  $B_{exp}^{(2d)}(0) = 31.5$ T.

### 2. Sn(2d) and Sn(2e) atoms in Mn-rich $TmMn_{6-x}Fe_xSn_6$

$Sn_{2h}(p)$  atoms ( $h=d, e$ ) with  $p$  Fe neighbors, are characterized, among others, by their experimental hyperfine magnetic fields,  $B_{exp}^{(2h)}(p)$  and by their relative areas  $f_{2h}(p)$  (Table S6 of [1]), or equivalently by their relative fractions.

The sextets with the largest hyperfine magnetic fields,  $\sim 31.5$ T, are attributed consistently to Sn(2d) sites with six Mn neighbors (Sec. VIIIA1). Sextets with external peaks at  $\sim -18$  mm/s and  $\sim +21$  mm/s, are observed for  $x = 0.4, 0.6$  and  $1.2$  but not for  $ZrMn_6Sn_6$  (Fig. 6). They are attributed to Sn(2d) atoms, surrounded by 5 Mn and 1 Fe atoms. Additional sextets are associated to Sn(2d) atoms with 4Mn and 2Fe neighbors. The hyperfine magnetic fields  $B_{exp}^{(2d)}(p)$  remain almost constant with  $x$  for any of the observed values of  $p$ . Similarly, the various subspectra associated with Sn(2e) atoms, whose hyperfine magnetic fields range from  $\sim 13$  T to  $\sim 21$  T, are identified, notably from a comparison of the variations with  $x$  of their relative areas to the expected values.

The hyperfine magnetic field changes with  $p$  are predominantly due to isotropic contributions of the six first nearest neighbors of Sn atoms as suggested by first-principle calculations ([17] and Sec. VIA). We consider first the isotropic contribution where the

common direction of M moments is taken as the reference direction. The following equations are formally identical for Sn(2d) and Sn(2e) which have both six ferromagnetically coupled neighbors. The predicted absolute value of the isotropic hyperfine magnetic field, for a given Fe content  $x$  and a given temperature, is deduced from Eq. (24) of [1] to be:

$$B_{pred}^{(2h)}(p) = B_{pred}^{(2h)}(0) - p \times \Delta A_{is}(2h) \quad (10)$$

, where  $\Delta A_{is}(2h) = A_{isMn}^-(2h)\mu_{Mn} - A_{isFe}^-(2h)\mu_{Fe}$ .

In Mn-rich alloys, the predicted hyperfine magnetic fields at Sn<sub>2d</sub>( $p$ ) and Sn<sub>2e</sub>( $p$ ) sites vary linearly with  $p$  in agreement with experiment (Fig. 7). Fig. 7 indicates further that the hyperfine magnetic fields are essentially independent of  $x$  ( $x \leq 1.2$ ).

Table S8 of [1] shows that  $0 < B_{exp}^{(2h)}(p) < B_{exp}^{(2h)}(0)$  for for h=d and e and the values of  $p$  whose associated spectral areas are significant ( $0 < p \leq 3$ ,  $x \leq 1.2$ ). Thus, the  $\Delta A_{is}(2h)$  are positive, i.e.  $A_{isMn}^-(2h)\mu_{Mn} > A_{isFe}^-(2h)\mu_{Fe}$  ( $A_{isMn}^-(2h) > 0$ ) for Mn-rich stannides. The Sn<sub>2d</sub>( $p$ ) hyperfine magnetic fields are larger than those of Sn<sub>2e</sub>( $p$ ) atoms with slopes  $-\Delta A_{is}(2d) = -3.4(1)$  T and  $-\Delta A_{is}(2e) = -2.5(1)$  T. This suggests that the isotropic constants  $A_{isMn}^-(2e)$  would be at most  $\sim 0.7 A_{isMn}^-(2d)$  as the effect of an anisotropic contribution on the total hyperfine magnetic field would have to be considered for site Sn(2e) [21].

If we take  $A_{isMn}^-(2d) = 2.3(3)$  T/ $\mu_B$  (Sec. VIIIA), then the measured slope yields an estimate of  $A_{isFe}^-(2d) \sim 0.8$  T/ $\mu_B$  for  $\mu_{Fe} = \mu_{Mn} \sim 2.3\mu_B$ . The isotropic constant  $A_{isFe}(2d)$  obtained in that way is thus negative as is  $A_{isMn}(2d)$ .

The effect of an anisotropic contribution on the total hyperfine magnetic field must be considered for site Sn(2e) albeit the isotropic contribution still dominates the total hyperfine magnetic field in Mn-rich stannides all the more that the anisotropic term is  $A_{aeff,M}^-(2e)/6$  in the definition of  $A_M^-(2e)$  (Eq. (11)). The latter constant is convenient to express  $B_{pred}^{(2e)}(0) = 6A_M^-(2e)\mu_{Mn}$  from Eq. (5) for  $\theta = 90^\circ$ . From Eq. (8) and Eqs (24) to (26) of [1], the predicted experimental hyperfine magnetic field writes finally,  $B_{pred}^{(2e)}(p) = B_{pred}^{(2e)}(0) - p\Delta A_M(2e)$ . We define, for all Sn sites:

$$\begin{cases} A_M^-(2h) = A_{isM}^-(2h) + A_{a\text{eff},M}^-(2h)/6 \quad (\theta=90^\circ) \\ \Delta A_M(2h) = A_{Mn}^-(2h)\mu_{Mn} - A_{Fe}^-(2h)\mu_{Fe} \end{cases} \quad (11)$$

The difference between  $\Delta A_{is}(2e)$  and  $\Delta A_M(2e)$  is that the latter includes both isotropic and anisotropic constants. For a given  $x$ , hyperfine magnetic fields at Sn(2e) sites are then predicted to vary linearly with the number  $p$  of Fe neighbors in agreement with experiment (in Tesla),  $B_{\text{exp}}^{(2e)}(p) = 21.2 - 2.5p$  (Table I, Fig. 7). However, the two experimental values,  $B_{\text{exp}}^{(2e)}(0)$  and the slope, don't suffice to evaluate the, four in number, isotropic and anisotropic constants which appear in  $\Delta A_M(2e)$  (Eq. (11)), so that only  $A_{Mn}^-(2e)$  and  $A_{Fe}^-(2e)$  can be evaluated.

In Mn-rich stannides,  $A_{Mn}^-(2e) = 21.2/(6\mu_{Mn}) = 1.53(7)$  T/ $\mu_B$  is obtained from  $B_{\text{exp}}^{(2e)}(0)$ . From the slope 2.5 T, we calculate further that  $A_{Fe}^-(2e) = 0.44(8)$  T/ $\mu_B$ . Electronic structure calculations [17] show that the negative isotropic terms are dominant in Mn-rich stannides. Thus:  $A_{Mn}(2e) = -1.53(7)$  T/ $\mu_B$  and (Sec. VIIIA)  $A_{Fe}(2e) = -0.44(8)$  T/ $\mu_B$ .

### 3. Sn(2c) sites

Only qualitative information, further discussed in Sec. VIIIB2 of [1], can be derived because the hyperfine magnetic fields of these sites are small,  $\sim 3.5$  T (Table S8 of [1]), and their quadrupole splittings are large,  $\sim 2$  mm/s (Sec. IVB of [1]).

## B. Fe-rich stannides ( $x = 4.25, 4.5, 5, 6$ )

Fe-rich stannides have an AFI antiferromagnetic structure (Fig. 2) observed in a range of Fe content similar to the one,  $x > 3.5$ , measured in  $\text{ErMn}_{6-x}\text{Fe}_x\text{Sn}_6$  [24]. In  $\text{TmMn}_1\text{Fe}_5\text{Sn}_6$  and in  $\text{TmFe}_6\text{Sn}_6$ , M magnetic moments are aligned along the c-axis while this occurs at very low temperatures for  $x=4.25$  and  $x=4.5$  (Fig. 5).

$^{119}\text{Sn}$  Mössbauer spectra of the two stannides with  $x = 4.25, 4.5$ , recorded at three different temperatures, are shown in Fig. 8. Two spectra recorded at 4.2 K and at 300 K are shown in Fig. S7 for  $x=5$  and in Fig. S8 for  $x=6$  (Sec. XB of [1]).

Because of the AFI structure, spectra consist mainly of an intense and broad central component clearly constituted of various subspectra with small hyperfine magnetic fields, due

to Sn(2c) and Sn(2d) sites and of broad outer wings (Sec. IVB of [1]) with larger hyperfine magnetic fields associated with Sn(2e) sites. Tm atoms, which are not magnetically ordered above 1.6 K (Sec. VB), do not contribute to the measured hyperfine magnetic fields.

Only Sn(2e) atoms have six magnetic neighbours ferromagnetically coupled in a single kagome plane. For  $x=6$ , all tin sites have six Fe nearest neighbors, antiferromagnetic coupled for Sn(2c) and Sn(2d) sites, with  $N_{Fe}=0$ , which give rise to the two central doublets of Fig. S9 of [1]. The magnetic components of TmFe<sub>6</sub>Sn<sub>6</sub> spectra are due to Sn(2e) sites whose first nearest neighbours are ferromagnetically coupled. Fig. S10 of [1] shows in addition the hyperfine magnetic field distribution at the Sn(2e) sites calculated at 4.2 K. Its asymmetry is further discussed in Sec. XB of [1].

The overlaps of subspectra in the central parts of Mössbauer spectra recorded for  $x=4.25$  and  $x=4.5$ , require to constrain their relative areas during the whole fitting process (Sec. IVA of [1]). Sn(2c) and Sn(2d) peaks form a broad central component from which it is difficult to extract usable values of their hyperfine magnetic fields, as  $B_{\text{exp}}^{(2c)}$  and  $B_{\text{exp}}^{(2d)}$  are only  $\sim 4\text{-}5$  T.

The three tin sites are further considered in Secs IXB and X of [1]. We limit the following discussion to Sn(2e) sites whose hyperfine magnetic fields are large and quadrupole splittings are small (Sec. IVB of [1]). Reliable values of model parameters can then be derived from experimental results.

An overall decrease of the Sn(2e) hyperfine magnetic fields in TmMn<sub>6-x</sub>Fe<sub>x</sub>Sn<sub>6</sub> ( $x=4.25, 4.5$ ), clearly seen without fitting, on the wings of the spectra of Fig. 8, takes place when T increases from 4.2 K to 51 K ( $x=4.25$ ) or to 72 K ( $x=4.5$ ). This decrease is due primarily to the increase of the angle  $\theta$  from  $\approx 7.5(6)^\circ$  respectively to  $\approx 69^\circ$  and  $\approx 53^\circ$  (Fig. 5) as further discussed in detail in Sec. IXB of [1].

### 1. Model parameters obtained from hyperfine magnetic fields measured at 4.2 K

The linear equations, which express  $B_M^{(2e)}(p)$ , are obtained from Eq. (5) and from Eq. (8):

$$B_M^{(2e)}(p) = B_M^{(2e)}(0) + p(A_{Fe}(2e)\mu_{Fe} - A_{Mn}(2e)\mu_{Mn}) \quad (12)$$

where  $A_M(2e) = A_{isM}(2e) - A_{a\text{eff},M}(2e)/3$  ( $\theta = 0^\circ$ ) and  $B_M^{(2e)}(0) = 6A_{Mn}(2e)\mu_{Mn}$ . As shown below,  $|A_{Mn}(2e)|$  is an order of magnitude smaller than  $|A_{Fe}(2e)|$ . Therefore the sign

of  $A_{Mn}(2e)$  does not matter, all the more that observable subspectra come from Sn atoms with more than three Fe neighbors ( $p \geq 3$ , Table S6 of [1]). The hyperfine magnetic fields predicted from Eq. (12) is then written as:

$$B_{pred}^{(2e)}(p) = 6\varepsilon A_{Mn}(2e)\mu_{Mn} + p\left(|A_{Fe}(2e)|\mu_{Fe} - \varepsilon A_{Mn}(2e)\mu_{Mn}\right) \quad (13)$$

where  $\varepsilon = \text{sign}(A_{Fe}(2e))$ . The experimental hyperfine magnetic fields vary linearly with  $p$ ,  $B_{exp}^{(2e)}(p) = B_{exp}^{(2e)}(0) + p \times \Delta B_{exp}^{(2e)}$ , with positive slopes, both at 4.2 K, for  $x=4.25$ , 4.5 and 5, and at moderate temperatures (51 K and 72 K) (Fig. 7 and Table I).

The hyperfine magnetic fields  $B_{exp}^{(2e)}(6)$  at 4.2 K for  $x=4.25$ , 4.5 and 5 (20.4 T, 21.2 T and 22 T respectively) and the corresponding magnetic moments at 2 K (2.35  $\mu_B$ , 2.40  $\mu_B$  and 2.42  $\mu_B$ , Table S5 of [1]) yield the values of  $|A_{Fe}(2e)| = B_{exp}^{(2e)}(6)/(6\mu_{Fe})$  (Eq. (13)) whose mean is  $|A_{Fe}(2e)| = 1.51(5)$  T/ $\mu_B$ .

Further, the mean hyperfine magnetic field at 4.2 K, 23.2 T, of TmFe<sub>6</sub>Sn<sub>6</sub> as obtained from the hyperfine magnetic field distribution (Fig. S10 of [1]), yields  $|A_{Fe}(2e)| = 1.61(3)$  T/ $\mu_B$ . From the slope  $\Delta B_{exp}^{(2e)} = 3.3$  T, we get thus  $\varepsilon A_{Mn}(2e) = 0.08(8)$  T/ $\mu_B$  (Eq. (13)) which is an order of magnitude smaller than  $|A_{Fe}(2e)|$ . The  $|A_{Fe}(2e)|$  value at 4.2 K is shown below to be consistent with the value derived from moment rotation between 4.2 K and ~50-70 K.

## 2. Model parameters obtained from magnetic moment rotation with temperature

The variation of  $B_{exp}^{(2e)}(6)$  due to the temperature dependent angle  $\theta$  (Fig. 5) yields  $\rho_{eff,Fe}^{(2e)} = -0.80 \pm 0.06$  and  $-0.84 \pm 0.14$  for  $x=4.25$  and  $x=4.5$  respectively (Sec. IX of [1]). Negative ratios,  $\rho_{Fe}^{(2e)} = A_{a,Fe}(2e)/A_{isFe}(2e)$ , contrast with positive ratios  $A_{a,Mn}(2h)/A_{isMn}(2h)$  ( $h=c, d, e$ ) found for Mn-rich alloys [21] which imply that  $A_{a,Mn}(2h)$  is negative as is  $A_{isMn}(2h)$  [17]. Negative anisotropic and isotropic components of hyperfine magnetic fields are also found for <sup>119</sup>Sn in TmFe<sub>2</sub> [35]. The previous results suggest that the negative sign of  $\rho_{Fe}^{(2e)}$  means that

$A_{isFe}(2e)$  is now positive as is then  $B_{\text{exp}}^{(2e)}(p)$ , a fact made reasonable from the band structure calculations mentioned in Sec. IX.

The previous discussion means that  $\varepsilon=1$  in Eq. (13) for Fe-rich stannides. Values  $A_{isFe}(2e)=1.15(3)$  T/ $\mu_B$  and  $A_{aFe}(2e)=-1.18(10)$  T/ $\mu_B$  are finally calculated from  $\rho_{\text{eff},Fe}^{(2e)}$  in Sec. IX of [1].

In summary:

a) for Mn-rich stannides:  $A_{Fe}(2e)=-0.44(8)$  T/ $\mu_B$ ,  $A_{Mn}(2e)=-1.53(7)$  T/ $\mu_B$

b) for Fe-rich stannides:  $A_{Fe}(2e)=1.51(5)$  T/ $\mu_B$ ,  $|A_{Mn}(2e)|=0.08(8)$  T/ $\mu_B$

$$A_{isFe}(2e)=1.15(3) \text{ T}/\mu_B, A_{aFe}(2e)=-1.18(10) \text{ T}/\mu_B$$

The marked decrease of the magnitude of  $|A_{Mn}(2e)|$  when going from Mn-rich to Fe-rich stannides agrees with the discussion presented below. The magnitudes of Mn coefficients in Fe-rich stannides are too small to decide if they are negative or positive.

## IX. DISCUSSION AND CONCLUSIONS

Magnetic structures of Mn-rich ( $x=0.4, 0.6, 1.2$ ) and of Fe-rich ( $x=4.25, 4.5, 5$ )  $\text{TmMn}_{6-x}\text{Fe}_x\text{Sn}_6$  stannides, with  $\text{HfFe}_6\text{Ge}_6$ -type structure, were determined by magnetization measurements and neutron diffraction. The low-temperature magnetic properties of Mn-rich stannides (below  $\sim 20$  K) are complex and originate from a mixture of several magnetic phases, some being incommensurate. Our magnetic studies show that Tm atoms are not magnetically ordered at temperatures higher than  $\sim 20$  to 50 K in Mn-rich stannides, ( $x = 0.4, 0.6, 1.2$ ) and higher than 1.6 K in Fe-rich stannides. In these temperature ranges, Mn-rich and Fe-rich stannides have different antiferromagnetic structures, AFII and AFI respectively. In both cases, Mn and Fe atoms of any kagome plane are ferromagnetically coupled. Structure AFII is such that two successive kagome planes are either ferromagnetically or antiferromagnetically coupled while they are antiferromagnetically coupled for structure AFI.

The focus of the study of  $^{119}\text{Sn}$  hyperfine magnetic fields was put on stannides which have either an AFII or an AFI magnetic structure. The hyperfine magnetic fields are modelled as sums of anisotropic dipolar contributions and of isotropic contributions. Both are due to magnetic moments of the six first nearest neighbors (Mn or Fe) of any tin site. The model includes isotropic and anisotropic constants, four in number, associated respectively with Sn-

Mn and with Sn-Fe bonds. With the assumption of a random substitution of Mn with Fe, the model predicts linear dependencies of average hyperfine magnetic fields:

a) Sn(2d) atoms in Mn-rich stannides (AFII) and Sn(2e) atoms in all stannides have six ferromagnetically coupled neighbors, respectively in two successive kagome planes and in a single kagome plane. Their average hyperfine magnetic fields vary linearly with the number  $p$  of their first Fe nearest neighbors ( $0 \leq p \leq 6$ ).

b) if a given Sn atom is sandwiched between two antiferromagnetically coupled kagome planes, then its associated average hyperfine magnetic field is predicted proportional to  $N_{Fe} = |p_2 - p_1|$ , where one of the two kagome planes contains  $p_1$  nearest neighbor Fe atoms and the other  $p_2$ . This is the case of Sn(2c) atoms in Mn-rich stannides (AFII) and of Sn(2c) and Sn(2d) atoms in Fe-rich stannides (AFI).

Significant experimental results from  $^{119}\text{Sn}$  Mössbauer spectra, associated with the largest hyperfine magnetic fields (Sn(2d) in Mn-rich stannides and Sn(2e) in all cases), agree with these predictions. Importantly, the slope of the line of experimental Sn(2e) hyperfine magnetic fields versus  $p$  is negative in Mn-rich stannides and positive in Fe-rich stannides. Experimental information enables us to determine only two linear combinations of the four constants mentioned above. In Fe-rich stannides, consistent values of the latter combinations are deduced on the one hand from the experimental Sn(2e) hyperfine magnetic fields versus  $p$  at 4.2 K and on the other hand from the variations of the largest hyperfine magnetic fields due to a temperature-dependent rotation of Mn and of Fe magnetic moments.

Our experimental results for Mn-rich stannides agree with published results which show that the isotropic constants of Sn-Mn bonds are all negative. Further, the ratios of Sn-Mn anisotropic constants to their associated isotropic constants are positive. Therefore, the anisotropic constants are negative too.

In Fe-rich stannides, the temperature-dependent rotation of Mn and of Fe magnetic moments enables us to calculate separately the anisotropic and isotropic constants of Sn(2e)-Fe bonds whose ratio is concluded to be negative. A change of sign of the isotropic constant of Sn(2e)-Fe bonds explains a change of sign of the resulting average hyperfine magnetic fields and of the slope of their variation with  $p$ .

A rigid band approach was used to account for a change from large negative tin hyperfine magnetic fields in  $\text{RMn}_6\text{Sn}_6$  to positive germanium hyperfine magnetic fields in  $\text{RFe}_6\text{Ge}_6$  [36]. Only the bonding s-d hybrids are occupied in Mn-based stannides while the supplementary valence electrons brought by Fe partly populate the antibonding states in Fe-

based germanides [36]. This evolution leads to a change of hyperfine magnetic field signs. An evolution from negative Sn(2e) hyperfine magnetic fields in Mn-rich stannides to positive Sn(2e) hyperfine magnetic fields in Fe-rich stannides is in line with the previous explanation. The range of Fe content in which this change of sign occurs remains to be investigated. In a similar way, we observe that the magnitudes of the constants associated with Sn(2e)-Mn bonds decrease strongly when going from Mn-rich to Fe-rich stannides.

### ACKNOWLEDGMENTS

We are indebted to the ILL (Grenoble, France) for the provision of research facilities (Exp. n\_5-31-1854) and to Dr. B. Ouladdiaf for his help during the measurements.

### REFERENCES

- [1] See Supplemental Material at <http://link.aps.org/supplemental/...> for further information on crystallographic characteristics of  $\text{TmMn}_{6-x}\text{Fe}_x\text{Sn}_6$  stannides, on magnetization and neutron diffraction results, on fitting assumptions of  $^{119}\text{Sn}$  Mössbauer spectra, on models of  $^{119}\text{Sn}$  transferred hyperfine magnetic fields in Mn-rich and in Fe-rich stannides and on their contribution to the analysis of experimental results.
- [2] N. J. Ghimire and I. I. Mazin, *Nature Materials* **19**, 137-138 (2020).
- [3] N. J. Ghimire et al., *Sci. Adv.*, **6**, 51 (2020) 10.1126/sciadv.abe2680.
- [4] R. L. Dally, J. W. Lynn, N. J. Ghimire, D. Michel, P. Siegfried and I. I. Mazin, *Phys. Rev. B* **103**, 094413 (2021).
- [5] Man Li et al., *Nat. Commun.*, **12**:3129 (2021).
- [6] Qi Wang et al., *Phys. Rev. B* **103**, 014416 (2021).
- [7] C.Q. Xu et al., *Phys. Rev. B* **104**, 024413 (2021).
- [8] Jia-Xin Yin et al., *Nature* **583**, 533 (2020).
- [9] Wenlong Ma et al., *Phys. Rev. Lett.* **126**, 246602 (2021).
- [10] Zhonghao Liu et al., *Phys. Rev. B* **104**, 115122 (2021).
- [11] Wenlong Ma et al., *Phys. Rev. B* **103**, 235109 (2021).
- [12] Dong Chen, Congcong Le, Chenguang Fu, Haicheng Lin, W. Schnelle, Yan Sun and C. Felser, *Phys. Rev. B* **103**, 144410 (2021).
- [13] T. Mazet, H. Ihou-Moko, J. F. Marêché and B. Malaman, *Eur. Phys. J. B* **51**, 173 (2006).
- [14] F. Weitzer, A. Leithejaspser, K. Hiebl, P. Rogl, Q. N. Qi and J. M. D. Coey, *J. Appl. Phys.* **73**, 8447 (1993).

- [15] Y. Amako, T. Yamamoto and H. Nagai, *Hyperfine Interact.* 94, 1897 (1994).
- [16] J. M. Cadogan, Suharyana, D. H. Ryan, O. Moze and W. Kockelmann, *J. Appl. Phys.* 87, 6046 (2000).
- [17] T. Mazet, J. Tobola, G. Venturini and B. Malaman., *Phys. Rev. B* 65, 104406 (2002).
- [18] F. Grandjean, G. J. Long, B. Mahieu, J. Hand and W. J. James, *J. Phys.: Condens. Matter* 17, 4665 (2005).
- [19] P. Gaszyński, L. C. J. Pereira and J. C. Waerenborgh, *J. Alloys Compd.* 451, 484 (2008).
- [20] G. Venturini and B. Malaman, *J. Magn. Magn. Mater.* 377, 159 (2015).
- [21] L.K. Perry, D.H. Ryan and G. Venturini, *Phys. Rev. B* 75, 144417 (2007).
- [22] L.K. Perry, D.H. Ryan and G. Venturini, J. M. Cadogan, *J. Appl. Phys.* 99, 08J302 (2006); 101, 09K504 (2007).
- [23] L. K. Perry, D.H. Ryan and G. Venturini, *Hyperfine Interact.* 170, 105 (2006).
- [24] J. Bourgeois, G. Venturini and B. Malaman, *J. Alloys Compd.* 480, 171 (2009).
- [25] T. Mazet and B. Malaman, *J. Magn. Magn. Mater.* 219, 33 (2000).
- [26] G. Venturini, P. Lemoine and B. Malaman, *J. Magn. Magn. Mater.* 354, 21 (2014).
- [27] J. Rodriguez-Carvajal, *Physica B* 192, 55 (1993).
- [28] G. Le Caër and J.M. Dubois, *J. Phys. E: Sci. Instrum.* 12, 1083 (1979).
- [29] G. Le Caër, B. Malaman, G. Venturini and I.B. Kim, *Phys. Rev. B* 26, 5085(1982).
- [30] L.M. Corliss and J.M. Hastings, *J. Appl. Phys.* 39, 461 (1968).
- [31] G. Venturini, B. Malaman, G. Le Caër and D. Fruchart, *Phys. Rev. B* 35, 7038 (1987).
- [32] G. Le Caër, B. Malaman, G. Venturini, D. Fruchart and B. Roques, *J. Phys. F: Met. Phys.* 15, 1813 (1985).
- [33] G. Le Caër, B. Malaman, G. Venturini, H.G. Wagner and U. Gonser, *Hyperfine Interact.* 28, 631 (1986).
- [34] V. I. Krylov, B. Bosch-Santos, G. A. Cabrera-Pasca, N. N. Delyagin, and A. W. Carbonari, *AIP Advances* 6, 056024 (2016).
- [35] N.N. Delyagin, G.T. Mudzhiri, V.I. Nesterov and A.K. Churakov, *Sov. Phys. JETP* 62, 1240 (1986).
- [36] T. Mazet, J. Tobola and B. Malaman, *Eur. Phys. J. B* 33, 183 (2003).

**Table I:**

$^{119}\text{Sn}$  Mössbauer spectra of  $\text{TmMn}_{6-x}\text{Fe}_x\text{Sn}_6$  stannides were recorded for the experimental combinations (Fe content  $x$ , temperature  $T$ ) given in the left column. Hyperfine magnetic fields of Sn(2d) and Sn(2e) sites, obtained from these spectra, vary linearly with  $p$ , their number of Fe first nearest-neighbors (Fig. 7). Equations of the fitted lines are in the middle column and in the right column for Sn(2d) and Sn(2e) respectively. Errors on all parameters range typically from 0.2 T to 0.4 T (Mn-rich) and from 0.5 T to 1 T (Fe-rich).

$\text{TmMn}_{6-x}\text{Fe}_x\text{Sn}_6$ ( $x$ , T)	Sn(2d) $B_{\text{exp}}^{(2d)}(p)$ (T)	Sn(2e) $B_{\text{exp}}^{(2e)}(p)$ (T)
Mn-rich ( $x=0.4$ , $T=55$ K) ( $x=0.6$ , $T=46$ K) ( $x=1.2$ , $T=30$ K)	$0 \leq p \leq 3$	$0 \leq p \leq 3$
	$31.2-3.4p$	$21.2-2.5p$
Fe-rich ( $x = 4.25$ , $T=4.2$ K) ( $x = 4.50$ , $T=4.2$ K)  Fe-rich ( $x=4.25$ , 51 K) ( $x=4.50$ , 72 K)  Fe-rich ( $x=5$ , 4.2K)	—	$3 \leq p \leq 6$
		$1.5+3.3p$
		$-4+3.3p$
		$3.7p$

### **Figure Legends**

Fig. 1: a) HfFe<sub>6</sub>Ge<sub>6</sub>-type structure of Tm(Mn,Fe)<sub>6</sub>Sn<sub>6</sub>, b) Sn2c, Sn2d, Sn2e tin sites with their first (Mn,Fe) and Tm neighbors.

Fig. 2: Magnetic structures of the studied TmMn<sub>6-x</sub>Fe<sub>x</sub>Sn<sub>6</sub> compounds (further, AFI structures with canted moments are observed in the Fe-rich case, Sn atoms are not shown).

Fig. 3 : Thermal variation of the magnetization of TmMn<sub>6-x</sub>Fe<sub>x</sub>Sn<sub>6</sub> ( $\mu_0 H_{app} = 0.05$  T) a) full temperature range, b) low-temperature range. c) Field dependence of magnetization at 4.2 K.

Fig. 4: Thermal evolutions of the neutron diffraction patterns of Mn-rich TmMn<sub>6-x</sub>Fe<sub>x</sub>Sn<sub>6</sub> compounds ( $x = 0.4, 0.6, 1.2$ ) and of Fe-rich TmMn<sub>6-x</sub>Fe<sub>x</sub>Sn<sub>6</sub> compounds ( $x = 4.25, 4.5, 5.0$ ).

Fig. 5: Temperature dependence of the refined angle  $\theta$  between the moment direction and the c-axis for TmMn<sub>6-x</sub>Fe<sub>x</sub>Sn<sub>6</sub> with  $x = 4.25$  and  $x = 4.50$ .

Fig. 6: Observed and calculated <sup>119</sup>Sn Mössbauer spectra of: 1) ZrMn<sub>6</sub>Sn<sub>6</sub> at 100 K (top) 2) TmMn<sub>6-x</sub>Fe<sub>x</sub>Sn<sub>6</sub> ( $x = 0.4; 0.6; 1.2$ ) with AFII easy-plane structures

Fig. 7: Measured <sup>119</sup>Sn HMF's on the one hand for sites Sn(2d) and Sn(2e) in Mn-rich TmMn<sub>6-x</sub>Fe<sub>x</sub>Sn<sub>6</sub> ( $x = 0.4, 0.6, 1.2$ ) AFII compounds (left and middle figures) and on the other for sites Sn(2e) in Fe-rich ( $x = 4.25, 4.5$ ) AFI compounds (right figure). Experimental HMF's are plotted versus the number  $p$  of Fe neighbors of tin atoms. Line equations are given in Table I.

Fig. 8: Observed and calculated <sup>119</sup>Sn Mössbauer spectra of TmMn<sub>6-x</sub>Fe<sub>x</sub>Sn<sub>6</sub> compounds ( $x = 4.25$  and  $4.5$ ) with AFI antiferromagnetic structures at various temperatures.

Fig.1 : a) HfFe<sub>6</sub>Ge<sub>6</sub>-type structure of Tm(Mn,Fe)<sub>6</sub>Sn<sub>6</sub> , b) Sn<sub>2c</sub>, Sn<sub>2d</sub>, Sn<sub>2e</sub> tin sites with their first (Mn,Fe) and Tm neighbors

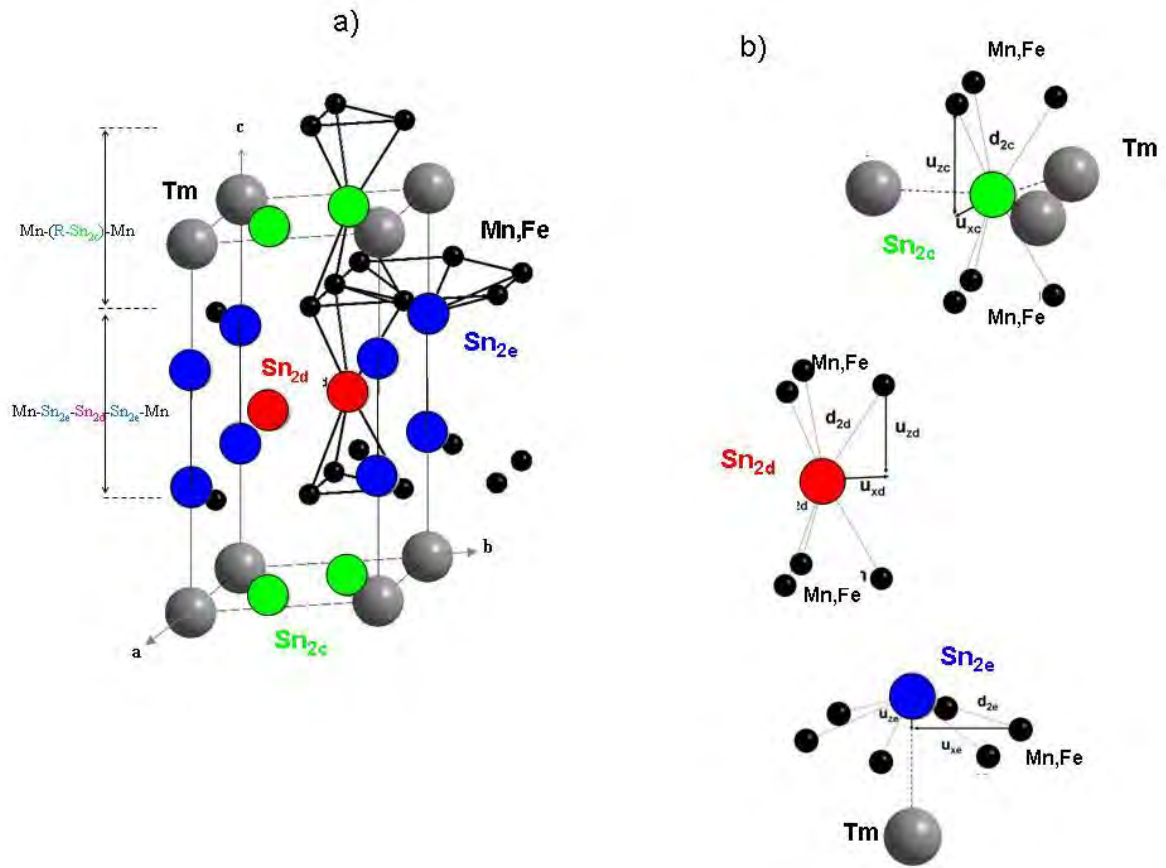


Fig. 2: Magnetic structures of the studied  $TmMn_{6-x}Fe_xSn_6$  compounds (further, AFI structures with canted moments are observed in the Fe-rich case)

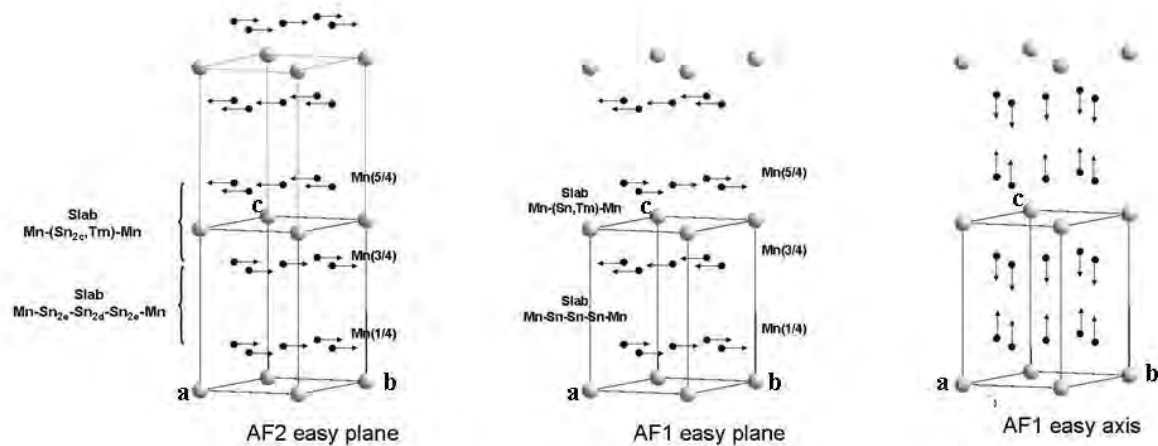


Fig.3 Thermal variation of the magnetization of  $\text{TmMn}_{6-x}\text{Fe}_x\text{Sn}_6$  ( $\mu_0 H_{\text{appl}} = 0.05 \text{ T}$ ) a) full temperature range, b) low-temperature range. c) Field dependence of magnetization at 4.2 K.

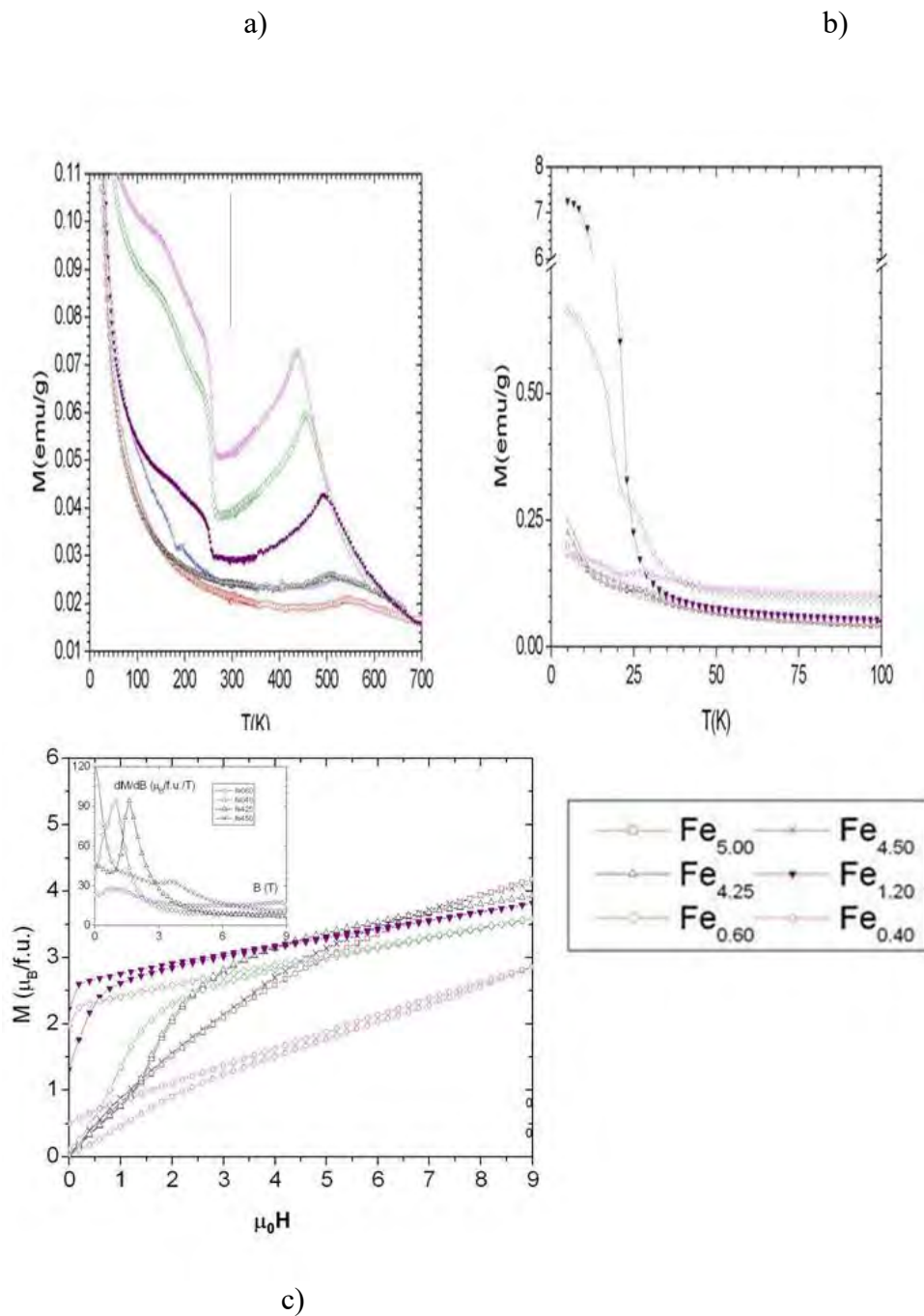


Fig. 4: Thermal evolutions of the neutron diffraction patterns of Mn-rich  $\text{TmMn}_{6-x}\text{Fe}_x\text{Sn}_6$  compounds ( $x = 0.4, 0.6, 1.2$ ) and of Fe-rich  $\text{TmMn}_{6-x}\text{Fe}_x\text{Sn}_6$  compounds ( $x = 4.25, 4.5, 5.0$ )

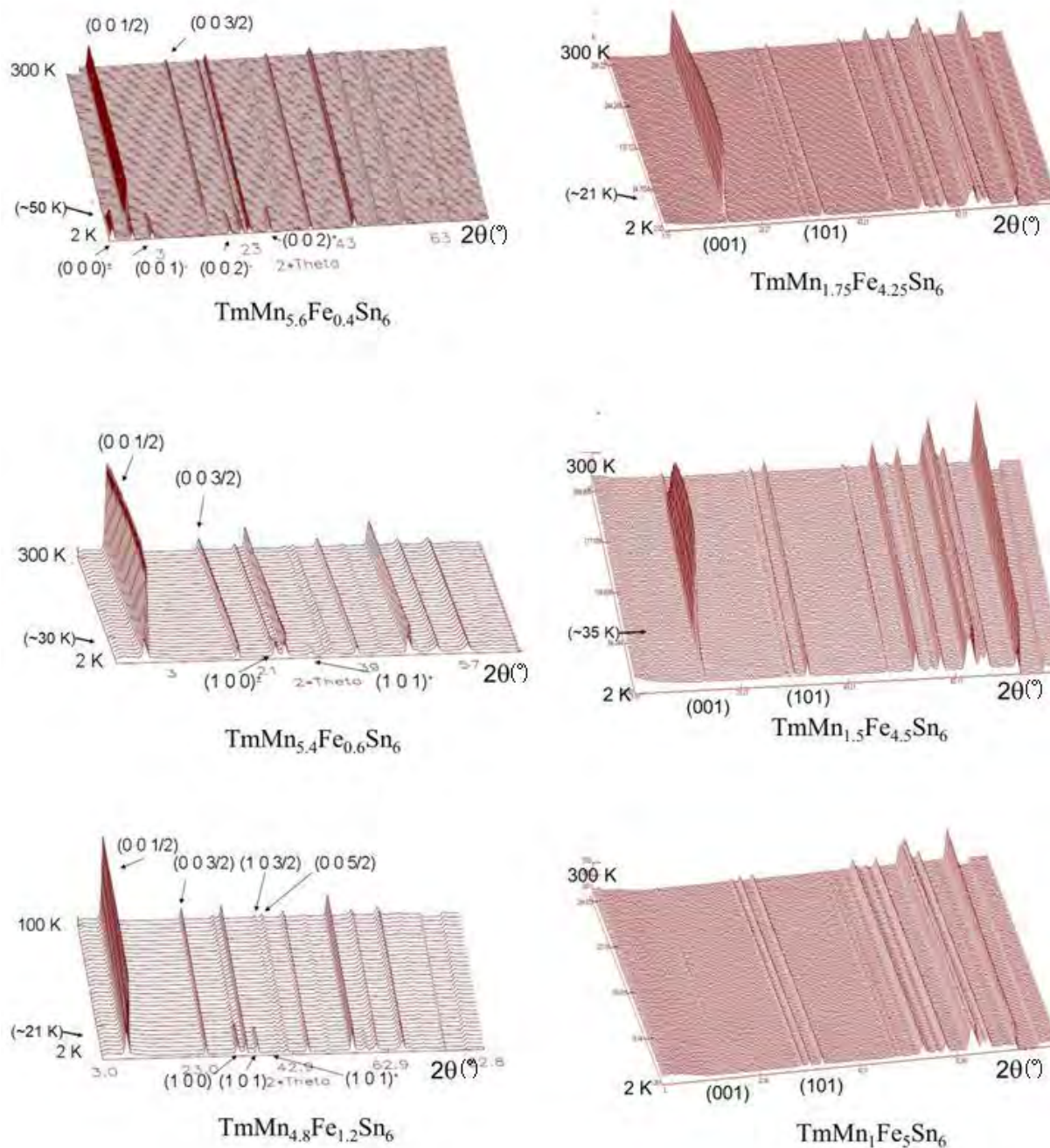


Fig. 5: Temperature dependence of the refined angle  $\theta$  between the moment direction and the c-axis for  $\text{TmMn}_{6-x}\text{Fe}_x\text{Sn}_6$  with  $x = 4.25$  and  $x = 4.50$ .

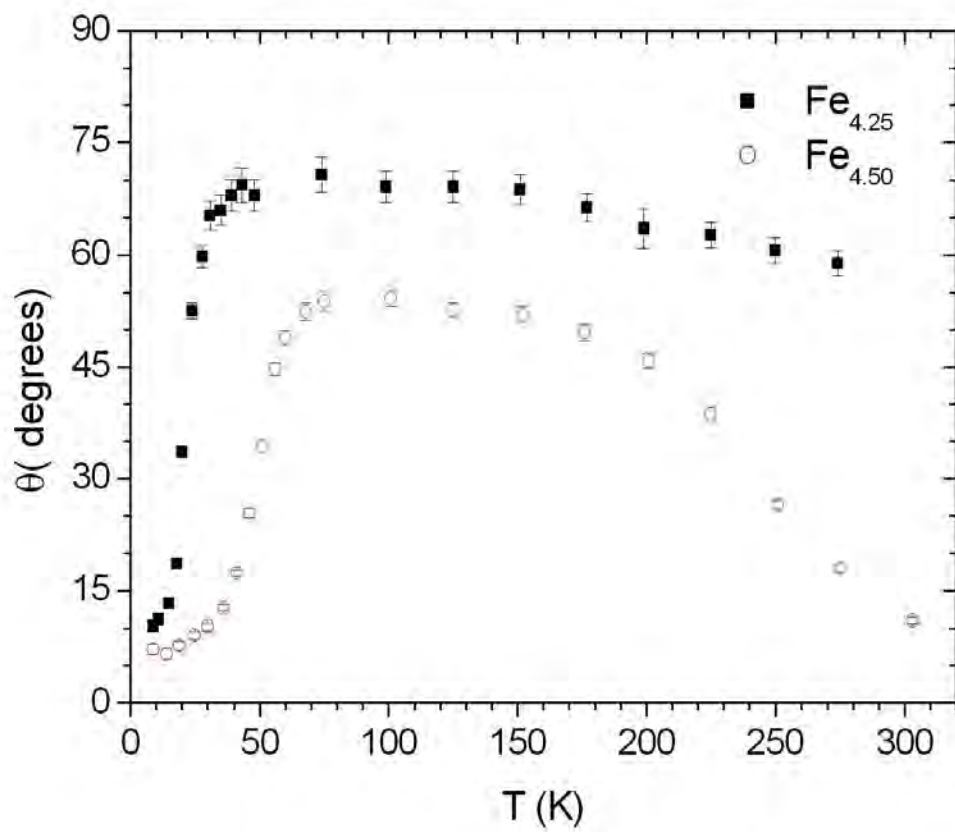


Fig. 6: Observed and calculated  $^{119}\text{Sn}$  Mössbauer spectra of: 1)  $\text{ZrMn}_6\text{Sn}_6$  at 100K (top) 2)  $\text{TmMn}_{6-x}\text{Fe}_x\text{Sn}_6$  ( $x = 0.4; 0.6; 1.2$ ) with AFII easy-plane structures

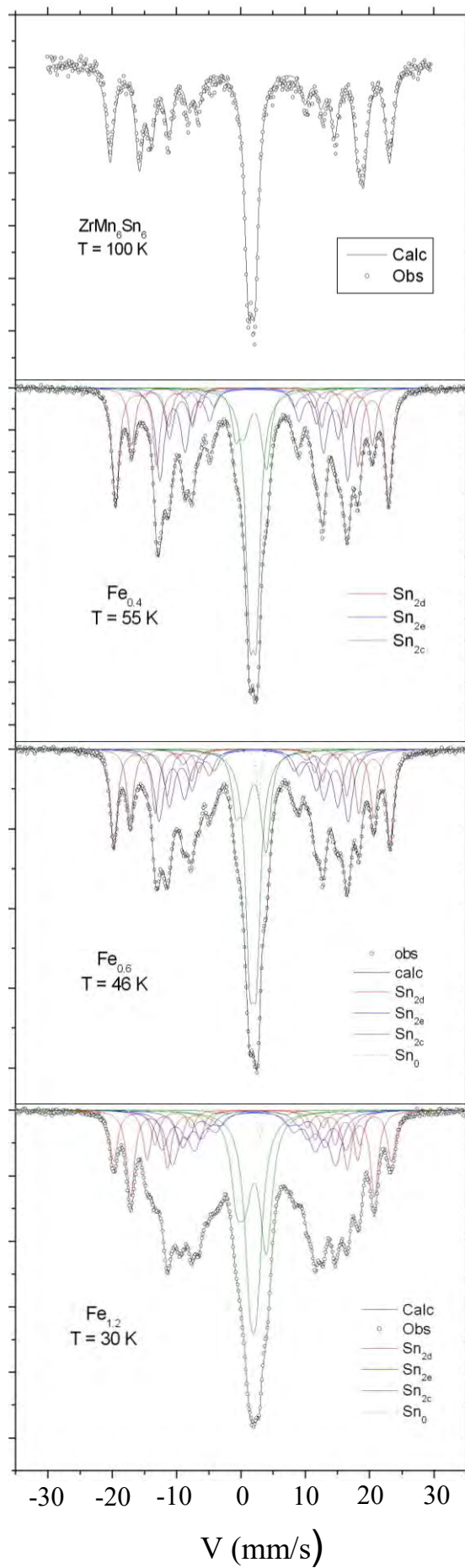


Fig. 7: Measured  $^{119}\text{Sn}$  HMF's on the one hand for sites  $\text{Sn}(2d)$  and  $\text{Sn}(2e)$  in Mn-rich  $\text{TmMn}_{6-x}\text{Fe}_x\text{Sn}_6$  ( $x = 0.4, 0.6, 1.2$ ) AFII compounds (left and middle figures) and on the other for sites  $\text{Sn}(2e)$  in Fe-rich ( $x=4.25, 4.5$ ) AFI compounds (right figure). Experimental HMF's are plotted versus the number  $p$  of Fe neighbors of tin atoms. Line equations are given in Table III.

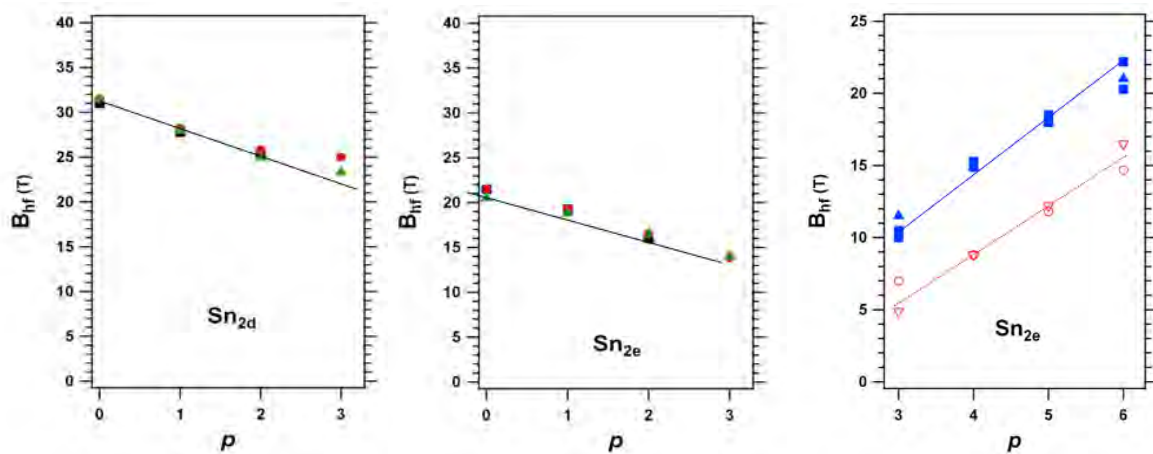
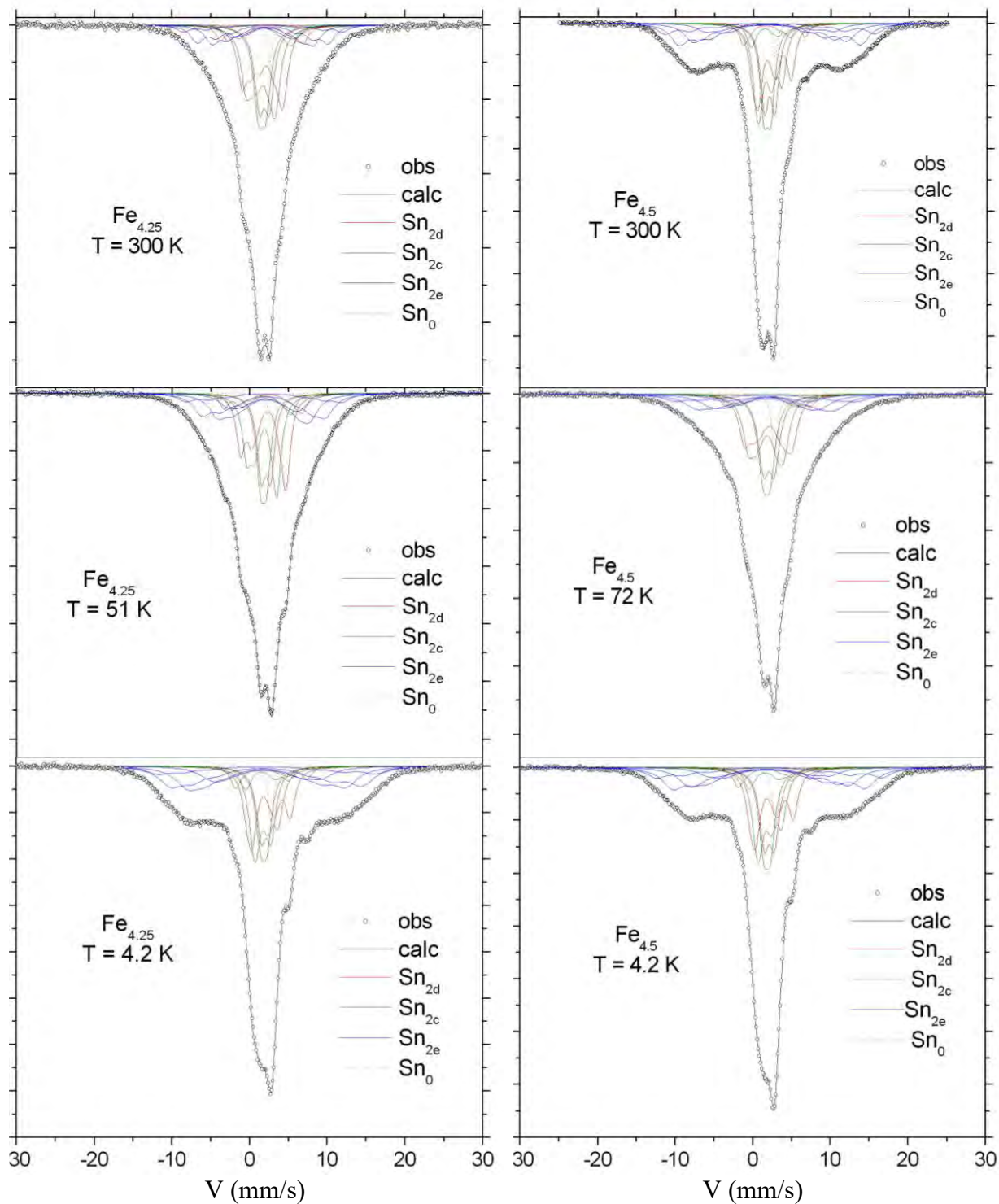


Fig. 8: Observed and calculated  $^{119}\text{Sn}$  Mössbauer spectra of  $\text{TmMn}_{6-x}\text{Fe}_x\text{Sn}_6$  compounds ( $x = 4.25$  and  $4.5$ ) with AFI antiferromagnetic structures at various temperatures.



**Magnetic structures of Mn-rich and of Fe-rich  $\text{TmMn}_{6-x}\text{Fe}_x\text{Sn}_6$  stannides with (Mn, Fe) kagome networks and related  $^{119}\text{Sn}$  hyperfine magnetic fields**

G. Venturini<sup>1†</sup>, B. Malaman<sup>1</sup>, G. Le Caër<sup>2</sup>, T. Mazet<sup>1</sup>

<sup>1</sup> Université de Lorraine, CNRS, IJL, F-54000 Nancy, France

<sup>2</sup> Univ. Rennes, CNRS, IPR (Institut de Physique de Rennes) - UMR 6251, F-35000 Rennes, France

**CONTENTS**

I. Magnetic kagome metals

II. Some crystallographic and magnetic characteristics of  $\text{TmMn}_{6-x}\text{Fe}_x\text{Sn}_6$

- A. Some crystallographic characteristics*
- B. Some magnetic characteristics*

III. Neutron diffraction study

- A. Mn-rich ( $x=0.4, 0.6, 1.2$ )*
- B. Fe-rich ( $x=4.25, 4.5, 5$ )*

IV. Fitting method of  $^{119}\text{Sn}$  Mössbauer spectra of  $\text{TmMn}_{6-x}\text{Fe}_x\text{Sn}_6$

- A. Least-squares fitting*
- B. First-order perturbation theory*

V. Models of  $^{119}\text{Sn}$  transferred hyperfine magnetic fields

- A. Anisotropic  $^{119}\text{Sn}$  hyperfine magnetic fields in  $\text{TmM}_6\text{Sn}_6$  ( $M=\text{Mn}$  or  $\text{Fe}$ )*
- B.  $^{119}\text{Sn}$  hyperfine magnetic fields when the  $M$  moments make an angle  $\theta$  with the  $c$ -axis*
- C. Some literature results for  $\text{RMn}_6\text{Sn}_{6-x}\text{X}_x$  compounds*

VI. Models of transferred hyperfine magnetic fields at Sn sites in pseudo-binary alloys  $\text{TmMn}_{6-x}\text{Fe}_x\text{Sn}_6$

- A.  $^{119}\text{Sn}$  hyperfine magnetic field variations for six equivalent  $M$  first NN sites*
- B.  $^{119}\text{Sn}$  hyperfine magnetic field variations for two groups of three equivalent  $M$  first NN sites*

VII. Hyperfine parameters fitted from  $^{119}\text{Sn}$  Mössbauer spectra of  $\text{TmMn}_{6-x}\text{Fe}_x\text{Sn}_6$

VIII. Sn(2d), Sn(2e) and Sn(2c) hyperfine magnetic fields in Mn-rich  $\text{TmMn}_{6-x}\text{Fe}_x\text{Sn}_6$

- A. Sn(2d) and Sn(2e) sites*
- B. Sn(2c) sites*

IX. Hyperfine magnetic fields in Fe-rich  $\text{TmMn}_{6-x}\text{Fe}_x\text{Sn}_6$  and model parameters

- A. Sn(2c) and Sn(2d) sites*
- B. Sn(2e)*

X.  $^{119}\text{Sn}$  Mössbauer spectra of  $\text{TmMn}_{6-x}\text{Fe}_x\text{Sn}_6$  stannides at 4.2K

- A. Mn-rich ( $x=0.4, 0.6, 1.2$ )*
- B. Fe-rich  $\text{TmMn}_1\text{Fe}_5\text{Sn}_6$  and  $\text{TmFe}_6\text{Sn}_6$  at 4.2K*

References

† deceased

## I. MAGNETIC KAGOME METALS

$\text{RMn}_6\text{Sn}_6$  stannides, with a  $\text{HfFe}_6\text{Ge}_6$ -type structure, belong to the family of transition-metal-based kagome magnets [1]. The most recent studies, with  $\text{R}=\text{Y}$  [2-5], Ga-substituted Y [6], Gd-Tm, [7-9], (Nd-Sm) [10], Li [11-12] with a variety of magnetic ground states, focus on the consequences of the interplay between lattice geometry, electron correlation and band topology which are expected to create new states of quantum matter (see for instance [8]). In the eighties, an antiferromagnetic 2D kagome lattice was considered to be probably the most frustrated magnetic system that one can construct [1] (Fig. S1).

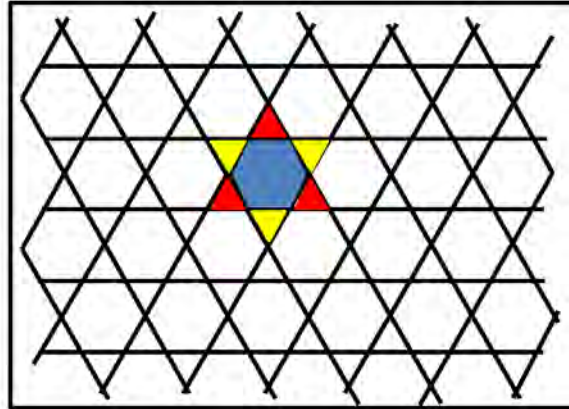


FIGURE S1: A 2D kagome network composed of equilateral triangles and of regular hexagons.

Kagome planes formed by Fe or Mn atoms often have strong in-plane ferromagnetic exchange interactions, which are not magnetically frustrated, but still have features typical of kagome lattices because of much weaker, often frustrated, interplanar exchange interactions [2]. According to Dally et al. [3], the latter interactions result for instance in a complex magnetic phase diagram of commensurate and incommensurate phases when applying a magnetic field in the  $ab$  plane of  $\text{YMn}_6\text{Sn}_6$ . One of the phase coexists with the topological Hall effect [8]. Mazet et al. [12] first synthesized the stannide  $\text{LiMn}_6\text{Sn}_6$ . They studied it by magnetic measurements, neutron diffraction and  $^{119}\text{Sn}$  Mössbauer spectroscopy. Interestingly,  $\text{LiMn}_6\text{Sn}_6$  was shown to be an easy-plane kagome ferromagnet with a Curie temperature of 380K. Very recently, a large anomalous Hall effect was measured by Chen et al. [11] in  $\text{LiMn}_6\text{Sn}_6$ . The latter effect has been attributed to band crossings near the Fermi energy.

## II. CRYSTALLOGRAPHIC AND MAGNETIC FEATURES OF $\text{TmMn}_{6-x}\text{Fe}_x\text{Sn}_6$

### A. Some crystallographic characteristics

Atomic positions and reduced atomic coordinates in  $\text{RM}_6\text{X}_6$  compounds with a hexagonal  $\text{HfFe}_6\text{Ge}_6$ -type structure (space group  $P6/mmm$  no 191) are given in table S1. The point symmetry is  $\bar{6}m2$  at both crystallographic sites 2c, 2d and  $6mm$  at site 2e.

**TABLE S1:**

Atomic positions and reduced atomic coordinates in  $\text{RM}_6\text{X}_6$  compounds

Site	Atom	$\text{RM}_6\text{X}_6$	
6i	M	$(1/2 \ 0 \ z_M)$	$(0 \ 1/2 \ z_M) \ (1/2 \ 1/2 \ z_M)$
		$(1/2 \ 0 \ \bar{z}_M)$	$(0 \ 1/2 \ \bar{z}_M) \ (1/2 \ 1/2 \ \bar{z}_M)$
$z_M \approx 0.25$			
2d	X	$(1/3 \ 2/3 \ 0)$	
		$(2/3 \ 1/3 \ 0)$	
2c	X	$(1/3 \ 2/3 \ 1/2)$	
		$(2/3 \ 1/3 \ 1/2)$	
2e	X	$(0 \ 0 \ z_e)$	$z_e \approx 0.33$
		$(0 \ 0 \ \bar{z}_e)$	
1a	R	$(0 \ 0 \ 0)$	

M (=Mn, Fe) atoms occupy the  $(\frac{1}{2}, 0, \pm z_M)$ ,  $(\frac{1}{2}, \frac{1}{2}, \pm z_M)$  and  $(0, \frac{1}{2}, \pm z_M)$  (6i) positions in  $\text{TmMn}_{6-x}\text{Fe}_x\text{Sn}_6$ , where the free general  $z_M$  coordinate deviates little from  $1/4$  (Table S2). Tm atoms occupy a (1a) site. For convenience, tin atoms are named according to the sites they occupy (2c, 2d, 2e) (Table S1). Hereafter, they will be denominated indifferently as Sn(2h) “atoms” or “sites” where  $h=c, d, e$ . In  $\text{RM}_6\text{Sn}_6$ , all tin sites have six M transition metal atoms as first nearest neighbors either contained in two successive kagome planes for a given Sn(2h) atom ( $h=c, d$ ) or in a single kagome plane for Sn(2e). For convenience, we denote as  $\text{K}^+$  the kagome plane first met when going from a given Sn(2h) atom in the  $[001]$  direction and as  $\text{K}^-$  the one first met in the opposite direction.

Table S2 gives the cell parameters  $a, c$ , the cell volume  $V$ , the ratio  $c/a$  and the reduced atomic coordinates of M,  $z_M$ , and of Sn,  $z_{\text{Sn}}$ , in  $\text{TmMn}_{6-x}\text{Fe}_x\text{Sn}_6$  as obtained from X-ray diffraction patterns at room temperature (RT, nominally 295 K). The cell volume decrease monotonously with  $x$  while the  $c/a$  ratio increases, with a significantly larger average slope in the Mn-rich range than in the Fe-rich range. The Fe-rich  $\text{Tm}_{1-\delta}\text{Mn}_{6-x}\text{Fe}_x\text{Sn}_6$  stannides are

slightly under-stoichiometric in Tm. The values of  $1-\delta$  are given in the last column of Table S2. Results for  $x = 6$  are taken from [13].

**TABLE S2:**

Crystallographic characteristics of  $\text{Tm}_{1-\delta}\text{Mn}_{6-x}\text{Fe}_x\text{Sn}_6$  as defined above

x	a(Å)	c(Å)	V(Å <sup>3</sup> )	c/a	Z <sub>M</sub>	Z <sub>Sn</sub>	1-δ
0.4	5.5020(1)	8.9875(1)	235.62(1)	1.6335	0.2480(4)	0.3365(3)	1.00(2)
0.6	5.4959(1)	8.9822(2)	234.96(1)	1.6343	0.2514(5)	0.3323(4)	1.00(2)
1.2	5.4788(1)	8.9745(2)	233.29(1)	1.6380	0.2472(4)	0.3376(3)	1.00(2)
4.25	5.4160(1)	8.9328(2)	226.92(1)	1.6493	0.2520(4)	0.3350(3)	0.93(2)
4.5	5.4117(1)	8.9266(2)	226.40(1)	1.6495	0.2463(4)	0.3387(4)	0.95(2)
5.0	5.4038(1)	8.9151(2)	225.45(1)	1.6498	0.2495(5)	0.3329(4)	0.93(2)
6	5.383(1)	8.884(2)	222.9(1)	1.650	-	-	≈ 0.9

### ***B. Some magnetic characteristics***

Table S3 summarizes some magnetic characteristics of  $\text{TmMn}_{6-x}\text{Fe}_x\text{Sn}_6$  stannides, where  $T_N$  is the Néel temperature and  $T_c$  is the temperature of appearance of a significant ferromagnetic component in the stannide with  $x = 1.20$ .  $T_{t1}$  and  $T_{t2}$  correspond to the other low-temperatures anomalies of the thermomagnetization curves.  $M_{9T}$  and  $M_r$  are, respectively, the maximal magnetization measured in an applied field of 9 T and the remnant magnetization (given in Bohr magneton per formula unit).  $\mu_0 H_{\text{crit}}$  is the critical field associated with the upturn in the isothermal magnetization curves.

The Néel temperatures of  $\text{TmMn}_{6-x}\text{Fe}_x\text{Sn}_6$  stannides increase with  $x$  in the Mn-rich and in the Fe-rich ranges respectively. This does not preclude a non-monotonic variation in the intermediate concentration range as observed in the related stannide  $\text{ErMn}_{6-x}\text{Fe}_x\text{Sn}_6$  which shows a maximum at  $x \sim 2$  and a minimum at  $x \sim 3$  [14] (Fig. S2)

**TABLE S3:**

x	$T_N$ (K)	$T_c$ (K)	$T_{t1}$ (K)	$T_{t2}$ (K)	$M_{9T}$ ( $\mu_B/\text{fu}$ )	$M_r$ ( $\mu_B/\text{fu}$ )	$\mu_0 H_{\text{crit}}$ (T)
0.40	438	-	26.8	-	2.9	0.5	0.84
0.60	455	-	28.8	18.8	3.6	2.0	0.94
1.20	493	16.7	-	-	3.8	2.2	-
4.25	503	-	24.9	8.1	3.9	0	1.60
4.50	513	-	8.4	-	4.6	0	3.60
5.00	543	-	-	-	4.2	0	-

Figure S2 displays the  $x$ -dependence of the latter Néel temperature together with those of  $\text{ErMn}_{6-x}\text{Fe}_x\text{Sn}_6$ .

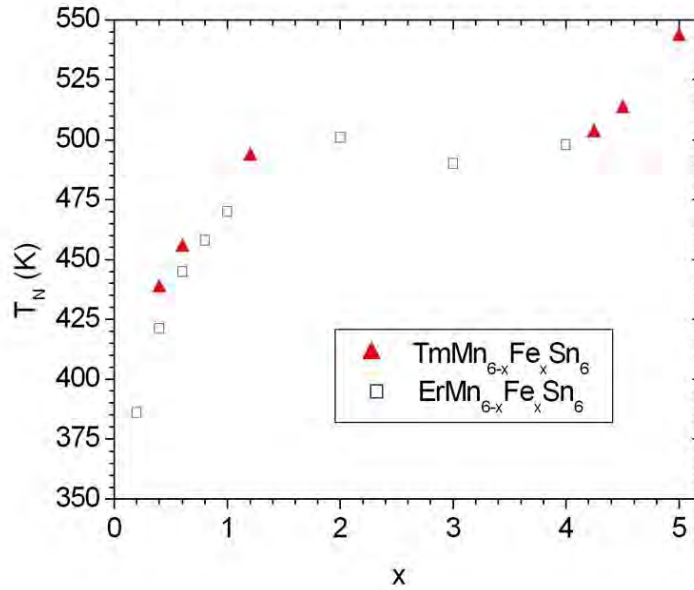


FIGURE S2: Néel temperatures of  $\text{TmMn}_{6-x}\text{Fe}_x\text{Sn}_6$  and of  $\text{ErMn}_{6-x}\text{Fe}_x\text{Sn}_6$  [14] as a function of  $x$ .

### III. NEUTRON DIFFRACTION STUDY

Two antiferromagnetic structures, AFI and AFII favored in the present study, are characterized by an ordering of the sole transition metal moments  $M$  which are ferromagnetically coupled in the  $(0\ 0\ 1)$  kagome planes [15]. Successive ferromagnetic  $(0\ 0\ 1)$  kagome planes are coupled along the  $c$ -axis according to sequences,  $++--$  and  $-++$  for AFII (Mn-rich) and AFI (Fe-rich) respectively [15] (Fig. 2 of the article). Structural and magnetic parameters were refined using the Fullprof software [16].

#### A. Mn-rich ( $x=0.4, 0.6, 1.2$ )

Neutron diffraction patterns of Mn-rich stannides, recorded at temperatures  $\sim 90$  K, evidence the AFII magnetic structure of the  $M$  moments (Fig. S3). Table S4 gives the parameters calculated from these patterns. Low-temperature neutron diffraction patterns, related to the magnetic ordering of the Tm sublattice, result from a mixture of several magnetic phases. Their analysis, which is beyond the scope of the present study, will not be discussed.

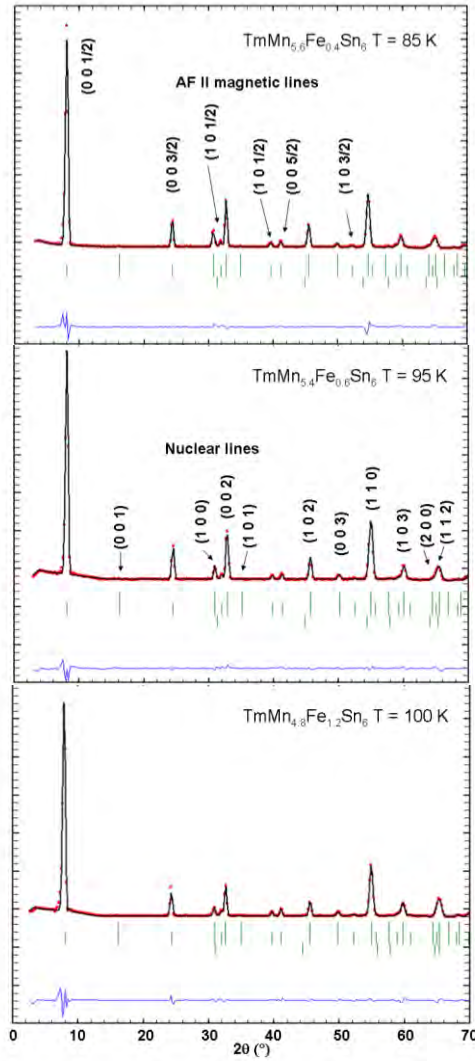


FIGURE S3: Observed and calculated neutron diffraction patterns of  $\text{TmMn}_{5.6}\text{Fe}_{0.4}\text{Sn}_6$ ,  $\text{TmMn}_{5.4}\text{Fe}_{0.6}\text{Sn}_6$  and  $\text{TmMn}_{4.8}\text{Fe}_{1.2}\text{Sn}_6$  (from top to bottom) at the indicated temperatures. AFII magnetic lines ( $x=0.4$ ) and nuclear lines ( $x=0.6$ ) are separately identified. First tick row: nuclear  $\text{HfFe}_6\text{Ge}_6$ -type; second row: AFII magnetic structure; third row:  $\text{CuAl}_2$ -type  $(\text{Mn,Fe})\text{Sn}_2$

### B. Fe-rich ( $x=4.25, 4.5, 5$ )

Some neutron diffraction patterns of Fe-rich stannides are shown in Fig. S4. All patterns are characterized by a significant intensity of the  $(1\ 0\ 1)$  line which is characteristic of the AFI antiferromagnetic structure usually adopted by the Fe moments in  $\text{RFe}_6\text{Sn}_6$  (Fig. S4). The missing  $(0\ 0\ 1)$  peak in  $\text{TmMn}_{1.0}\text{Fe}_{5.0}\text{Sn}_6$  indicates that the magnetic moment is aligned along the  $c$ -axis. By contrast, the patterns of the two other Fe-rich stannides ( $x = 4.25$  and  $4.50$ ) show that the  $(0\ 0\ 1)$  intensities vary strongly with temperature. This means that the moment direction deviates markedly from the  $c$ -axis. Refinements were carried out letting the

angle  $\theta$  between the moment direction and the c-axis free to vary (see also Fig. 5 of the paper). The refined parameters and R-factors are given in Table S5.

**TABLE S4:**

Refined cell parameters, atomic coordinates ( $z_{\text{Sn}}$  and  $z_{\text{M}}$ ), occupation factors ( $\text{occ}_{\text{Fe}}$  and  $\text{occ}_{\text{Mn}}$ ) and magnetic moment of Mn-rich  $\text{TmMn}_{6-x}\text{Fe}_x\text{Sn}_6$  ( $x = 0.4, 0.6$  and  $1.2$ ) from neutron diffraction patterns recorded at the indicated temperatures.

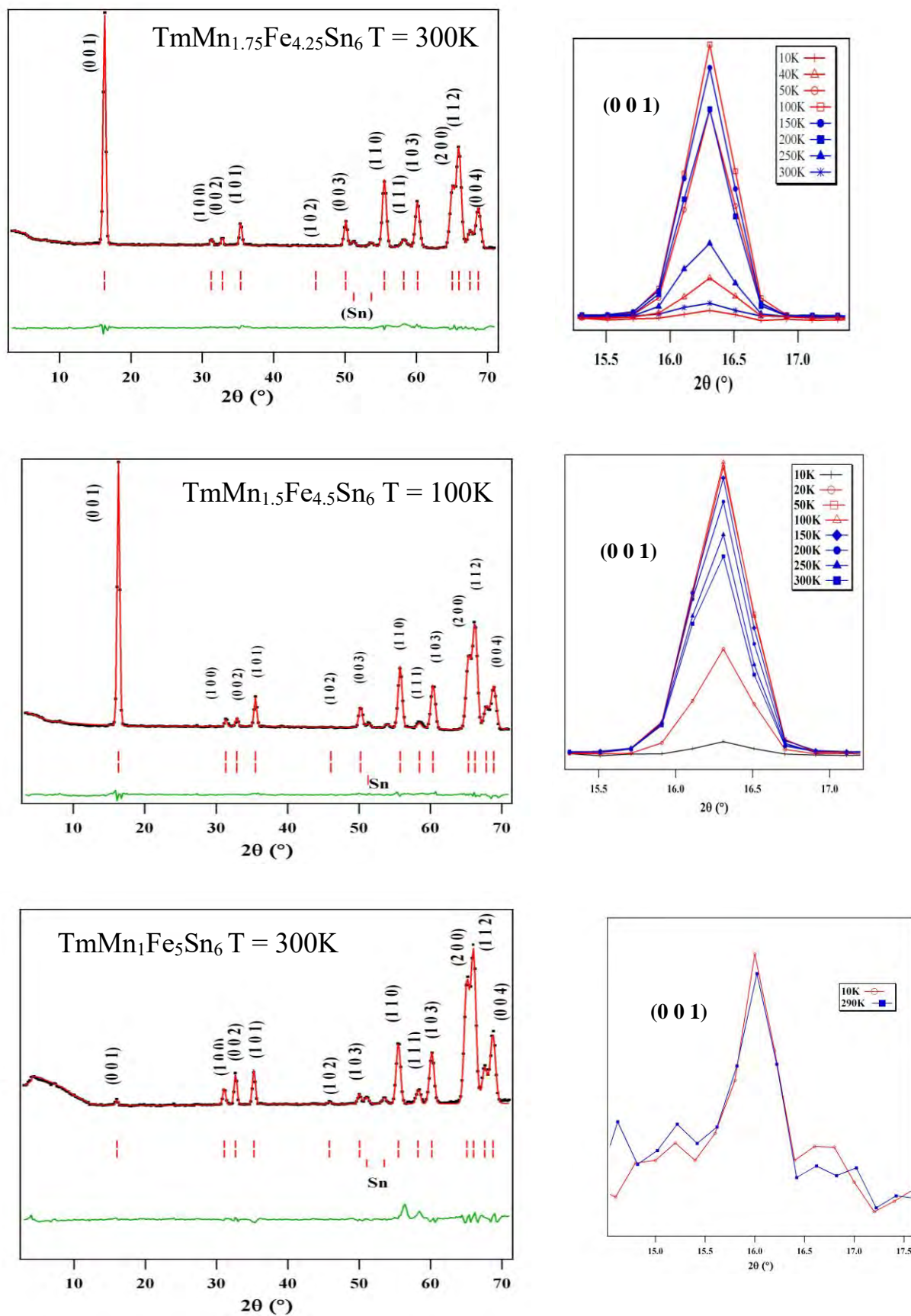
x	0.4	0.4	0.6	0.6	1.2
T(K)	301	85	296	95	100
a(Å)	5.502(1)	5.490(5)	5.495(1)	5.462(1)	5.463(1)
c(Å)	8.986(1)	8.958(7)	8.985(1)	8.922(1)	8.971(1)
$z_{\text{Sn}}$	0.331(1)	0.330(2)	0.334(1)	0.334(3)	0.336(2)
$z_{\text{M}}$	0.246(1)	0.247(1)	0.246(1)	0.242(2)	0.247(2)
$\text{occ}_{\text{Fe}}$	0.013(1)	0.012(2)	0.023(1)	0.025(2)	0.049(2)
$\text{occ}_{\text{Mn}}$	0.237(1)	0.238(2)	0.227(1)	0.225(2)	0.201(2)
$\mu_{\text{M}}$ ( $\mu_{\text{B}}$ )	1.95(9)	2.33(15)	1.9(1)	2.13(18)	2.14(9)

**TABLE S5:**

Refined atomic and magnetic parameters for Fe-rich  $\text{TmMn}_{6-x}\text{Fe}_x\text{Sn}_6$  stannides ( $x = 4.25, 4.5, 5.0$ ) obtained at different temperatures from neutron diffraction patterns.  $\theta$  is the angle between the c-axis and the M moment direction.

x	4.25	4.25	4.5	4.5	4.5	5.0	5.0
T(K)	281	2	300	152	2	300	2
a(Å)	5.415(1)	5.399(1)	5.411(1)	5.396(1)	5.393(1)	5.402(1)	5.386(1)
c(Å)	8.937(1)	8.921(1)	8.929(2)	8.915(1)	8.912(2)	8.917(2)	8.900(2)
$z_{\text{Sn}}$	0.249(1)	0.247(1)	0.246(1)	0.246(1)	0.246(1)	0.245(1)	0.247(1)
$z_{\text{M}}$	0.326(2)	0.332(1)	0.333(2)	0.332(2)	0.335(1)	0.333(1)	0.334(2)
$\text{occ}_{\text{Fe}}$	0.174(1)	0.178(1)	0.187(1)	0.186(1)	0.187(1)	0.211(1)	0.209(1)
$\text{occ}_{\text{Mn}}$	0.076(1)	0.072(1)	0.063(1)	0.064(1)	0.063(1)	0.039(1)	0.041(1)
$\mu_{\text{M}}$ ( $\mu_{\text{B}}$ )	2.07(3)	2.35(3)	2.12(3)	2.27(3)	2.40(3)	2.17(2)	2.42(3)
$\theta$ (°)	59(1)	7.6(6)	11.1(4)	52(1)	7.5(5)	4.5(8)	3.1(7)

FIGURE S4: Left: Observed and calculated neutron diffraction patterns of  $\text{TmMn}_{6-x}\text{Fe}_x\text{Sn}_6$  stannides ( $x = 4.25, 4.5, 5.0$ ) at the indicated temperatures (about 2% Sn); first tick row: nuclear  $\text{HfFe}_6\text{Ge}_6$ -type; second row: AFI magnetic structure. Right: temperature dependence of the (001) peak.



#### IV. FITTING METHOD OF $^{119}\text{Sn}$ MÖSSBAUER SPECTRA OF $\text{TmMn}_{6-x}\text{Fe}_x\text{Sn}_6$

The simple antiferromagnetic structures, AFI and AFII, are favoured in the present study of  $^{119}\text{Sn}$  hyperfine magnetic fields. Indeed, it is very difficult to unscramble with confidence the effects on  $^{119}\text{Sn}$  Mössbauer spectra of complex magnetic structures from those of the disordered substitution of Mn with Fe.

##### *A. Least-squares fitting*

$^{119}\text{Sn}$  Mössbauer spectra of  $\text{TmMn}_{6-x}\text{Fe}_x\text{Sn}_6$  were fitted with a standard least-squares method program assuming Lorentzian peaks. The latter proceeds by successive iterations from guessed initial values. By contrast, strong overlaps of  $^{119}\text{Sn}$  Mössbauer subspectra of Fe-rich stannides, more particularly those of central components, require to fix the values of the relative areas of related subspectra during the whole fitting process to obtain reliable hyperfine parameters.

Additional approximations were introduced in spectra fittings. Full-widths at half-maximum (FWHM or  $\Gamma$ ) of Lorentz lines, isomer shifts and quadrupole splittings or quadrupole shifts were constrained to be the same for the various spectral components associated with a given Sn(2h) site ( $h=c, d, e$ ) (see next section). The latter tin components differ by the number of Mn and Fe nearest neighbors of the considered Sn(2h) site, a fact classically observed in Mössbauer spectra of binary solid solutions. Further, we assumed that  $^{119}\text{Sn}$  Lamb-Mössbauer factors are similar for the three equally occupied tin sites. In the thin absorber approximation, the relative spectral areas of the aforementioned components are thus essentially equal to their associated relative tin fractions. The latter are calculated from the occupation of sites (6i) by Mn and Fe atoms, assumed below to be random. This assumption yields the probability  $P(p)$  (the binomial distribution given by Eq. (2) of the article) that a Sn(2h) atom, named hereafter  $\text{Sn}_{2h}(p)$ , has  $p$  Fe atoms and  $6-p$  Mn atoms as nearest neighbors. From the point of view of hyperfine magnetic fields, the studied stannides with AFI and AFII structures might be considered as “pseudo-binary alloys” of Mn and Fe in parallel kagome planes where tin atoms play a role of local probes.

Table S6 gives the most significant values of  $P(p)$  for the different pseudo-binary alloys we studied i.e. those of configurations whose associated Mössbauer subspectra might be observed. The relative fraction of any given  $\text{Sn}_{2h}(p)$  species with respect to all Sn(2h) atoms is given in Table S6 ( $p=0, \dots, 5$ ) ( $P(6)=1$  for  $x=6$ ). It must be divided by 3 to obtain

instead the fraction or the relative spectral area of  $\text{Sn}_{2\text{h}}(p)$  atoms with respect to all Sn atoms which belong to three families of equal weights.

**Table S6:**

Probability  $P(p)$  that a  $\text{Sn}_{2\text{h}}$  atom has  $p$  Fe and  $6-p$  Mn nearest neighbors in  $\text{TmMn}_{6-x}\text{Fe}_x\text{Sn}_6$

x	$P(0)$	$P(1)$	$P(2)$	$P(3)$	$P(4)$	$P(5)$	$P(6)$
0.4	0.661	0.283	0.051	-	-	-	-
0.6	0.531	0.354	0.098	-	-	-	-
1.2	0.262	0.393	0.246	0.082	-	-	-
4.25	-	-	0.054	0.176	0.321	0.312	0.126
4.5	-	-	-	0.132	0.267	0.356	0.178
5	-	-	-	0.054	0.201	0.402	0.335

The number of configurations of  $p$  Fe neighbors of  $\text{Sn}(2\text{c})$  or of  $\text{Sn}(2\text{d})$  atoms, contained in a single kagome plane,  $A^{(1)}(p)$ , or in two kagome planes,  $A^{(2)}(p)$ , are further given in Table S7 below. The various repartitions of  $p$  Fe first nearest neighbors of  $\text{Sn}_{2\text{c}}$  or of  $\text{Sn}_{2\text{d}}$  atoms in the two kagome planes  $\text{K}^-$  and  $\text{K}^+$  (Suppl. Fig. S5) are given by pairs  $(p_1, p_2)$  where  $p_1$  Fe atoms are in  $\text{K}^-$  and  $p_2$  in  $\text{K}^+$ .  $(A^{(1)}(p) + A^{(2)}(p)) = \binom{6}{p}$ .

### **B. First-order perturbation theory**

A criterion to evaluate the validity, at a temperature  $T$ , of first order perturbation theory of hyperfine magnetic interactions at a given Mössbauer site is the ratio  $R_{FO}(T) = \left| QS(T) / (g_{3/2} B(T)) \right|$ . The latter ratio is calculated from  $QS(T)$ , the quadrupole splitting (in mm/s) which would be measured at  $T$  in a non-magnetic state,  $g_{3/2}$  the nuclear g factor for the excited state ( $\approx 0.27611$  mm/(s.T) for  $^{119}\text{Sn}$ ) and  $B(T)$  the hyperfine magnetic field (T). If  $R_{FO}(T)$  is much less than 1, the quadrupole interaction can be treated as a first-order perturbation upon the hyperfine magnetic interaction. The quadrupole splittings of the stannides we study do not vary significantly in the temperature ranges we investigate. If first-order perturbation theory holds at temperature  $T$ , then the positions of the six Mössbauer lines ( $^{119}\text{Sn}$ ,  $^{57}\text{Fe}$ ), numbered from 1 to 6 from negative to positive velocities, are given by  $v_j(T) = \alpha_j B(T) + \beta_j \varepsilon(T) + \delta(T)$  ( $j = 1, \dots, 6$ ). The  $\alpha_j$ , which are such that  $\alpha_6 = -\alpha_1 > 0$ ,  $\alpha_3 = -\alpha_2 > 0$ ,  $\alpha_4 = -\alpha_5 > 0$ , are characteristic of the considered isotope and

$\beta_1 = \beta_6 = 1$ ,  $\beta_j = -1$ ,  $j = 2, \dots, 5$  (see for instance [17]). In this case, the quadrupole shift  $2\varepsilon(T)$  is calculated from  $2\varepsilon(T) = \left[ (v_1(T) + v_6(T)) - (v_2(T) + v_5(T)) \right] / 2$ , and  $\delta(T)$  is the isomer shift referred here to  $\text{BaSnO}_3$  at RT in the case of the  $^{119}\text{Sn}$  isotope. In passing, the maximum hyperfine magnetic field can then be correctly estimated just by measuring the velocity interval between the most external peaks on both sides of a spectrum:  $B_{\max}(T) = (v_{6,\text{ext}}(T) - v_{1,\text{ext}}(T)) / (2\alpha_6)$ .

**Table S7:**

The  $A^{(k)}(p)$  counts the configurations of  $p = p_1 + p_2$  Fe contained either in a single kagome plane ( $k=1$ ) or in two kagome planes ( $k=2$ ). The number  $N_{Fe} = |p_1 - p_2|$  plays the role of an effective number of neighbors (Eq. (9) of the article) .

$p$	<i>Fe in <math>K^-</math> or in <math>K^+(k=1)</math> (<math>p, 0</math>), (<math>0, p</math>)</i>	$A^{(1)}(p)$	<i>Fe in <math>K^-</math> and in <math>K^+(k=2)</math> (<math>p_1, p_2</math>), (<math>p_2, p_1</math>)</i>	$A^{(2)}(p)$	$N_{Fe} =$ $ p_1 - p_2 $
0	(0,0)	1	-	0	0
1	(0,1), (1,0)	6	-	0	1
2	(0,2), (2,0)	6	-	0	2
2	-	0	(1,1)	9	0
3	(0,3), (3,0)	2	-	0	3
3	-	0	(1,2), (2,1)	18	1
4	-	0	(1,3), (3,1)	6	2
4	-	0	(2,2)	9	0
5	-	0	(2,3), (3,2)	6	1
6	-	0	(3,3)	1	0

In its principal axis system of reference (OXYZ), the principal components of a zero-trace electric field gradient (EFG) tensor,  $V_{xx}$ ,  $V_{yy}$ ,  $V_{zz}$ , are defined to be such that  $|V_{xx}| \leq |V_{yy}| \leq |V_{zz}|$ . The principal components are thus fully defined by  $V_{zz}$  and an asymmetry parameter,  $\eta$  with  $0 \leq \eta = (V_{xx} - V_{yy}) / V_{zz} \leq 1$ . Within the framework of the previous theory,

the quadrupole shift is given by  $2\varepsilon(T) = QS(T)(3\cos^2\alpha - 1 + \eta\sin^2\alpha\cos(2\beta))/2$ , if  $\eta \neq 0$ , where  $\alpha$  and  $\beta$  are the polar coordinates of the hyperfine magnetic field with respect to the principal axes of the EFG tensor. The aforementioned line positions, and the hyperfine parameters deduced from them, are exact, for any value of  $R_{FO}(T)$ , when the direction of the hyperfine magnetic field at  $T$  is along the principal axis OZ and when  $\eta = 0$ .

In  $\text{TmMSn}_6$  (M=Mn or Fe), local symmetries imply that the OZ principal axes of the EFG tensors at the three tin sites (h=c, d, e) are parallel to the c-axis and that  $\eta(2h) = 0$  (Sec. I of the article). The quadrupole splittings in our experiments are  $QS(2h) \propto |V_{zz}(2h)|$ . They would be measured at the considered temperature if transferred hyperfine magnetic fields were equal to zero. The above expression of  $2\varepsilon$  for a tin site h becomes  $2\varepsilon(2h) = QS(2h)(3\cos^2\alpha - 1)/2$ , in the magnetic state, where  $\alpha$  is the angle between the hyperfine magnetic field direction and the c-axis. The latter direction does not coincide with the moment direction  $\theta$  because of anisotropic interactions except for easy-plane or easy-axis magnetic structures.

### 1. Fe-rich stannides

First-order perturbation theory is exact at any temperature ( $\theta = \alpha \approx 0^\circ$ ) for Sn(2e) sites in  $\text{TmFe}_6\text{Sn}_6$  and at very low temperature for tin sites, with six Fe first nearest neighbors, in Fe-rich  $\text{TmMn}_{6-x}\text{Fe}_x\text{Sn}_6$ . In the latter stannides,  $x=4.25, 4.5, 5, 6$ , Sn(2e) atoms have large mean hyperfine fields and small mean quadrupole shifts ( $\sim 0.2\text{-}0.6$  mm/s) (Table S9 and S11).

Atoms, denoted hereafter as  $\text{Sn}_{2h}(p)$ , are Sn(2h) atoms which have a fixed number  $p$  of Fe first nearest neighbors for the given Fe content  $x$  ( $0 \leq p \leq 6$ ), omitted in their notation. We focus on Sn(2e) atoms for any  $x$  and on Sn(2d) atoms in Mn-rich stannides. All other tin sites, with small magnetic hyperfine fields, are sandwiched between antiferromagnetically coupled kagome planes. The mean hyperfine magnetic fields of the considered  $\text{Sn}_{2h}(p)$  atoms, calculated from the model, are linear interpolations between the fields of  $\text{Sn}_{2h}(0)$  and those of  $\text{Sn}_{2h}(6)$  atoms (Eq. (26)). The latter are easily characterized in Mössbauer spectra. First-order perturbation theory should apply satisfactorily to their spectral components associated with symmetric first-neighbor shells of Fe atoms.

Isotropic hyperfine magnetic fields and isomer shifts of  $\text{Sn}_{2e}(p)$  ( $1 \leq p \leq 6$ ) atoms have been reasonably assumed to be independent on the position of Fe atoms and of Mn atoms. However, sources of line broadening are related to the variety of environments of  $\text{Sn}_{2h}(p)$  atoms where  $2 \leq p \leq 5$ . This variety is due primarily to the different ways to place  $p$  Fe atoms

on the six first nearest neighbour sites. Averages must be taken over all possible configurations for a given number of Fe neighbors. In the cases where  $p=1$  or  $5$ , the quadrupole splittings, which are the moduli of the EFG tensors, are the same for any of the six positions of the Fe or the Mn neighbor because of the sixfold symmetry. However, the quadrupole shift at a given position might depend on  $\alpha$  (and  $\beta$ ) so that the average over the six positions will produce broadened lines possibly asymmetric. This is exemplified by a calculation, performed with the assumption of the validity of first-order perturbation theory for a random distribution of angles [17]. This calculation takes into account the effects of quadrupole shifts and of dipolar magnetic fields. It yields asymmetrical line shape ( $\eta < 1$ ) and line broadening (Fig. 3 and Eq. (19) of [17]).

Similar considerations may be applied to all values of  $p$ . There are however different subsets of quadrupole splittings, quadrupole shifts and of anisotropic hyperfine magnetic field  $B_M^{(2h)}(p)$  values for  $2 \leq p \leq 4$ . The final line is a weighted sum over all lines associated with the different configurations. It is broadened and possibly asymmetric and shifted by a small quadrupole shift according to the relations of the previous section. Non-stoichiometry (Table S2), which would induce a local magnetic disorder [13], may be responsible for an additional broadening. Line broadenings are observed to be large for the subspectra of Sn(2e) sites in Fe-rich stannides with  $x=4.25$  and  $4.5$  (Table S9)  $3.8$  mm/s and  $2.7$  mm/s at  $4.2$  K respectively while they are  $2.5$  mm/s and  $1.7$  mm/s for  $x=5$  and  $6$  respectively (Table S11). These broadenings depend on temperature for  $x=4.25$  and  $4.5$  (Table S9) as does the angle  $\theta$  (Table S5 and Fig. 5 of the article). The explicit calculation of all contributions to line broadening for the various sites of the studied stannides is presently out of reach.

## 2. Mn-rich stannides

In Mn-rich stannides, the quadrupole shifts of Sn(2d) atoms are  $\sim -0.8$  mm/s. However, the mean hyperfine magnetic fields of Sn(2d) atoms with  $p$  Fe neighbors vary from  $\sim 24$  T to  $\sim 31$  T according to the value of  $p$  (Table S8). These hyperfine magnetic fields are predominantly due to isotropic contributions of the six first nearest neighbors of Sn atoms as suggested by first-principle calculations (Sec. VIA of the article). Reasonable values of mean hyperfine magnetic fields are still expected from the use of first order perturbation theory. Only combinations,  $A_M(2h) = A_{isM}(2h) + A_{aeff,M}(2h)/6$  (Eq. (11) of the article,  $\theta = 90^\circ$ ), are calculated for sites ((2d), (2e)) with large hyperfine magnetic fields. Despite the fact that QS(2c)  $\sim 2$  mm/s, hyperfine magnetic fields obtained for Sn(2c) atoms are nevertheless shown in Table S8 to give an idea of their values.

### 3. Conclusion

Hyperfine magnetic fields were observed to change almost not even when different least-squares fits, still satisfactory, yield different values of the other hyperfine parameters and of line widths. The fact that the mean hyperfine magnetic fields of  $\text{Sn}_{2h}(p)$  atoms, with  $h=d$  (Mn-rich) and  $e$  (for any  $x$ ) (Fig. 7), are independent of  $x$  is an additional indication that they are confidently determined. Line broadenings are found to depend on  $x$  (and on temperature because of a moment rotation). The most reliable hyperfine magnetic fields are thus those of tin sites with large hyperfine magnetic fields that is ( $h=d, e$ ) for Mn-rich and  $h=e$  for Fe-rich stannides. They are the only ones from which the constants of the model ( $A_{aM}, A_{isM}$  or a linear combination of them) are obtained and discussed in the article.

## V. MODELS OF $^{119}\text{Sn}$ TRANSFERRED HYPERFINE MAGNETIC FIELDS

Random vectors are denoted hereafter in bold underlined italic fonts while their realizations are in bold italic fonts. The hyperfine magnetic field calculations, which are described below, are first based on a successful model of  $^{119}\text{Sn}$  hyperfine magnetic fields for the different magnetic structures of the distannides  $\text{MSn}_2$  ( $M=\text{Mn, Fe}$ ), both with a  $\text{CuAl}_2$ -type structure and therefore a single  $\text{Sn}(8h)$  site with four  $M$  neighbors [18-21]. It appeared later that the model is physically consistent with the results of first-principles electronic structure calculations in  $\text{HfFe}_6\text{Ge}_6$ -type  $\text{RMn}_6\text{Sn}_6$  stannides ( $R=\text{Li and Mg, Zr, Hf}$ ) (Sec. VIA of the article).

The model of vectorial hyperfine magnetic field applied first to  $\text{MSn}_2$  ( $M=\text{Mn, Fe}$ ) [18-21] consists in a vector addition of anisotropic, dipolar-type, and of isotropic transferred hyperfine magnetic fields at  $\text{Sn}(8h)$  that writes:

$$\mathbf{B}_M^{(8h)} = A_{aM} \sum_{i=1}^n \left[ \mathbf{u}_i (\boldsymbol{\mu}_i \cdot \mathbf{u}_i) - \frac{1}{3} \boldsymbol{\mu}_i \right] + A_{isM} \sum_{i=1}^n \boldsymbol{\mu}_i \quad (1)$$

where the left parenthetical term of the right member represents the dipolar-type part of the transferred hyperfine magnetic field which is due predominantly to a local contribution of  $p$  electrons of Sn assumed to remain localized in each  $M$ -Sn bond ( $M=\text{Mn, Fe}$ ) ( $n=4$  for  $\text{MSn}_2$ ). In Eq. (1),  $\bar{\mathbf{u}}_i$  is a unit vector carried by the bond connecting a central Sn atom to its  $i^{\text{th}}$   $M$  neighbor ( $i=1, \dots, n$ ) whose magnetic moment is  $\boldsymbol{\mu}_i$  as shown in Fig. S5 in the case of  $\text{TmMn}_{6-x}\text{Fe}_x\text{Sn}_6$ . The last term in the right member of Eq. (1) is the isotropic contribution due to the first shell of  $n$   $M$  atoms around the selected  $^{119}\text{Sn}$  atom. Most generally, the  $^{119}\text{Sn}$

hyperfine magnetic fields measured by Mössbauer spectroscopy are actually the moduli of the vectorial hyperfine magnetic fields calculated from Eq. (1). The proportionality constants  $A_{aM}$ ,  $A_{isM}$  convert magnetic moments respectively into anisotropic and isotropic hyperfine magnetic fields. In the literature, the right member of Eq. (1) is sometimes written as  $A_{aM} \sum_{i=1}^n \mathbf{u}_i (\boldsymbol{\mu}_i \cdot \mathbf{u}_i) + A_{isMeff} \sum_{i=1}^n \boldsymbol{\mu}_i$  where  $A_{isMeff} = A_{isM} - A_{aM}/3$ . In some cases, the effective coefficient of Sn(2e) sites in  $\text{RM}_6\text{Sn}_6$ ,  $A_{isMeff}$ , may however differ from the real one by  $\sim 20\%$  [15].

The constants  $A_{aMn}$  for Sn in  $\text{MnSn}_2$  (Eq. (1)) and  $A_{aFe}$  in  $\text{FeSn}_2$  [18-22], taken as positive, are respectively equal to  $A_{aMn} = 2.19 \pm 0.11 \text{ T} \cdot \mu_B^{-1}$  for Mn [18] ( $\mu_{\text{Mn}} = 2.33 \mu_B$  at 4.2 K [23]) and  $A_{aFe} = 2.03 \pm 0.17 \text{ T} \cdot \mu_B^{-1}$  for Fe [20-21] ( $\mu_{\text{Fe}} = 1.70 \mu_B$  at 5 K). Both anisotropic constants were found to be temperature independent [18-21].

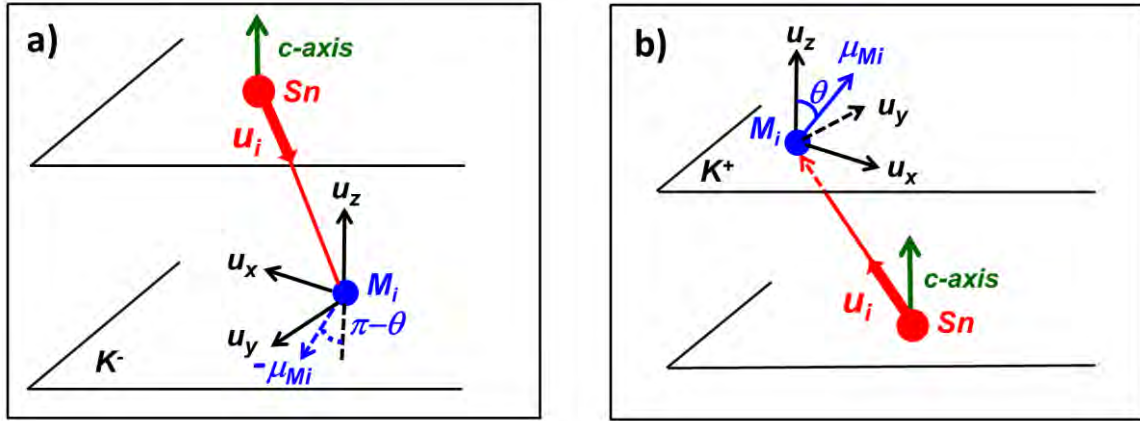


FIGURE S5: Some constituents of the model of  $^{119}\text{Sn}$  hyperfine magnetic fields in  $\text{TmMn}_{6-x}\text{Fe}_x\text{Sn}_6$ :  $M_i$  (in blue) = Mn atom or Fe atom on a nearest neighbour site  $i$  of a given Sn atom (in red);  $\mathbf{u}_i$  is a unit vector carried by the Sn- $M_i$  bond. Shown is an example of antiferromagnetically coupled magnetic moments ( $-\boldsymbol{\mu}_{M_i}$ ,  $\boldsymbol{\mu}_{M_i}$ ) of  $M_i$  atoms which belong to successive kagome planes, namely K- in a) and K+ in b).

The unit vectors ( $\mathbf{u}_x$ ,  $\mathbf{u}_y$ ,  $\mathbf{u}_z$ ) shown in Fig. S5 define an orthonormal coordinate system where  $\mathbf{u}_z = [001]$  is along the c-axis (Fig. S5). The unit vector  $\mathbf{u}_x$ , contained in the plane formed by  $\boldsymbol{\mu}_{M_i}$  and the c-axis, is in the direction of the projection of the  $M_i$  magnetic moment into the kagome plane. Finally, the unit vector  $\mathbf{u}_y$  is defined as the cross product  $\mathbf{u}_y = \mathbf{u}_z \times \mathbf{u}_x$ . The previous moments, contained in ( $\mathbf{u}_x$ ,  $\mathbf{u}_z$ ) planes make an angle  $\theta$  with  $\mathbf{u}_z$ .

Eq. (1) and its extensions work more particularly for HfFe<sub>6</sub>Ge<sub>6</sub>-type RMn<sub>6</sub>Sn<sub>6</sub> stannides and for stannides derived from them by various substitutions of Mn or of Sn. Here R stands most often either for a single species of rare earth atoms or for a mixture of different species. For the sake of completeness, we mention that possible dipolar and isotropic contributions of rare-earth atoms must be included in Eq. (1) to account for <sup>119</sup>Sn hyperfine magnetic fields in ternary RMn<sub>6</sub>Sn<sub>6</sub> stannides as done in studies of RMn<sub>6</sub>Sn<sub>6</sub>, with R=Sc, Y, Tb–Tm, Lu [23]. For TmMn<sub>6-x</sub>Fe<sub>x</sub>Sn<sub>6</sub> pseudo-binary alloys with AFI and AFII magnetic structures, Eq. (1) is replaced by:

$$\mathbf{B}_M^{(2h)} = \sum_{i=1}^6 A_{aMi}(2h) \left[ \mathbf{u}_{Mi} (\boldsymbol{\mu}_{Mi} \cdot \mathbf{u}_{Mi}) - \frac{1}{3} \boldsymbol{\mu}_{Mi} \right] + \sum_{i=1}^6 A_{isMi}(2h) \boldsymbol{\mu}_{Mi} \quad (2)$$

where h=c, d, e, M refers either to Mn or to Fe and “i” to the ith M-Sn bond.

#### A. Anisotropic <sup>119</sup>Sn hyperfine magnetic fields in TmM<sub>6</sub>Sn<sub>6</sub>

First nearest neighbor atoms of tin atoms are either all Mn or all Fe. We sketch below the calculation of the anisotropic hyperfine magnetic field  $\mathbf{B}_{aM}^{(2h)}(K^+)$  whose expression is written from Eq. (2) as:

$$\mathbf{B}_{aM}^{(2h)}(K^+) = A_{aM}(2h) \left\{ \sum_{i=1}^{n(2h)} \mathbf{u}_i(2h) (\boldsymbol{\mu}_M \cdot \mathbf{u}_i(2h)) - \alpha(2h) \boldsymbol{\mu}_M \right\} \quad (3)$$

where  $n(2h) = 3, 3, 6$  and  $\alpha(2h) = n(2h)/3$  (h=c, d, e) respectively. Then, we project both the unit vector  $\mathbf{u}_i(2h)$ , assigned to the ith Sn(2h)-M bond (Fig. S5), and the magnetic moment  $\boldsymbol{\mu}_M$  onto the (ab) plane which contains the considered Sn atom to get respectively  $\mathbf{u}_{abi}(2h)$  and  $\boldsymbol{\mu}_{abM}$ , and on the [001] axis, respectively  $\mathbf{u}_{zM}(2h)$  (independent of i) and  $\boldsymbol{\mu}_{zM}$  :

$$\begin{cases} \mathbf{u}_i(2h) = \mathbf{u}_{abi}(2h) + \mathbf{u}_{zM}(2h) & u_{ab,i}^2(2h) + u_{zM}^2(2h) = 1 \\ \boldsymbol{\mu}_M = \boldsymbol{\mu}_{abM} + \boldsymbol{\mu}_{zM} & \mu_{abM}^2 + \mu_{zM}^2 = \mu_M^2 \end{cases} \quad (4)$$

where  $x^2$  is the square of the modulus of  $x$ . From Eqs (3) and (4), we derive the following intermediate relation:

$$\mathbf{B}_{aM}^{(2h)}(K^+) = A_{aM}(2h) \left\{ \begin{array}{l} \left( \sum_{i=1}^{n(2h)} \mathbf{u}_{abi}(2h) (\boldsymbol{\mu}_{abM}(2h) \cdot \mathbf{u}_{abi}(2h)) \right) \\ + 3\alpha(2h) \mathbf{u}_{zM}(2h) (\boldsymbol{\mu}_{zM}(2h) \cdot \mathbf{u}_{zM}(2h)) - \alpha(2h) \boldsymbol{\mu}_M \end{array} \right\} \quad (5)$$

We consider first the cases where  $n(2h) = 3$  and we define then three unit vectors in the (ab) plane,  $\mathbf{v}_{abk}$  ( $k=1,2,3$ ). These unit vectors are along the lines joining the position of the Sn atom to the vertices of an equilateral triangle which are the projections onto the (ab) plane, which contains this Sn atom, of its three M first nearest neighbors in  $K^+$ . For simplicity, we omit below the site label (2h). These three unit vectors are chosen as:

$$\mathbf{v}_{ab1}(0,1), \mathbf{v}_{ab2}(-\sqrt{3}/2, -1/2), \mathbf{v}_{ab3}(\sqrt{3}/2, -1/2) \quad (6)$$

A fourth unit vector,  $\mathbf{w}_{ab}(\cos\theta, \sin\theta)$ , is such that  $\boldsymbol{\mu}_{abM} = \mu_{abM} \mathbf{w}_{ab}$ . Then:

$$\begin{aligned} \sum_{i=1}^3 \mathbf{u}_{abi} (\boldsymbol{\mu}_{abM} \cdot \mathbf{u}_{abi}) &= \mu_{abM} u_{ab}^2 \left( \sum_{i=1}^3 \mathbf{v}_{abi} (\mathbf{w}_{abi} \cdot \mathbf{v}_{abi}) \right) = \\ &= \frac{3}{2} \mu_{abM} u_{ab}^2 \mathbf{w}_{ab} = \frac{3}{2} u_{ab}^2 \boldsymbol{\mu}_{abM} \end{aligned} \quad (7)$$

Since  $3\mathbf{u}_{zM} (\boldsymbol{\mu}_{zM} \cdot \mathbf{u}_{zM}) = 3u_{zM}^2 \boldsymbol{\mu}_{zM}$  (Eq. (5)), it comes:

$$\mathbf{B}_{aM}(K^+) = A_{aM} \left\{ \frac{3}{2} u_{ab}^2 \boldsymbol{\mu}_{abM} + 3u_{zM}^2 \boldsymbol{\mu}_{zM} - \boldsymbol{\mu}_M \right\} \quad (8)$$

thus:

$$\mathbf{B}_{aM}(K^+) = A_{aM} \left( \frac{1-3u_{zM}^2}{2} \right) \{ \boldsymbol{\mu}_M - 3\boldsymbol{\mu}_{zM} \} = \frac{A_{aM}}{2} \times \{ \boldsymbol{\mu}_M - 3\boldsymbol{\mu}_{zM} \} \quad (9)$$

A calculation can be performed for site Sn(2e) along the same line with  $n(2e) = 6$ , i.e. with six unit vectors instead of three in an ab plane. We obtain finally:

$$\overline{B}_{aM}^{(2h)}(K^+) = A_{aM}^{(2h)} [\alpha(2h)/2] \times \{ \boldsymbol{\mu}_M - 3\boldsymbol{\mu}_{zM} \} \quad (10)$$

The effective anisotropic constant:

$$A_{aM}^{(2h)}(2h) = A_{aM}(2h) (1 - 3u_{zM}^2(2h)) \quad (11)$$

which appears in Eqs (9) and (10), is useful to express the relations derived in the next section. In Eq. (11), M=(Mn, Fe) while  $u_{zM}(2h)$  is the common length of the projections on

the c-axis of the unit vectors carried by Sn(2h)-M bonds ( $u_{zMn}(2h)$  and  $u_{zFe}(2h)$  are a priori different). The considered Sn(2h) sites are such that h=(c, d, e) for ferromagnetic stannides (examples are given in [23]). They are respectively such that h=(d, e) and h=e for the antiferromagnetic structures AFII and AFI (Fig. 2 of the article).

The constant  $A_{aeff,M}(2h)$  includes a geometrical factor  $(1-3u_{zM}^2(2h))$  which would be equal to zero if Sn(2h)-M bonds made a « magic angle » ( $\phi_m = 54.735..^\circ$ ) with the c-axis. In most  $\text{RMn}_{6-x}\text{Fe}_x\text{Sn}_6$  stannides, the effective anisotropic constant  $A_{aeff,M}(2h)$  has the same sign as  $A_{aM}(2h)$  for Sn(2e) atoms while it has the opposite sign for Sn(2c) and Sn(2d) atoms. For instance, the geometrical factors calculated from Table S2 for  $\text{TmMn}_{6-x}\text{Fe}_x\text{Sn}_6$  are typically, for any x,  $(1-3u_{zM}^2(2e)) \approx 0.8$  and  $(1-3u_{zM}^2(2h)) \approx -1.25$  (h=c, d). Angles  $\phi(2e)$  of  $\sim 75^\circ$  ( $> \phi_m$ ) and  $\phi(2h)$  (h=c, d) of  $\sim 30^\circ$  ( $< \theta_m$ ) are made by Sn(2h)-M bonds with the c-axis.

### **B. $^{119}\text{Sn}$ hyperfine magnetic fields when the M moments make an angle $\theta$ with the c-axis**

The M moments,  $\mu_M(T)$ , are assumed to make an angle  $\theta$  with the c-axis at a given temperature T. The components of the total hyperfine field in the  $(\mathbf{u}_x, \mathbf{u}_y, \mathbf{u}_z)$  frame of reference (Fig. S5) are obtained from Eq. (2) and from Eq. (10) to be:

$$\mathbf{B}_{M,T}^{(2h)}(\theta) = B_{M,T}^{(2h)}(90^\circ) \sin \theta \times \mathbf{u}_x + B_{M,T}^{(2h)}(0^\circ) \cos \theta \times \mathbf{u}_z \quad (12)$$

For Sn(2h) sites whose neighbors are ferromagnetically coupled, it comes:

$$\begin{cases} B_{M,T}^{(2h)}(90^\circ) = (6A_{isM}(2h) + A_{aeff,M}(2h)) \mu_M(T) \\ B_{M,T}^{(2h)}(0^\circ) = (6A_{isM}(2h) - 2A_{aeff,M}(2h)) \mu_M(T) \end{cases} \quad (13)$$

We define too a coefficient,  $\rho_{eff,M}^{(2h)}$ , which is basically constant in the investigated temperature ranges:

$$\rho_{eff,M}^{(2h)} = \frac{A_{aeff,M}(2h)}{A_{isM}(2h)} = \left[ \frac{A_{aM}(2h)}{A_{isM}(2h)} \right] \times (1-3u_{zM}^2(2h)) \quad (14)$$

The measured hyperfine magnetic field, at a temperature  $T$ ,  $B_{M,T}^{(2h)}(\theta)$  is the modulus of  $\mathbf{B}_{M,T}^{(2h)}(\theta)$  (Eq. (12)). Actually, we need to compare hyperfine magnetic fields, at different temperatures  $T_1$  and  $T_2$  at which magnetic moments make respectively angles  $\theta_1$  and  $\theta_2$  with the c-axis. For this reason, we define:

$$b_{M,T_k}^{(2h)}(\theta_k) = B_{M,T_k}^{(2h)}(\theta_k) / \mu_M(T_k) \quad (15)$$

where  $\mu_M(T_k)$  is the magnetic moment of M at a temperature  $T_k$ . We consider first the case where  $\theta_1 = 0^\circ$  at  $T_1$ . We write, from Eqs (12 to 15):

$$\frac{b_{M,T_2}^{(2h)}(\theta_2)}{b_{M,T_1}^{(2h)}(0^\circ)} = \sqrt{\left(1 + \left\{3\rho_{eff,M}^{(2h)} \left(12 - \rho_{eff,M}^{(2h)}\right) / \left(4 \left(3 - \rho_{eff,M}^{(2h)}\right)^2\right)\right\} \times \sin^2(\theta_2)\right)} \quad (16)$$

Eq. (16) is of practical interest to estimate the experimental value of  $\rho_{eff,M}^{(2h)}$  if  $b_{M,T}^{(2h)}(0^\circ)$  is known. We consider now the case where  $b_{M,T}^{(2h)}(0^\circ)$  cannot be accessed experimentally. It is nevertheless possible to estimate experimentally  $\rho_{eff,M}^{(2h)}$  from Eq. (16) and from two hyperfine magnetic fields,  $b_{M,T_1}^{(2h)}(\theta_1)$  and  $b_{M,T_2}^{(2h)}(\theta_2)$ . To this end, we consider the ratio ( $\theta_1 \neq \theta_2$ ):

$$r_{12} = \frac{b_{M,T_2}^{(2h)}(\theta_2)^2 - b_{M,T_1}^{(2h)}(\theta_1)^2}{b_{M,T_1}^{(2h)}(\theta_1)^2 \sin^2(\theta_2) - b_{M,T_2}^{(2h)}(\theta_2)^2 \sin^2(\theta_1)} \quad (17)$$

or equivalently:

$$r_{12} = \frac{\mu_M(T_1)^2 B_{M,T_2}^{(2h)}(\theta_2)^2 - \mu_M(T_2)^2 B_{M,T_1}^{(2h)}(\theta_1)^2}{\mu_M(T_2)^2 B_{M,T_1}^{(2h)}(\theta_1)^2 \sin^2(\theta_2) - \mu_M(T_1)^2 B_{M,T_2}^{(2h)}(\theta_2)^2 \sin^2(\theta_1)} \quad (18)$$

Eqs (16) and (17) yield:

$$r_{12} = \frac{3\rho_{eff,M}^{(2h)} \left(12 - \rho_{eff,M}^{(2h)}\right)}{4 \left(3 - \rho_{eff,M}^{(2h)}\right)^2} \quad (19)$$

From literature results [23-28], a range (-1, +1) for  $\rho_{eff,Mn}^{(2h)}$  suffices for any composition of the stannides studied in the present work. Because of the values of geometrical factors discussed above, the typical maximum value of  $\rho_{Mn}^{(2h)}$  is  $\sim 0.7$ . Then Eq. (19) shows that  $\rho_{eff,Mn}^{(2h)}$  and  $r_{12}$  are of the same sign and that  $r_{12}$  varies between  $\approx -0.61$  and  $\approx 2.06$  when  $|\rho_{eff,Mn}^{(2h)}| \leq 1$ . From Eq. (19), we deduce the following quadratic equation:

$$\rho_{eff,M}^{(2h)2} \times (3 + 4r_{12}) - 12\rho_{eff,M}^{(2h)} \times (3 + 2r_{12}) + 36r_{12} = 0 \quad (20)$$

If  $r_{12} = 0$  for any pair of angles, then the anisotropic contribution is equal to zero, i.e.  $\rho_{eff,M}^{(2h)} = 0$ . The sole solution of Eq. (20) to be retained is thus:

$$\rho_{eff,M}^{(2h)} = 6(3 + 2r_{12} - 3\sqrt{1 + r_{12}}) / (3 + 4r_{12}) \quad (21)$$

A convenient rewriting of Eq. (16) for  $T_1 = T_2 = T$  and  $\theta_2 = \theta$ ,  $\theta_1 = 0^\circ$  yields (M=Mn, Fe):

$$B_{M,T}^{(2h)}(\theta) = |A_{isM}^{(2h)}| \mu_M(T) \sqrt{\left(6 + \rho_{eff,M}^{(2h)}\right)^2 - 3\cos^2(\theta) \rho_{eff,M}^{(2h)} \left(12 - \rho_{eff,M}^{(2h)}\right)} \quad (22)$$

The square-root in Eq. (22) appears then as some kind of effective angular number of neighbors.

If moment rotations take place in temperature ranges, where the ratios of moments remain essentially equal to 1, then Eq. (16) shows immediately that the variations,  $\delta B_M^{(2h)}(\theta_2) = B_{M,T_2}^{(2h)}(\theta_2) - B_{M,T_1}^{(2h)}(0^\circ)$  have the same sign as  $\rho_{eff,M}^{(2h)}$  for any  $0^\circ < \theta_2 \leq 90^\circ$ . If  $\rho_{eff,M}^{(2h)}$  is positive (r.s.p. negative) for a given h, then the experimental Sn(2h) hyperfine magnetic field increases (r.s.p. decreases) for any deviation of the M moment from the c-axis.

### ***C. Some literature results for $RMn_6Sn_{6-x}X_x$ compounds***

A spin reorientation from the [001] c-axis to the (001) kagome plane is, for instance, field-driven for  $TbMn_6Sn_{5.46}In_{0.54}$ , for  $YMn_6Sn_{5.42}In_{0.58}$  and for  $RMn_6Sn_{6-x}X_x$  (R=Y, Tb, Er, X=In, Ga) [15]. It is temperature driven in a narrow temperature range for  $TbMn_6Sn_{6-x}Ga_x$

and for  $\text{ErMn}_6\text{Sn}_{6-x}\text{Ga}_x$  [26-27]. In all these compounds,  $\delta B_{Mn}^{(2e)}(90^\circ) > 0$  while  $\delta B_{Mn}^{(2c)}(90^\circ)$  and  $\delta B_{Mn}^{(2d)}(90^\circ) < 0$  as expected from the above discussion if  $A_{aM}(2h)$  and  $A_{isM}(2h)$  have the same sign, i.e.  $\rho_{eff,M}^{(2e)} > 0$  and  $\rho_{eff,M}^{(2c)}, \rho_{eff,M}^{(2d)} < 0$  (Eq. (14)). For  $\text{YMn}_6\text{Sn}_{5.42}\text{In}_{0.58}$  the hyperfine magnetic field changes were reported to be respectively  $\delta B_{Mn}^{(2h)}(90^\circ) = -1.9(8)\text{T}$ ,  $-2.1(3)\text{T}$  and  $6.4(3)\text{T}$  for  $h=c, d, e$  [15]. The ratios of these changes, independent of  $\mu_{Mn}$ , show that the constants  $A_{aMn}(2h)$  ( $h=c, d$ ) have similar values while  $A_{aMn}(2e) \sim 4.5A_{aMn}(2d)$ .

## VI. MODELS OF TRANSFERRED HYPERFINE MAGNETIC FIELDS AT Sn SITES IN PSEUDO-BINARY ALLOYS $\text{TmMn}_{6-x}\text{Fe}_x\text{Sn}_6$

The calculation of transferred hyperfine magnetic fields from Eq. (2) requires to make assumptions on the parameters associated with the six Sn(2h)-M (=Mn, Fe) bonds of any tin site. They are recalled here:

- a) The anisotropic and isotropic constants  $A_{aM}(2h)$  and  $A_{isM}(2h)$  are assumed to be identical for all Sn(2h)-M bonds where M is either Mn or Fe.
- b) The projections on the c-axis of unit vectors carried by Sn(2h)-M bonds are all assumed to have the same lengths as are all corresponding projections onto the ab plane (Fig. S5). Projection lengths differ however when M is either Mn or Fe. The projection lengths are denoted respectively as  $u_{zM}(2h)$  (c-axis) and  $u_{abM}(2h)$  (ab plane).
- c) Fe and Mn magnetic moments remain ferromagnetically coupled in their kagome planes

All M sites, assumed to be occupied at random by Mn and Fe atoms in  $\text{TmMn}_{6-x}\text{Fe}_x\text{Sn}_6$ , are then statistically equivalent for a random substitution of Mn atoms with Fe atoms. However, from the point of view of tin sites and of their associated hyperfine magnetic fields, the statistical equivalency of their six M nearest neighbors depends further on local magnetic structures. This leads us to distinguish two cases which are relevant for the AFI and AFII magnetic structures we consider primarily.

### A. $^{119}\text{Sn}$ hyperfine magnetic field variations for six equivalent M NN sites

The statistical equivalence of the six first nearest neighbor sites of any tin site implies that the moments  $\mu_{Mni}$  and  $\mu_{Fei}$  do not depend on “ $i$ ” and become simply  $\mu_{Mn}$  and  $\mu_{Fe}$ , which are obtained experimentally at the considered temperature. The random magnetic moment  $\mu_{Mi}$  depends of course of “ $i$ ”, being equal either to  $\mu_{Mn}$  or to  $\mu_{Fe}$ . Two random

vectors,  $\underline{\mu}_{Mi}$  and  $\underline{u}_{Mi}$ , are thus involved in the calculation of the anisotropic contribution of any site “ $i$ ” to the total anisotropic hyperfine magnetic field.

The two anisotropic hyperfine magnetic fields,  $\mathbf{B}_{aMn}^{(2h)} = \sum_{i=1}^6 \mathbf{X}_{Mni}$  and  $\mathbf{B}_{aFe}^{(2h)} = \sum_{i=1}^6 \mathbf{X}_{Fei}$

$\left( \mathbf{X}_{Mi} = A_{aM}(2h) \times \left\{ \underline{u}_{Mi} (\underline{\mu}_{Mi} \cdot \underline{u}_{Mi}) - \frac{\underline{\mu}_{Mi}}{3} \right\} \right)$  (M=Mn or Fe) are associated with Sn(2h) atoms (h=c, d, e) which have respectively six Mn and six Fe nearest neighbors. The moments  $\underline{\mu}_{Mni}$  and  $\underline{\mu}_{Fei}$  are obtained from the magnetic structure at the given Fe content and temperature. In the same way, the two isotropic hyperfine magnetic fields of the latter Sn atoms are respectively  $\mathbf{B}_{isMn}^{(2h)} = 6A_{isMn}(2h)\underline{\mu}_{Mn}$  and  $\mathbf{B}_{isFe}^{(2h)} = 6A_{isFe}(2h)\underline{\mu}_{Fe}$  while the two total hyperfine magnetic fields are respectively  $\mathbf{B}_{Mn}^{(2h)} = \mathbf{B}_{aMn}^{(2h)} + \mathbf{B}_{isMn}^{(2h)}$  and  $\mathbf{B}_{Fe}^{(2h)} = \mathbf{B}_{aFe}^{(2h)} + \mathbf{B}_{isFe}^{(2h)}$ . In summary, all the random vectors needed to characterize the hyperfine magnetic fields are:

$$\begin{aligned}
& - \underline{\mathbf{B}}_{aM}^{(2h)} = \sum_{i=1}^6 (\underline{\mathbf{X}}_{Mi}) \\
& - \underline{\mathbf{X}}_{Mi} = A_{aMi}(2h) \times [\underline{u}_{Mi} (\underline{\mu}_{Mi} \cdot \underline{u}_{Mi}) - \underline{\mu}_{Mi}/3] \\
& - \underline{\mathbf{B}}_{isM}^{(2h)} = \sum_{i=1}^6 (A_{isMi}(2h) \underline{\mu}_{Mi}) \\
& - \underline{\mathbf{B}}_M^{(2h)} = \underline{\mathbf{B}}_{aM}^{(2h)} + \underline{\mathbf{B}}_{isM}^{(2h)}
\end{aligned} \tag{23}$$

We aim to calculate the average hyperfine magnetic fields of Sn<sub>2h</sub>( $p$ ) atoms ( $p$  Fe first nearest neighbors, section IVB), for a given  $x$ . The Fe content determines, at a given temperature, the relative areas of sites Sn<sub>2h</sub>( $p$ ) with respect to all Sn sites and it influences the associated hyperfine magnetic fields  $\mathbf{B}_M^{(2h)}(p)$  through anisotropic and isotropic constants. However, the latter are found to be weakly dependent of  $x$  in Mn-rich and in Fe-rich stannides (Tables S8 and S9). The random isotropic hyperfine magnetic field  $\underline{\mathbf{B}}_{isM}^{(2h)}(p)$  takes a single value because the relative positions of Mn and of Fe play no role. The calculation of this value, which is too its mean, is straightforward:

$$\underline{\mathbf{B}}_{isM}^{(2h)}(p) = (6-p)A_{isMn}(2h)\underline{\mu}_{Mn} + pA_{isFe}(2h)\underline{\mu}_{Fe} = \underline{\mathbf{B}}_{isMn}^{(2h)} - \frac{p}{6} \times (\underline{\mathbf{B}}_{isMn}^{(2h)} - \underline{\mathbf{B}}_{isFe}^{(2h)}) \tag{24}$$

From site equivalence, the conditional probability that a Sn atom with  $p$  Fe neighbours has a M atom as its  $i$ th neighbor is simply  $p/6$  for M=Fe and thus  $1-p/6$  for M=Mn. The

previous probabilities differ from those of a random, unconditional, occupation of site “ $i$ ” by Fe or by Mn which are respectively  $x/6$  and  $1-x/6$ . A simple alternative method starts from the total number of configurations of  $p$  Fe atoms around a  $\text{Sn}_{2h}(p)$  atom which is  $\binom{6}{p}$ . Then, we single out those  $\text{Sn}_{2h}(p)$  atoms with a Fe atom in a neighboring site “ $i$ ”, chosen among the six ( $1 \leq p \leq 6$ ). The number of configurations is found by selecting at random  $p-1$  sites in all possible ways among the remaining five sites. The probability that a Sn atom with  $p$  Fe neighbours has a Fe atom as its  $i$ th neighbor is, without surprise, equal to  $\binom{5}{p-1} / \binom{6}{p} = \frac{p}{6}$ . Because of the statistical equivalence of the six sites, the previous conditional probabilities are identical for any first nearest neighbor site chosen among the six but the probability that  $n$  selected sites ( $2 \leq n \leq p \leq 5$ ) are occupied simultaneously by Fe atoms differs from  $(p/6)^n$ . Indeed, these events are not independent as the total number of Fe neighbors must be exactly  $p$ . Fortunately, the mean of a sum is the sum of the means of its random terms regardless of whether or not they are independent. The mean field,  $\mathbf{B}_M^{(2h)}(p)$ , is finally obtained from Eq. (23) which yields first the average anisotropic component:

$$\mathbf{B}_{aM}^{(2h)}(p) = \sum_{i=1}^6 ((1-p/6) \mathbf{X}_{Mni} + (p/6) \mathbf{X}_{Fei}) = \mathbf{B}_{aMn}^{(2h)} - p \times \left\{ \mathbf{B}_{aMn}^{(2h)} - \mathbf{B}_{aFe}^{(2h)} \right\} / 6 \quad (25)$$

to which we add the average isotropic part given by Eq. (24) to get finally the average total hyperfine magnetic field,  $\mathbf{B}_M^{(2h)}(p)$ :

$$\mathbf{B}_M^{(2h)}(p) = \mathbf{B}_{Mn}^{(2h)} - p \times \left\{ \mathbf{B}_{Mn}^{(2h)} - \mathbf{B}_{Fe}^{(2h)} \right\} / 6 \quad (26)$$

The latter field, is thus a weighted sum, linear in  $p$ , of the two hyperfine magnetic fields  $\mathbf{B}_{Mn}^{(2h)}$  and  $\mathbf{B}_{Fe}^{(2h)}$ , measured at the same temperatures for the given Fe content. The calculation of the variance of the distribution of the total hyperfine magnetic field,  $\mathbf{B}_M^{(2h)}(p)$ , is somewhat more involved. The latter variance is solely due to the anisotropic part of the total hyperfine magnetic field,  $\mathbf{B}_{aM}^{(2h)}(p)$ . The dispersion of  $\mathbf{B}_M^{(2h)}(p)$  contributes to Mössbauer line broadening of the spectral component due to  $\text{Sn}_{2h}(p)$  atom, possibly asymmetrical to some extent.

Eq. (26) is essentially a consequence of the linearity of the site contributions to hyperfine magnetic fields (Eqs (23)). Thus, the linear behavior is arguably a first-order approximation, even if more involved hypotheses would be actually required to explain anisotropic hyperfine magnetic fields. An example of the latter might be the necessity to take into account possible effects of the relative positions of Fe neighbors on local distortions of Sn-Fe bonds. In any case, we explore the consequences of Eq. (26), when applied to various magnetic structures, to see how far they account for experimental results.

***B.  $^{119}\text{Sn}$  hyperfine magnetic field variations for two groups of three equivalent M NN sites***

The tin atoms considered below, Sn(2h), are sandwiched between two ferromagnetic kagome planes which are antiferromagnetically coupled. The index h is for instance h=c for the AFII structure while it is h=c, d for the AFI structure (Fig. 2 of the article). The moments of M atoms (M=Mn or Fe) sitting on the latter sites are thus  $\mu_{Mn}$  and  $\mu_{Fe}$  for one of the two kagome planes, say  $K^+$ , and  $-\mu_{Mn}$  and  $-\mu_{Fe}$  for the other,  $K^-$ . Statistical equivalence holds separately for the two groups of three nearest neighbor sites of the selected Sn(2h) sites contained in  $K^-$  and in  $K^+$  (Fig. S5). The numbers of Fe atoms in  $K^-$  and in  $K^+$  are denoted respectively as  $p_1$  and  $p_2=p-p_1$ . The addition of the isotropic contributions of M atoms in the two kagome planes, yields then:

$$\mathbf{B}_{isM}^{(2h)}(p_1, p_2) = (p_1 - p_2) \times \{A_{isMn}(2h)\mu_{Mn} - A_{isFe}(2h)\mu_{Fe}\} \quad (27)$$

If the AFI and AFII structures are either easy-plane or easy-axis and if the anisotropic hyperfine magnetic fields are negligible, then the modulus of the hyperfine magnetic field given Eq. (27) writes:

$$B_M^{(2h)}(N_{Fe}) = N_{Fe} \times |A_{isMn}(2h)\mu_{Mn} - A_{isFe}(2h)\mu_{Fe}| \quad (28)$$

where  $N_{Fe} = |p_2 - p_1|$  plays the role of an “effective” number of Fe nearest neighbors.

Sites of M atoms, with superscripts (-) and (+), numbered below from 1 to 3, are located respectively in kagome planes  $K^-$  and  $K^+$  (Fig. S5). The calculation of the anisotropic hyperfine magnetic fields at Sn(2h) sites, where the values of h are defined above, is performed in two steps which correspond:

a) first to the case where Sn(2h) sites are surrounded by six identical M atoms (M is either Mn or Fe). As,  $p_1 = p_2 = 0$  for M=Mn and  $p_1 = p_2 = 3$  for M=Fe,  $N_{Fe}$  is equal to zero in both cases. The anisotropic hyperfine magnetic fields (Eq. (23)) are equal to zero because of the antiferromagnetic coupling of  $K^-$  and  $K^+$ . Indeed,  $\mathbf{B}_{aMn}^{(2h)} = \sum_{i=1}^3 (\mathbf{X}_{Mi}^{(+)} + \mathbf{X}_{Mi}^{(-)}) = \mathbf{B}_{aM}^{(2h)}(K^+) + \mathbf{B}_{aM}^{(2h)}(K^-) = 0$  (Eq. (10), h=c, d). By the same token, the isotropic hyperfine magnetic fields,  $\mathbf{B}_{isM}^{(2h)}$ , and the total hyperfine magnetic fields,  $\mathbf{B}_M^{(2h)}$ , are also equal to zero.

b) then to the case where Sn(2h) sites are surrounded by a total of  $6-p$  Mn atoms and of  $p$  Fe atoms whose repartition in  $K^-$  and  $K^+$  is defined above. The calculation parallels the one performed in the previous section (Eq. (25)). As  $\sum_{i=1}^3 (\mathbf{X}_{Mi}^{(+)} + \mathbf{X}_{Mi}^{(-)}) = 0$ , we write first:

$$\mathbf{B}_{aM}^{(2h)}(p_1, p_2) = (p_1/3) \times \left[ \sum_{i=1}^3 (\mathbf{X}_{Fei}^{(-)} - \mathbf{X}_{Mni}^{(-)}) \right] + (p_2/3) \times \left[ \sum_{i=1}^3 (\mathbf{X}_{Fei}^{(+)} - \mathbf{X}_{Mni}^{(+)}) \right] \quad (29)$$

as  $p_i/3 = p_j/3 + (p_i - p_j)/3$ , we apply the latter relation to Eq. (29), first for  $i=1, j=2$  and then for  $i=2, j=1$ , to get:

$$\begin{aligned} \mathbf{B}_{aM}^{(2h)}(p_1, p_2) &= \{(p_1 - p_2)/3\} \times \left[ \sum_{i=1}^3 (\mathbf{X}_{Fei}^{(-)} - \mathbf{X}_{Mni}^{(-)}) \right] = \\ &= \{(p_2 - p_1)/3\} \times \left[ \sum_{i=1}^3 (\mathbf{X}_{Fei}^{(+)} - \mathbf{X}_{Mni}^{(+)}) \right] \end{aligned} \quad (30)$$

An explicit expression is finally obtained from Eq. (10):

$$\mathbf{B}_{aM}^{(2h)}(p_1, p_2) = [(p_1 - p_2)/6] \times \{A_{a\text{eff}, Mn}(2h) \{\boldsymbol{\mu}_{Mn} - 3\boldsymbol{\mu}_{zMn}\} - A_{a\text{eff}, Fe}(2h) \{\boldsymbol{\mu}_{Fe} - 3\boldsymbol{\mu}_{zFe}\}\} \quad (31)$$

where  $A_{a\text{eff}, M}(2h)$  is defined by Eq. (11). For convenience, we define further:

$$\boldsymbol{\Omega}_M(2h) = (A_{isM}(2h) + A_{a\text{eff}, M}(2h)/6) \boldsymbol{\mu}_M - (A_{a\text{eff}, M}(2h)/2) \boldsymbol{\mu}_{zM} \quad (32)$$

where M is either Mn or Fe. The total hyperfine magnetic field, the sum of Eqs (27) and (31), is expressed with the help of Eq. (32) as:

$$\mathbf{B}_M^{(2h)}(p_1, p_2) = (p_1 - p_2) \times \{\boldsymbol{\Omega}_{Mn}(2h) - \boldsymbol{\Omega}_{Fe}(2h)\} \quad (33)$$

The predicted ‘‘Mössbauer’’ hyperfine magnetic field,  $B_{pred}^{(2h)}(N_{Fe})$ , is thus:

$$B_{pred}^{(2h)}(N_{Fe}) = N_{Fe} \times \|\mathcal{Q}_{Mn}(2h) - \mathcal{Q}_{Fe}(2h)\| \quad (34)$$

Eq. (34) yields notably,  $B_{pred}^{(2h)}(0) = 0$ .

## VII. HYPERFINE PARAMETERS FITTED FROM $^{119}\text{Sn}$ MÖSSBAUER SPECTRA OF $\text{TmMn}_{6-x}\text{Fe}_x\text{Sn}_6$

In Table S8, the magnetic hyperfine fields in italics are associated with components whose relative areas are smaller than 0.05. They are seen to be consistent with those obtained for larger areas or/and for different Fe contents. Small hyperfine magnetic field values, which are considered as being only illustrative of the true values, are in italic type (Sn(2c)).

For Tables S8 and S9 given below, IS is the isomer shift with respect to  $\text{BaSnO}_3$  at RT,  $\Gamma$  the full-width at half-maximum of Mössbauer lines,  $2\varepsilon$  the quadrupole shift, QS the quadrupole splitting (Sec. IV). A sextet with a hyperfine magnetic field  $B_{exp}^{(2h)}(n)$  has an area,  $\text{Area}(n)$ , the fraction of the total area comprised between the spectrum and its background measured far from resonance peaks.

**TABLE S8:**

$^{119}\text{Sn}$  hyperfine magnetic fields  $B_{exp}^{(2h)}(n)$  of sites 2h (h=d, e, c), at different temperatures, in Mn-rich  $\text{TmMn}_{6-x}\text{Fe}_x\text{Sn}_6$  stannides ( $x = 0.4, 0.6$  and  $1.2$ ) from least-squares fitted spectra. The parameter  $n$  represents either the number  $p$  of Fe neighbors for  $\text{Sn}_{2d}$  and  $\text{Sn}_{2e}$  atoms or an effective number of neighbors  $N_{Fe}$  (table S7) for  $\text{Sn}_{2c}$  atoms.

Sn(2d)	Fe <sub>0.4</sub>	Fe <sub>0.6</sub>	Fe <sub>1.2</sub>
Temperature	55 K	46 K	30 K
IS(mm/s)	2.19	2.17	2.21
$2\varepsilon$ (mm/s)	-0.79	-0.78	-0.82
$\Gamma$ (mm/s)	1.31	1.32	1.44
$B_{exp}^{(2d)}(0)$ (T)	31.1	31.4	31.5
Area(0)	0.21	0.17	0.08
$B_{exp}^{(2d)}(1)$ (T)	27.4	27.7	27.7
Area(1)	0.11	0.12	0.14
$B_{exp}^{(2d)}(2)$ (T)	24.6	24.8	24.2
Area(2)	0.02	0.02	0.07
$B_{exp}^{(2d)}(3)$ (T)	-	23.8	22.9
Area(3)	-	0.01	0.03
Sn(2e)			

IS(mm/s)	2.09	2.07	2.07
2ε (mm/s)	-0.07	-0.10	-0.21
Γ(mm/s)	1.58	1.58	1.87
$B_{\text{exp}}^{(2e)}(0)$ (T)	21.4	21.5	20.3
Area(0)	0.20	0.17	0.10
$B_{\text{exp}}^{(2e)}(1)$ (T)	19.2	19.2	18.4
Area(1)	0.11	0.13	0.11
$B_{\text{exp}}^{(2e)}(2)$ (T)	15.7	16.1	16.3
Area(2)	0.02	0.03	0.08

**TABLE S8** (continued)

Sn(2c)	Fe <sub>0.4</sub>	Fe <sub>0.6</sub>	Fe <sub>1.2</sub>
Temperature	55 K	46 K	30 K
IS (mm/s)	1.94	1.93	1.95
QS (mm/s)	1.04	1.04	1.02
Γ (mm/s)	1.51	1.58	2.13
$B_{\text{exp}}^{(2c)}(0)$ (T)	0	0	0
Area(0)	0.21	0.20	0.16
$B_{\text{exp}}^{(2c)}(1)$ (T)	3.6	3.5	3.5
Area(1)	0.09	0.12	0.16

**TABLE S9:**

<sup>119</sup>Sn hyperfine parameters at Sn(2e) sites in Fe-rich TmMn<sub>6-x</sub>Fe<sub>x</sub>Sn<sub>6</sub> stannides (x = 4.25, 4.5) from least-squares fitted spectra.

Sn(2e)	Fe <sub>4.25</sub>	Fe <sub>4.25</sub>	Fe <sub>4.25</sub>	Fe <sub>4.5</sub>	Fe <sub>4.5</sub>	Fe <sub>4.5</sub>
Temperature	4.2 K	51 K	300 K	4.2 K	72K	300K
IS(mm/s)	1.97	1.97	1.74	1.96	2.13	1.95
2ε (mm/s)	0.43	0.63	0.43	0.35	0.51	0.32
Γ(mm/s)	3.83	2.74	2.14	3.39	4.06	2.74
$B_{\text{exp}}^{(2e)}(3)$ (T)	10.4	6.8	6.4	11.5	4.9	12.6
Area(3)	0.07	0.06	0.04	0.05	0.05	0.05
$B_{\text{exp}}^{(2e)}(4)$ (T)	14.9	9.0	9.7	15.1	8.6	14.5
Area(4)	0.14	0.10	0.08	0.11	0.11	0.10
$B_{\text{exp}}^{(2e)}(5)$ (T)	18.0	11.7	12.4	18.1	12.1	17.0
Area(5)	0.13	0.11	0.08	0.13	0.13	0.13
$B_{\text{exp}}^{(2e)}(6)$ (T)	20.4	14.7	15.0	21.2	16.6	19.7
Area(6)	0.05	0.04	0.03	0.07	0.06	0.06

## VIII. MODELS OF $^{119}\text{Sn}$ HYPERFINE MAGNETIC FIELDS IN Mn-RICH $\text{TmMn}_{6-x}\text{Fe}_x\text{Sn}_6$

### A. Sn(2d) and Sn(2e) sites

The sextets associated with Sn(2h) atoms (h=d, e) with  $p$  Fe neighbors,  $\text{Sn}_{2h}(p)$ , are characterized, among others, by their experimental hyperfine magnetic fields,  $B_{\text{exp}}^{(2h)}(p)$  which vary linearly with  $p$  (Fig. 7 of the article) in agreement with the predicted variations of Sec. VIA (Eq. (26)), and by their relative areas  $f_{2h}(p)$ , or equivalently by their relative fractions. All parameters obtained from least-squares fits of Mössbauer spectra are collected in Table S8 while observed and calculated spectra are shown in Fig. S6. The non-linear fitting method we used required to guess initial relative areas  $f_{2h0}(p)$ . They were taken from the binomial distribution as  $P(p)/3$  (Table S6), for sites Sn(2d) and Sn(2e) and from Eq. (38) discussed below for sites Sn(2c). These initial values lead to satisfactorily fitted spectra even though the number of subspectra is large. The final fitted areas remain in good agreement with the expected areas (Table S8).

### B. Sn(2c) atoms

Central high-amplitude components of Mössbauer spectra of  $\text{TmMn}_{6-x}\text{Fe}_x\text{Sn}_6$  seen for  $x=0.4$  and  $0.6$  (Fig. S6) are attributed to Sn(2c) atoms, which are sandwiched between two antiferromagnetically coupled kagome planes  $K^-$  and  $K^+$  (Fig. S5). Further, spectra display shoulders on both wings of the central component.

#### 1. Predicted values of Sn(2c) hyperfine magnetic fields

The predicted value of Sn(2c) hyperfine magnetic fields for atoms, which have  $p_1$  Fe atoms in one of the two kagome planes and  $p_2 = p - p_1$  in the other, writes:

$$B_{\text{pred}}^{(2c)}(N_{\text{Fe}}) = N_{\text{Fe}} \times \|\boldsymbol{\Omega}_{\text{Mn}}(2c) - \boldsymbol{\Omega}_{\text{Fe}}(2c)\| \quad (35)$$

where  $N_{\text{Fe}} = |p_1 - p_2|$  varies between 0 and 3 for the different configurations given in Table S7 and the  $\boldsymbol{\Omega}_M(2c)$ 's are (Sec. VIB, Eqs (32) to (34)):

$$\boldsymbol{\Omega}_M(2c) = \left( A_{\text{isM}}(2c) + A_{\text{aeff},M}(2c)/6 \right) \boldsymbol{\mu}_M - \left( A_{\text{aeff},M}(2c)/2 \right) \boldsymbol{\mu}_{zM} \quad (36)$$

For the easy-plane AFII structure of Mn-rich stannides, it comes  $\mu_{zM} = 0$  which yields a simplified version of Eq. (35) ( $A_M(2c) = A_{isM}(2c) + A_{aef,M}(2c)/6$ , M=Mn, Fe):

$$B_{pred}^{(2c)}(N_{Fe}) = N_{Fe} \times |A_{Mn}(2c)\mu_{Mn} - A_{Fe}(2c)\mu_{Fe}| \quad (37)$$

Both Eqs (35) and (37) predict that  $B_{pred}^{(2h)}(N_{Fe})$  varies proportionally with  $N_{Fe}$ .

The relative fractions (or spectral areas) that are associated with the effective numbers of neighbors  $N_{Fe}$ , are directly calculated by summing up the relevant probabilities  $P(p)$ , with weighting factors. The latter are deduced either from  $A^{(1)}(p)$  ( $p$  Fe atoms either in  $K^-$  or in  $K^+$ ) or from  $A^{(2)}(p)$  (either  $p_1$  Fe atoms in  $K^-$  and  $p_2$  in  $K^+$  or  $p_2$  Fe atoms in  $K^-$  and  $p_1$  in  $K^+$ ) given in Table S7:

$$\begin{cases} f(N_{Fe} = 0) = \left[ P(0) + \frac{3}{5} \times (P(2) + P(4)) + P(6) \right] / 3 \\ f(N_{Fe} = 1) = \left[ P(1) + \frac{9}{10} \times P(3) + P(5) \right] / 3 \\ f(N_{Fe} = 2) = 2 \times [P(2) + P(4)] / 15 \\ f(N_{Fe} = 3) = P(3) / 30 \end{cases} \quad (38)$$

## 2. Fitted values of Sn(2c) hyperfine magnetic fields

Only qualitative information can be obtained because the hyperfine magnetic fields of this site are small and the quadrupole splittings are large ( $\sim 2$  mm/s, Sec. IVB). The central quadrupole doublets associated with the Sn(2c) site are clearly observed on the Mössbauer spectra of  $TmMn_{6-x}Fe_xSn_6$  for  $x = 0.4$  and  $0.6$ . They display shoulders on both wings (Fig. 6 of the article). For  $x = 1.2$ , the whole central component appears as broadened.

We assume that  $p_1$  Fe atoms are in one of the two kagome planes and  $p_2 = p - p_1$  in the other. Below, we consider only the case of  $h=c$  with an AFII structure. As the anisotropic term,  $(-A_{aef,M}(2c)/6)$ , is rather small [9], as compared to the isotropic one, the predicted

hyperfine magnetic field simplifies to,  $B_{pred}^{(2h)}(N_{Fe}) = N_{Fe} \times |\Delta A_{is}(2c)|$  with  $0 \leq N_{Fe} = |p_1 - p_2| \leq 3$  and  $\Delta A_{is}(2h) = -(A_{isMn}(2h)\mu_{Mn} - A_{isFe}(2h)\mu_{Fe})$  ( $h=c$ ) (Eq. (10) of the article). The formal expressions of  $\Delta A_{is}(2d)$  and of  $|\Delta A_{is}(2c)|$  become similar. The inequality  $A_{isMn}^-(2h)\mu_{Mn} > A_{isFe}^-(2h)\mu_{Fe}$ , discussed for the Sn(2d) site in Sec. VIII.A.2 of

the article, is expected to hold for the Sn(2c) site too. The distances M-Sn(2d) and M-Sn(2c) at RT are much the same in Mn-rich stannides, respectively  $\approx 2.57, 2.61 \text{ \AA}$ .

Comparable values of  $\Delta A_{Is}(2d) = 3.4(1) \text{ T}$  and of  $|\Delta A_M(2c)|$  appear thus as a reasonable guess. In Table S8 of [1], we give only the hyperfine magnetic field values of  $B_{\text{exp}}^{(2c)}(1)$ . The  $B_{\text{exp}}^{(2c)}(1)$  are all similar for  $x=0.4, 0.6, 1.2$  and yield an estimate  $|\Delta A_M(2c)| = 3.4(4) \text{ T}$  (for  $N_{Fe}=0$ , the field is 0) which is in line with the above discussion. It might be just a fortuitous coincidence but the order of magnitude is likely correct.

## IX. MODELS OF HYPERFINE MAGNETIC FIELDS IN Fe-RICH $\text{TmMn}_{6-x}\text{Fe}_x\text{Sn}_6$ AND MODEL PARAMETERS

### A. Sn(2c) and Sn(2d) sites

Sn(2c) and Sn(2d) peaks form a broad central component and overlap. It is thus difficult to extract reliable values of hyperfine magnetic fields of Sn(2c) and Sn(2d) sites. In any case,  $B_{\text{exp}}^{(2c)}$  and  $B_{\text{exp}}^{(2d)}$  are only  $\sim 4\text{-}5 \text{ T}$ . The explicit expressions of the predicted hyperfine magnetic fields (h=c, d) are established in Eqs (32) to (34). Here, we simplify them to  $B_{\text{pred}}^{(2h)}(N_{Fe}) = N_{Fe} \times \|\Psi_{Mn,Fe}(2h)\boldsymbol{\mu} + \Phi_{Mn,Fe}(2h)\boldsymbol{\mu}_z\|$  with  $\boldsymbol{\mu} = \boldsymbol{\mu}_{Mn} = \boldsymbol{\mu}_{Fe}$ . This hyperfine magnetic field depends on the angle  $\theta$  between the transition metal magnetic moment and the [001] axis through its projection  $\boldsymbol{\mu}_z$ . Thus, only the hyperfine magnetic fields values of  $B_{\text{exp}}^{(2e)}(N_{Fe})$  at Sn(2e) sites, which are much larger than the previous ones  $B_{\text{exp}}^{(2e)} \sim 15\text{T}$ , are given in Table S9 of [1].

### B. Sn(2e) sites

The broad outer wings, due to Sn(2e) sites, tend to coalesce with the central peak on the one hand for the spectra of  $\text{TmMn}_{1.75}\text{Fe}_{4.25}\text{Sn}_6$  recorded at 51 and 300 K and on the other hand for the spectrum of  $\text{TmMn}_{1.5}\text{Fe}_{4.5}\text{Sn}_6$  recorded at 72 K (Fig. 8 of the article). These shape changes mean that an overall decrease of the Sn(2e) hyperfine magnetic fields takes place when T increases from 4.2K to 51K ( $x=4.25$ ) or to 72K ( $x=4.5$ ). Concomitantly, the angle  $\theta$  increases from  $\approx 7.5(6)^\circ$  respectively to  $\approx 69^\circ$  and  $\approx 53^\circ$  (Fig. 5 of the article). In contrast to the  $x=4.25$  spectrum at 300K, the outer wings of the  $x=4.5$  spectrum at 300K

emerge again from the central component (Fig. 8 of the article). Thus, an overall increase of the Sn(2e) hyperfine magnetic fields occurs without doubt when the temperature increases from 72K to 300K while the angle  $\theta$  decreases from  $\approx 53^\circ$  to  $\approx 11^\circ$  (Fig. 5 of the article and Table S5).

At low temperatures, the hyperfine magnetic field variations are thus triggered by those of  $\theta$  whose importance exceeds significantly that of the thermal decrease of magnetic moments. These experimental variations are then used to calculate the ratios  $\rho_{eff,Fe}^{(2e)}$ . Sn(2e) atoms, whose hyperfine magnetic fields are  $B_{exp}^{(2e)}(6)$ , are surrounded by six Fe nearest neighbors whose magnetic moments make angles  $\theta_1$  and  $\theta_2$  with the c-axis at two different temperatures, respectively  $T_1$  and  $T_2$ . As shown in Sec. VB, the ratio  $\rho_{eff,Fe}^{(2e)}$  is calculated from Eq. (21) where “ $B_{Fe,T}^{(2e)}(\theta)$ ” needed to calculate  $r_{12}$  (Eq. (18)) is now the hyperfine magnetic field  $B_{exp}^{(2e)}(6)$  measured at a temperature T at which Fe moments make an angle  $\theta$  with the c-axis.

The magnetic moments at 51K and 72K in Table S10 are interpolated from those measured by neutron diffraction. These moments were varied to determine the sensitivity of the calculated parameters to their values. The experimental values needed to obtain  $\rho_{eff,Fe}^{(2e)}$  from Eqs (18) and (21) from low-temperature values are given in Table S10 for  $x=4.25$  and  $x=4.5$ .

Equations (18) and (21) yield negative values of  $\rho_{eff,Fe}^{(2e)}$  whose average values are  $\rho_{eff,Fe}^{(2e)} = -0.80 \pm 0.06$  and  $-0.84 \pm 0.14$  for  $x=4.25$  and  $x=4.5$  respectively. We conclude unambiguously that  $A_{a,Fe}(2e)/A_{isFe}(2e)$  is negative as  $(1 - 3u_{zFe}^2(2e)) \simeq 0.8$ . These results contrast with the positive ratios  $A_{a,Mn}(2h)/A_{isMn}(2h)$  ( $h=c, d, e$ ) found for Mn-rich stannides [15] which imply that  $A_{a,Mn}(2h)$  is negative as is  $A_{isMn}(2h)$  [15]. The previous results suggest that the negative sign of  $A_{a,Fe}(2e)/A_{isFe}(2e)$  means that  $A_{isFe}(2e)$  is now positive as is then  $B_{exp}^{(2e)}(p)$  in accordance with band structure calculations which indicate opposite signs of isotropic hyperfine fields in Mn- and Fe-based  $RT_6X_6$  compounds ( $X = Ge, Sn$ ) [24-25].

**TABLE S10:**

Experimental values needed to obtain  $\rho_{eff,Fe}^{(2e)}$  in  $TmMn_{6-x}Fe_xSn_6$  ( $x=4.25, 4.5$ )

$x$	$T_1$ (K)	$\theta_1^\circ$	$\mu_{Fe}(T_1)$ ( $\mu_B$ )	$B_{Fe,T_1}^{(2e)}(\theta_1)$ (T)
4.25	4.2	7.6	2.35(3)	20.4
4.50	4.2	7.5	2.40(3)	21.2
	$T_2$ (K)	$\theta_2^\circ$	$\mu_{Fe}(T_2)$ ( $\mu_B$ )	$B_{Fe,T_2}^{(2e)}(\theta_2)$ (T)
4.25	51	70	2.30(5)	14.6
4.50	72	53	2.32(6)	16.6

From the hyperfine magnetic fields measured at  $T_1$  and at  $T_2$ , we write (Eqs (11) and (22)):

$$\left\{ \begin{array}{l} |A_{isFe}(2e)| = B_{Fe,T}^{(2e)}(\theta) / \left\{ \mu_{Fe}(T) \sqrt{\left(6 + \rho_{eff,Fe}^{(2e)}\right)^2 - 3\rho_{eff,Fe}^{(2e)}\left(12 - \rho_{eff,Fe}^{(2e)}\right)\cos^2(\theta)} \right\} \\ |A_{a,Fe}(2e)| = \left| \rho_{eff,Fe}^{(2e)} A_{isFe}(2e) \right| / \left(1 - 3u_{zFe}^2(2e)\right) \end{array} \right. \quad (39)$$

From Eqs (39), we obtain  $|A_{isFe}(2e)| = 1.15 \pm 0.02$  T/ $\mu_B$  and  $1.15 \pm 0.04$  T/ $\mu_B$  and  $|A_{aFe}(2e)| = 1.15 \pm 0.07$  T/ $\mu_B$  and  $1.21 \pm 0.15$  T/ $\mu_B$  for  $x=4.25$  and  $x=4.5$  respectively. The previous discussion leads to  $A_{isFe}(2e) = 1.15(3)$  T/ $\mu_B$  and  $A_{aFe}(2e) = -1.18(10)$  T/ $\mu_B$ . From the definition of  $A_M(2e) = A_{isM}(2e) - A_{aeff,M}(2e)/3$  (Eq. (12) of the article and below), we calculate then  $A_{Fe}(2e) = A_{isFe}(2e) \times \left(1 - \rho_{eff,Fe}^{(2e)}/3\right) = 1.48(10)$  T/ $\mu_B$ .

The latter value, calculated from moment rotation, agrees with the mean,  $A_{Fe}(2e) = B_{exp}^{(2e)}(6)/(6\mu_{Fe}) = 1.51(5)$  T/ $\mu_B$ , obtained from hyperfine magnetic fields measured at 4.2 K for  $4.25 \leq x \leq 6$ .

## X. $^{119}\text{Sn}$ MÖSSBAUER SPECTRA OF $\text{TmMn}_{6-x}\text{Fe}_x\text{Sn}_6$ stannides at 4.2 K

### A. Mn-rich ( $x=0.4, 0.6, 1.2$ ) at 4.2K

Figure S6 is plotted mainly for a visual comparison of shapes of  $^{119}\text{Sn}$  Mössbauer spectra.

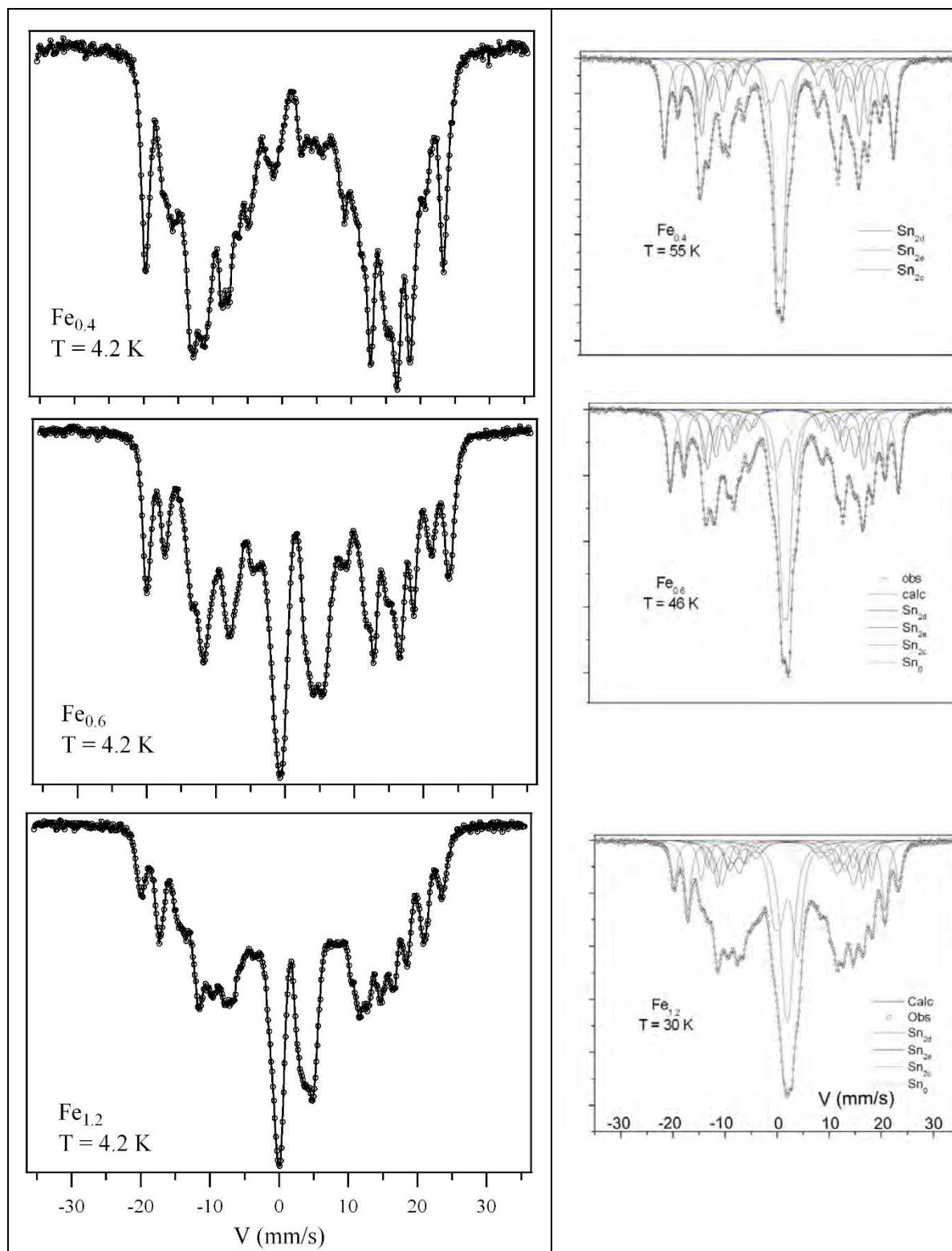


FIGURE S6:  $^{119}\text{Sn}$  Mössbauer spectra of Mn-rich  $\text{TmMn}_{6-x}\text{Fe}_x\text{Sn}_6$  ( $x=0.4, 0.6, 1.2$ ): left column at 4.2 K; right column at 55 K, 46 K, 30 K respectively. For each column, velocity scales are identical with the one given for the bottom spectrum.

It juxtaposes Mössbauer spectra at 4.2 K where spectra result from mixtures of several magnetic phases, importantly with ordered Tm magnetic moments, and spectra of Mn-rich  $\text{TmMn}_{6-x}\text{Fe}_x\text{Sn}_6$  ( $x=0.4, 0.6, 1.2$ ) recorded in the antiferromagnetic AFII state (Fig. 2 of the article) at 55 K, 46 K, 30 K respectively. These 4.2 K spectra, more particularly that recorded for  $x=0.4$ , exemplify the difficulty to unscramble with confidence the effects of complex low-temperature magnetic structures from those of the disordered substitution of Mn with Fe. The substitution effect is clearly evidenced at 55 K for  $x=0.4$  by comparison with the spectrum of  $\text{ZrMn}_6\text{Sn}_6$  in the AFII state at 100 K (Fig. 6 of the article).

### ***B. Fe-rich $\text{TmMn}_1\text{Fe}_5\text{Sn}_6$ and $\text{TmFe}_6\text{Sn}_6$ at 4.2 K***

Neutron diffraction results show that magnetic moments remain along the c-axis between 4.2 K and 300 K. Mössbauer spectra recorded at 4.2 K and at 300 K for  $x=5, 6$ , show no significant shape evolution (Figs S7 and S8) as M magnetic moments remain directed along the c-axis in the whole temperature range.

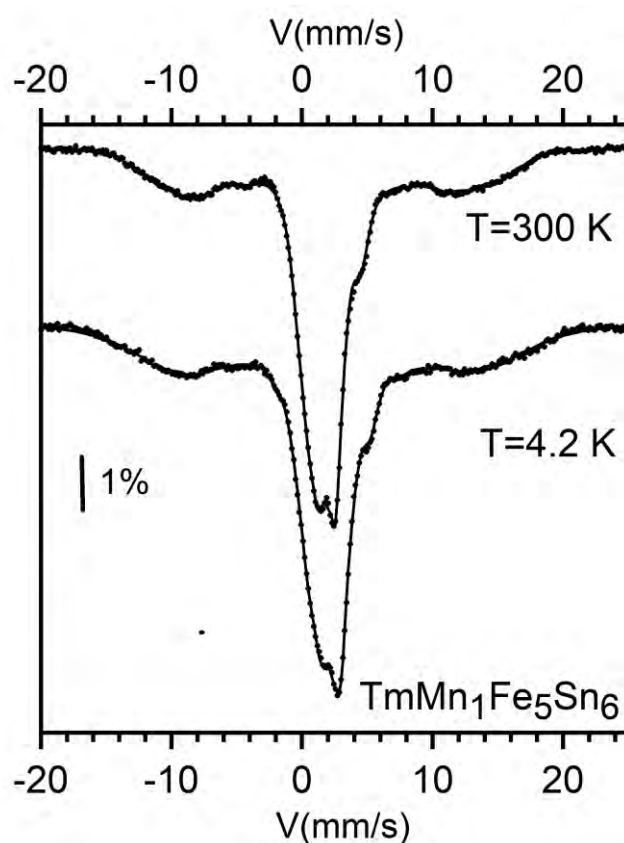


FIGURE S7: Observed (points) and calculated (solid lines)  $^{119}\text{Sn}$  Mössbauer spectra of  $\text{TmMn}_1\text{Fe}_5\text{Sn}_6$  with an AFI antiferromagnetic structure at 4.2 K and at 300 K.

A comparison of the Mössbauer spectra of figures S7 and S8 illustrates the effect of the substitution of 1Fe with 1Mn in  $\text{TmFe}_6\text{Sn}_6$ . Table S11 gives the results of least-squares fitting for Sn(2e) sites with six Fe first-nearest neighbors.

**TABLE S11:**

$^{119}\text{Sn}$  hyperfine parameters at Sn(2e) sites with six Fe first-nearest neighbors in  $\text{TmMn}_1\text{Fe}_5\text{Sn}_6$  and in  $\text{TmFe}_6\text{Sn}_6$  from least-squares fitted spectra recorded at 4.2 K.

Sn(2e)	Fe <sub>5</sub>	Fe <sub>6</sub>
Temperature	4.2 K	4.2 K
IS(mm/s)	1.96	2.03
$2\varepsilon$ (mm/s)	0.20	0.14
$\Gamma$ (mm/s)	2.49	1.69
$B_{\text{exp}}^{(2e)}(4)$ (T)	15.0	-
Area(4)	0.07	-
$B_{\text{exp}}^{(2e)}(5)$ (T)	18.4	-
Area(5)	0.14	-
$B_{\text{exp}}^{(2e)}(6)$ (T)	22.0	23.2
Area(6)	0.11	1

A stannide, with nominal composition  $\text{TmFe}_6\text{Sn}_6$ , was characterized by neutron diffraction experiments between 2 K and 300 K and by  $^{57}\text{Fe}$  Mössbauer spectroscopy at 4.2 K and 300 K by Mazet and Malaman [13]. However, asymmetries of  $^{57}\text{Fe}$  Mössbauer lines led to conclude that non-stoichiometry induces a local magnetic disorder. About 30% of iron atoms were estimated to have their moments which deviate from the c-axis and lie along intermediate directions between the basal plane and the c-axis. At first glance, the  $^{119}\text{Sn}$  Mössbauer spectra recorded at 4.2 K and at RT consist of two doublets and of one sextet (Fig. S8) as expected from an AFI magnetic structure.

Least-squares fitting with independent Lorentz lines yields for site Sn(2e), IS=2.03 mm/s,  $2\varepsilon=0.14$  mm/s, a FWHM of outer lines of 1.7 mm/s and a hyperfine magnetic field of 23.2(5) T calculated from outer lines of the sextet. The two paramagnetic doublets, due to Sn(2c) and Sn(2d) atoms sandwiched between antiferromagnetically coupled kagome planes, explain the slight asymmetry of the central component. Fig. S9 shows the 4.2 K hyperfine magnetic field distribution obtained from the latter sextet. The asymmetry of the hyperfine magnetic field distribution is attributed to the abovementioned deviations of a fraction of Fe moments from the c-axis [13]. The distribution of Fig. S9 is well fitted with two Gaussians. Their mean hyperfine magnetic fields, standard-deviations and weights, are respectively: 22.3 T, 1.2 T, 27% and 23.4 T, 0.3 T, 73%. The latter hyperfine magnetic field is associated with

Sn(2e) atoms whose six Fe neighbours have their moments along the c-axis. The weight of 27% is consistent with the one, 30%, mentioned above.

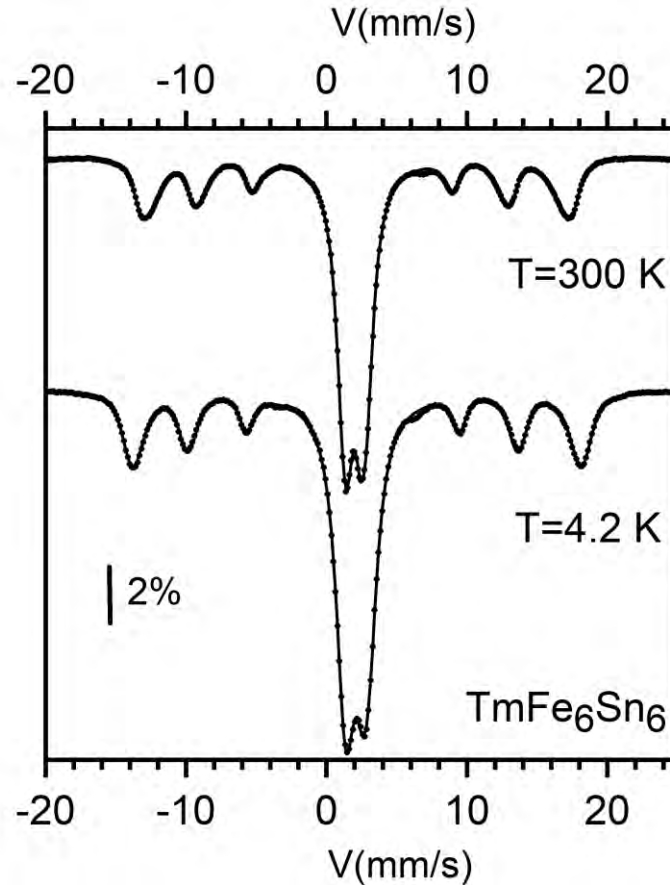


FIGURE. S8: Observed (points) and calculated (solid lines)  $^{119}\text{Sn}$  Mössbauer spectra of  $\text{TmFe}_6\text{Sn}_6$  with an easy-axis AFI antiferromagnetic structure at 4.2 K and at 300 K. The spectra were fitted with a constrained Hesse-Rübartsch method [17] which yields the hyperfine magnetic field distribution  $P(B)$  of Fig. S9.

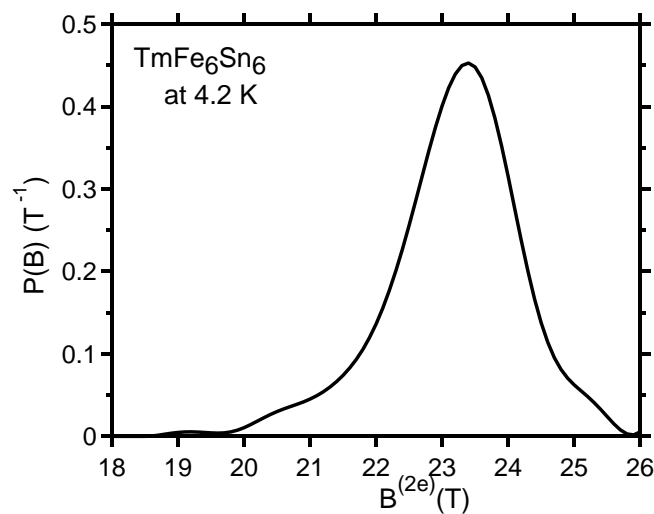


FIGURE S9: Hyperfine magnetic field distribution  $P(B)$  of Sn(2e) atoms (solid line) as calculated from the  $^{119}\text{Sn}$  Mössbauer spectrum of  $\text{TmFe}_6\text{Sn}_6$  at 4.2 K (Fig. S8).

## REFERENCES

- [1] N. J. Ghimire and I. I. Mazin, *Nature Materials* **19**, 137-138 (2020).
- [2] N. J. Ghimire et al., *Sci. Adv.*, **6**, 51 (2020) 10.1126/sciadv.abe2680.
- [3] R. L. Dally, J. W. Lynn, N. J. Ghimire , D. Michel , P. Siegfried and I. I. Mazin, *Phys. Rev. B* **103**, 094413 (2021).
- [4] Man Li et al., *Nat. Commun.*, **12**:3129 (2021).
- [5] Qi Wang et al., *Phys. Rev. B* **103**, 014416 (2021).
- [6] C.Q. Xu et al., *Phys. Rev. B* **104**, 024413 (2021).
- [7] Jia-Xin Yin et al., *Nature* **583**, 533 (2020).
- [8] Wenlong Ma et al., *Phys. Rev. Lett.* **126**, 246602 (2021).
- [9] Zhonghao Liu et al., *Phys. Rev. B* **104**, 115122 (2021).
- [10] Wenlong Ma et al., *Phys. Rev. B* **103**, 235109 (2021).
- [11] Dong Chen, Congcong Le, Chenguang Fu, Haicheng Lin, W. Schnelle, Yan Sun and C. Felser, *Phys. Rev. B* **103**, 144410 (2021).
- [12] T. Mazet, H. Ihou-Moko, J. F. Marêché and B. Malaman, *Eur. Phys. J. B* **51**, 173 (2006).
- [13] T. Mazet and B. Malaman, *J. Magn. Magn. Mater.* **219**, 33 (2000).
- [14] J. Bourgeois, G. Venturini and B. Malaman, *J. Alloys Compd.* **480**, 171 (2009).
- [15] L. K. Perry, D. H. Ryan and G. Venturini, *Phys. Rev. B* **75**, 144417 (2007).
- [16] J. Rodriguez-Carvajal, *Physica B* **192**, 55 (1993).
- [17] G. Le Caër and J. M. Dubois, *J. Phys. E: Sci. Instrum.* **12**, 1083 (1979).
- [18] G. Le Caër, B. Malaman, G. Venturini and I. B. Kim, *Phys. Rev. B* **26**, 5085(1982).
- [19] G. Venturini, B. Malaman, G. Le Caër and D. Fruchart, *Phys. Rev. B* **35**, 7038 (1987).
- [20] G. Le Caër, B. Malaman, G. Venturini, D. Fruchart and B. Roques, *J. Phys. F: Met. Phys.* **15**, 1813 (1985).
- [21] G. Le Caër, B. Malaman, G. Venturini, H. G. Wagner and U. Gonser, *Hyperfine Interact.* **28**, 631 (1986).
- [22] L.M. Corliss and J.M. Hastings, *J. Appl. Phys.* **39**, 461 (1968).
- [23] G. Venturini and B. Malaman, *J. Magn. Magn. Mater.* **377**, 159 (2015).
- [24] T. Mazet, J. Tobola, G. Venturini and B. Malaman., *Phys. Rev. B* **65**, 104406 (2002).
- [25] T. Mazet, J. Tobola and B. Malaman, *Eur. Phys. J. B* **33**, 183 (2003).
- [26] L. K. Perry, D. H. Ryan and G. Venturini, *Hyperfine Interact.* **170**, 105 (2006).
- [27] L. K. Perry, D. H. Ryan and G. Venturini, J. M. Cadogan, *J. Appl. Phys.* **99**, 08J302 (2006); **101**, 09K504 (2007).
- [28] G. Venturini, P. Lemoine and B. Malaman, *J. Magn. Magn. Mater.* **354**, 21 (2014).